

2

201600-11-F

Final Report

HIGH RESOLUTION IMAGING BY PHASE RETRIEVAL AND DISCRIMINATION USING SPECKLE

Volume 1

August 1987-January 1989

J.N. CEDERQUIST
J.R. FIENUP
J.C. MARRON
Advanced Concepts Division
March 1989

Approved for public release; distribution unlimited.

Sponsored by:
Office of Naval Research
800 N. Quincy
Arlington, VA 22217-5000

Prepared for:
Naval Research Laboratory
Washington, DC 20375-5000
Contract: N00014-86-C-0587

DTIC
ELECTE
NOV 06 1989
S E D

This document has been approved
for public release and sale in
distribution is unlimited.



ERIM

P.O. Box 8618
Ann Arbor, MI 48107-8618

Unclassified

SECURITY CLASSIFICATION OF THIS PAGE

REPORT DOCUMENTATION PAGE				Form Approved OMB No. 0704-0188	
1a REPORT SECURITY CLASSIFICATION Unclassified			1b RESTRICTIVE MARKINGS		
2a SECURITY CLASSIFICATION AUTHORITY			3 DISTRIBUTION AVAILABILITY OF REPORT Approved for public release; distribution unlimited.		
2b DECLASSIFICATION/DOWNGRADING SCHEDULE					
4 PERFORMING ORGANIZATION REPORT NUMBER(S) 201600-11-F			5 MONITORING ORGANIZATION REPORT NUMBER(S)		
6a NAME OF PERFORMING ORGANIZATION Environmental Research Institute of Michigan		6b OFFICE SYMBOL (if applicable)		7a NAME OF MONITORING ORGANIZATION Naval Research Laboratory	
6c ADDRESS (City, State, and ZIP Code) P.O. Box 8618 Ann Arbor, MI 48107-8618			7b ADDRESS (City, State, and ZIP Code) 4555 Overlook Ave., S.W. Washington, D.C. 20375-5000		
8a NAME OF FUNDING/SPONSORING ORGANIZATION Office of Naval Research		8b OFFICE SYMBOL (if applicable)		9 PROCUREMENT INSTRUMENT IDENTIFICATION NUMBER N00014-86-C-0587	
8c ADDRESS (City, State, and ZIP Code) 800 N. Quincy Arlington, VA 22217-5000			10 SOURCE OF FUNDING NUMBERS		
			PROGRAM ELEMENT NO.	PROJECT NO.	TASK NO.
			WORK UNIT ACCESSION NO.		
11 TITLE (Include Security Classification) High Resolution Imaging by Phase Retrieval and Discrimination Using Speckle					
12 PERSONAL AUTHOR(S) J.N. Cederquist, J.R. Fienup, and J.C. Marron					
13a TYPE OF REPORT Final, Vol. 1		13b TIME COVERED FROM 8/87 TO 1/89		14 DATE OF REPORT (Year, Month, Day) 1989 March	
15 PAGE COUNT xi + 121 = 132					
16 SUPPLEMENTARY NOTATION					
17 COSATI CODES			18 SUBJECT TERMS (Continue on reverse if necessary and identify by block number)		
FIELD	GROUP	SUB-GROUP			
20	05		Unconventional Imaging		
20	06		Phase Retrieval		
			Speckle		
19 ABSTRACT (Continue on reverse if necessary and identify by block number) Concepts for unconventional sensors capable of high-resolution imaging and parameter estimation for the SDI midcourse discrimination application were developed. The basic sensor consists of a large filled array of small-aperture receivers that measure a laser-illuminated object's Fourier intensity in the aperture of the receiver. Reconstruction of a high-resolution image using a phase retrieval algorithm was investigated via theoretical analysis, computer simulations, and laboratory experiments. In particular, modification of the basic sensor to include a small-aperture, diffraction-limited imager within the array was studied. A method was developed to use the additional low resolution image data in the process of reconstructing a high resolution image. This method first retrieves the Fourier phase over the small aperture of the low resolution imager using the Gerchberg-Saxton algorithm and then proceeds with phase retrieval over the entire array aperture using the iterative Fourier transform algorithm. This method was successfully demonstrated via computer simulations. Reconstruction of					
20 DISTRIBUTION AVAILABILITY OF ABSTRACT XX UNCLASSIFIED UNLIMITED □ SAME AS RPT □ DTIC USERS			21 ABSTRACT SECURITY CLASSIFICATION Unclassified		
22a NAME OF RESPONSIBLE INDIVIDUAL J.A. Blodgett			22b TELEPHONE (Include Area Code) 202-767-3674		22c OFFICE SYMBOL Code 6535

19. Abstract (Continued)

the image of a simple two-part object from Fourier intensity data gathered in a laboratory experiment was also achieved. Non-imaging, speckle correlation methods were developed which use the data provided by the large array of receivers to measure rotation rates and separation rates for multiple objects. Theoretical, computer simulation, and laboratory experimental results for both the rotation and separation measurement methods were obtained and found to be in good agreement with one another. The methods were shown to be robust at very low received light levels. The laser waveform and detector bandwidth requirements of the sensor system were also determined.

PREFACE

The work reported here was performed by the Optical Science Laboratory of the Advanced Concepts Division, Environmental Research Institute of Michigan (ERIM). The work was sponsored by the Office of Naval Research and the Naval Research Laboratory under Contract N00014-86-C-0587. At NRL, the technical monitor was Dr. Jerry A. Blodgett.

This final technical report covers work performed from 1 August 1987 to 31 January 1989. The principal investigator at ERIM was Jack Cederquist. Major contributors to this work were Jack Cederquist, James R. Fienup, Ann M. Kowalczyk, Joseph C. Marron, and Kirk S. Schroeder.

Accession For	
NTIS GRA&I	<input checked="" type="checkbox"/>
DTIC TAB	<input checked="" type="checkbox"/>
Unannounced	<input type="checkbox"/>
Justification	
By	
Distribution/	
Availability Codes	
Dist	Avail and/or Special
A-1	

TABLE OF CONTENTS

Preface.....	iii
List of Figures.....	vii
List of Tables.....	xi
1.0 Introduction.....	1
1.1 Background.....	1
1.2 Overview of Accomplishments.....	2
1.3 Summary Remarks and Recommendation.....	3
2.0 Measurement of Object Rotation Using Laser Speckle.....	5
2.1 Introduction.....	5
2.2 Analysis of Space-Time Correlation.....	8
2.3 Calculations of Normalized Correlation.....	14
2.4 Experimental Measurements of Speckle Correlation.....	21
2.5 Multiple Objects Rotating at Different Rates.....	31
2.6 Complicated Rotating Objects.....	35
2.7 Rotation Measurement at Low Light Level.....	35
2.8 Comparison to Conventional Doppler Radar.....	41
3.0 Measurement of Object Separation Using Laser Speckle.....	45
3.1 Introduction.....	45
3.2 Properties of the Fourier Transform of a Speckle Pattern.....	47
3.3 Measurement of Object Separation.....	51
4.0 Phase Retrieval for a Complex-Valued Object Using a Low-Resolution Image.....	59
4.1 Summary.....	59
4.2 Background.....	59
4.3 Optical Sensor Configuration.....	60

TABLE OF CONTENTS (Continued)

4.4	Data Processing Steps.....	63
4.4.1	Support Estimation.....	63
4.4.2	Small-Aperture Phase Retrieval Using Gerchberg-Saxton.....	70
4.4.3	Fine-Resolution Image Reconstruction.....	81
4.5	Image Reconstruction Example.....	85
4.6	Conclusion.....	89
5.0	Image Reconstruction Laboratory Experiments.....	93
5.1	Summary.....	93
5.2	Fresnel Zone Data Collection.....	93
5.3	Detector Calibration.....	95
5.4	Experimental Optical Set-up.....	96
5.5	Detector Sampling and Data Preprocessing.....	101
5.6	Experimental Results.....	103
6.0	System Analysis.....	107
6.1	Introduction.....	107
6.2	System Analysis for Parameter Estimation.....	107
6.2.1	Principles of Rotation Measurement.....	107
6.2.2	Source Requirements.....	109
6.2.3	Object Properties.....	111
6.2.4	Receiver Requirements.....	111
6.3	System Analysis for Image Reconstruction.....	112
6.3.1	Source and Sensor Requirements.....	112
6.3.2	Simulation Experiments.....	113
6.3.3	Computational Requirements.....	115
Appendix.	Error Variance Relationships.....	119

LIST OF FIGURES

2-1. Example of an Optical System Used to Observe Dynamic Speckle from Rough, Rotating Objects.....	6
2-2. Sampling Grid of Equally Spaced Ray Coordinates Used to Compute the Speckle Correlation Function.....	12
2-3. Optical System Used in the Simulation to Investigate Speckle from Rotating Disk Objects.....	15
2-4. Correlation Functions for Objects with Uniform, Lambertian, and Gaussian Scattering Profiles are Shown in (a), (b) and (c) Respectively.....	18
2-5. The Phase Function $\Delta\phi(x)$ that Appears in Eq. (2-5) is Plotted as a Function of Position on the Object for Various Amounts of Object Rotation.....	20
2-6. Optical System Used in the Experiments.....	22
2-7. Examples of the Speckle Correlation Functions Computed from Experimental Data.....	26
2-8. Scattering Profiles for Materials A, B and C of Table 1 are Shown in (a), (b) and (c) Respectively.....	29
2-9. Theoretical and Experimental Correlation Functions are Compared for Materials A, B and C in (a), (b) and (c) Respectively.....	30

LIST OF FIGURES (Continued)

2-10.	Correlation Functions for Speckle from Two Objects.....	34
2-11.	Examples of Speckle Patterns are Shown for the Indicated Light Levels.....	38
2-12.	Correlation Functions Generated for the Various Light Levels.....	39
2-13.	Cross-Sectional Plots Taken Horizontally Through the Center of the Correlation Functions Shown in Fig. 2-12.....	40
3-1.	Separation Measurement Using Laser Speckle.....	46
3-2.	Experimental Setup Used for Separation Measurements.....	53
3-3.	Examples of Various Sized Speckle Patterns are Shown in the Left Column.....	55
3-4.	A Comparison of Experimentally Measured Separation to the True Value for Various Speckle Pattern Sizes.....	56
4-1.	Optical Sensor Configuration.....	62
4-2.	Data Processing Steps to Reconstruct a Fine-Resolution Image (Retrieve the Phase in the Aperture Plane) from the Intensity Measurements.....	64

LIST OF FIGURES (Continued)

4-3. Thresholding the Low-Resolution Intensity Image to Estimate a Support Constraint, with no Weighting on the Small Aperture.....	66
4-4. Thresholding the Low-Resolution Intensity Image to Estimate a Support Constraint, with a Weighting on the Small Aperture.....	67
4-5. Removal of Nulls Due to Speckles in the Image.....	69
4-6. Block Diagram of the Gerchberg-Saxton Algorithms.....	71
4-7. Convergence of the Gerchberg-Saxton (GS) and Accelerated Gerchberg-Saxton (GS2) Algorithms.....	74
4-8. Convergence of the Combined GS2 and GS Algorithms for a Variety of Light Levels.....	75
4-9. RMS Error (ABSERR) of the Complex-Valued Reconstructed Low-Resolution Image as a Function of Iteration Number for a Variety of Light Levels.....	76
4-10. RMS Error of the Complex-Valued Reconstructed Low-Resolution Image as a Function of Light Level.....	77
4-11. Convergence of the Combined GS2 and GS Algorithms, using a Filtered Version of the Noisy Image, for a Variety of Light Levels.....	79

LIST OF FIGURES (Continued)

4-12.	RMS Error of the Complex-Valued Reconstructed Low-Resolution Image as a Function of Iteration Number, when using the Filtered Version of the Noisy Image, for a Variety of Light Levels.....	80
4-13.	Block Diagram of the Iterative Fourier Transform Algorithm..	82
4-14.	Image Reconstruction Example.....	86
4-15.	Intermediate Reconstruction Results with Different Weightings on the Fourier Modulus.....	87
4-16.	Convergence of the Iterative Fourier Transform Algorithm....	88
5-1.	Optical Setup for Phase Retrieval Laboratory Experiments....	97
5-2.	Image Reconstruction from Experimental Data.....	104
6-1.	Normalized RMS Error in Image Intensity for Image Reconstructed by Phase Retrieval and for Conventional Image Versus Number of Detected Photons/Speckle.....	114
6-2.	Normalized RMS Error in Image Reconstructed by Phase Retrieval Versus Normalized Error in Fourier Magnitude Data (Due to Additive Gaussian Noise in Fourier Intensity)..	116

LIST OF TABLES

Table 2.1	Materials Used to Coat Cylindrical Objects.....	23
-----------	---	----

1
INTRODUCTION

1.1 BACKGROUND

The ability to discriminate between targets (e.g., re-entry vehicles) and decoys is of great importance to our nation's strategic defense. One approach for accomplishing such discrimination is to obtain a fine-resolution image. Conventional approaches for fine-resolution optical (UV to near IR) imaging of objects at great distances require large-diameter receiver optics with near-diffraction-limited imaging performance. A very stable receiver support structure and/or adaptive correction of optical misalignment to within a fraction of a wavelength is also required to maintain this near-diffraction-limited performance. Further, if the receiver must operate over a large field-of-regard, prohibitively complex hardware is required. In our research program we have investigated a meaningful and realizable alternative solution to meet the challenge of fine-resolution imaging.

For coherently illuminated objects, a class of alternative, unconventional approaches to fine-resolution imaging uses a large array of small diameter receivers to make Fourier intensity measurements in the receiver aperture. From these measurements and additional low-resolution imagery and/or a priori information about the object, it is possible to compute a fine-resolution image using a phase retrieval algorithm. The intensity measurements can be made for objects over a large field-of-regard. In comparison to conventional approaches, this method greatly reduces the receiver hardware requirements in exchange for increasing the data processing necessary to compute the image. In addition, certain object parameters, such as rotation rate, can be determined from the Fourier intensity measurements without forming an image.

1.2 OVERVIEW OF ACCOMPLISHMENTS

This report describes the results of an 18 month program for development of unconventional approaches to image reconstruction and parameter estimation. In this section the principal results of the research program will be briefly summarized. They are reported in detail in the sections that follow. Sections 2 and 3 give research results in the area of parameter estimation and Sections 4 and 5 describe image reconstruction research. Section 6 reports on the investigation of system requirements.

The research conducted in the area of parameter estimation concerns two types of object parameters. The first, which is described in Section 2 is object rotation rate and the second, object separation, is the subject of Section 3. In the area of rotation measurement we have developed a simple model that allows us to compute the space-time correlation function of the speckle patterns from objects of arbitrary shape and surface material. This computational model was confirmed experimentally on cylinders with a variety of surface materials. We also demonstrated, both in theory and through experiments, rotation rate measurements of multiple objects illuminated simultaneously. Other topics covered include the robustness of rotation measurement at low light levels and a comparison of the speckle methods for rotation measurement with heterodyne methods. Measurement of object separation rate from the Fourier transform of speckle pattern data is described in Section 3. Both a theoretical treatment of separation measurement from speckle intensity and experimental results that demonstrate the method are given.

Ordinarily it is very difficult to reconstruct an image of a complex-valued object from the modulus of its Fourier transform (i.e., retrieve the Fourier phase) except for some special cases. In Section

4, a two-step approach is described for reconstructing high-resolution images of a general object from Fourier intensity data using additionally a low-resolution intensity image. First, the Fourier phase over the small aperture is retrieved using the Gerchberg-Saxton algorithm. Then that phase is used, in conjunction with the Fourier modulus data over a large aperture together with a support constraint on the object, to reconstruct a fine-resolution image (retrieve the phase over the large aperture) by the iterative Fourier transform algorithm. A series of simulations that demonstrate image reconstruction and test the sensitivity of the Gerchberg-Saxton algorithm to photon noise are described. Experiments were also conducted to demonstrate image reconstruction from Fourier intensity data obtained in laboratory experiments. The details of the experimental setup, system calibration, and successful reconstruction results for a simple two part object are given in Section 5. Finally, Section 6 of this report summarizes work done to specify the laser, detector, and data processor requirements of a deployed system for image reconstruction and parameter estimation.

1.3 SUMMARY REMARKS AND RECOMMENDATION

In summary, we have succeeded in developing important new image reconstruction techniques and speckle-based target parameter measurement techniques. These techniques have a strong potential for use in the SDI midcourse discrimination application. Further, it is important to note that these techniques do not require the use of large diffraction-limited optics or heterodyne detection and should therefore lead to more reliable, lower cost, and lighter weight system designs. We recommend additional research to further develop and apply these techniques.

2.1 INTRODUCTION

Consider the speckle pattern produced by a fully illuminated, 3-D object as shown in Fig. 2-1. It is assumed that the surface of the object is sufficiently rough to produce a fully developed speckle pattern in the observation plane. When the object rotates about a fixed axis, the dominant effect observed is that the speckle pattern translates perpendicular to the object's axis of rotation and that the distance of speckle translation is proportional to the amount of object rotation. Finer observation reveals that, along with the translation, the speckle pattern decorrelates or 'boils.' The degree of boiling is primarily dependent on the amount of object rotation and factors such as the locations of the source and observation plane as well as the underlying shape of the object.

In this section we analyze a simple computational model useful for calculating space-time correlation functions for speckle from rough rotation objects. These theoretically calculated correlation functions can be used to assess the ability to make remote measurements of an object's rotation rate and shape from speckle intensity correlation.

Speckle from rotating objects in free-propagation arrangements has been investigated by several authors. George [2.1] has provided a detailed analysis of the space-time correlation properties of speckle in the far field of the object. He considered point-source illumination of the entire object and calculated the space-time correlation function. An analysis of the Doppler spectrum obtained by interfering the scattered light with a local oscillator was also given.

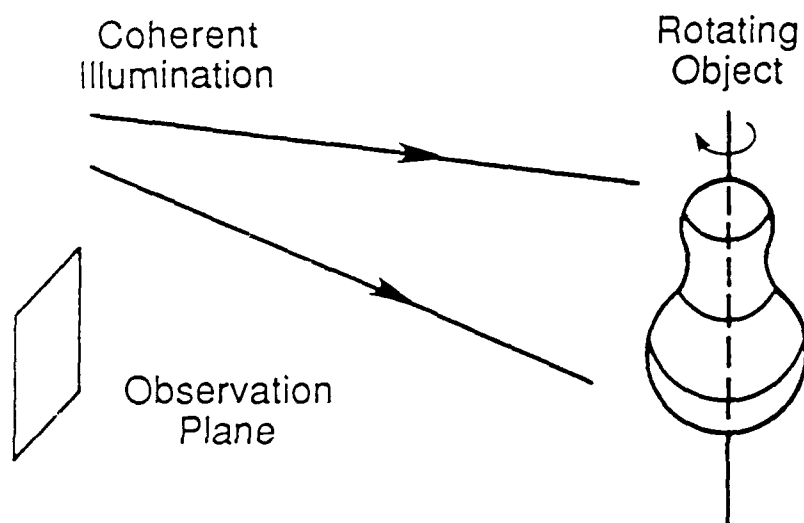


Figure 2-1. Example of an optical system used to observe dynamic speckle from rough, rotating objects.

Erdmann and Gellert [2.2] and later Takai et al. [2.3] analyzed speckle from rotating objects illuminated by a laser spot. Erdmann and Gellert developed an expression for the space-time intensity correlation function in the far field. Takai and co-workers considered a single detector in the near field and derived an expression for the temporal intensity correlation function. Both groups presented experimental measurements to verify the theoretical results.

Leader [2.4] has investigated temporal properties of the speckle by analyzing the frequency spectrum of the detected light. Smith [2.5] developed criteria to indicate when Doppler frequency shifts of the scattered light dominate the speckle effects.

Hayashi and Kitagawa [2.5] reported a technique to measure the rotation angle of a cylinder using near-field speckle. They derived a relationship in which the speckle translation is equal to the object rotation multiplied by a constant and confirmed their results with experiments.

From the investigations mentioned above it becomes apparent that calculations of the space-time correlation function of the optical field can be difficult, particularly when the object has a complicated underlying shape. In this section we present a relatively simple ray-trace method for computing space-time correlation functions of dynamic speckle. Here we consider only rotation about a fixed axis. However, the method can be applied to more complicated motions. The theoretical basis for the ray-trace method is presented in Section 2.2. In Section 2.3 the method is used to compute the space-time correlation function for a series of 2-D disk objects; these calculations allow one to develop an intuitive understanding of the amounts of speckle boiling and translation to expect for general objects. In Section 2.4 experimental calculations of the correlation function for speckle from a rotating cylinder are presented and compared to theory. In Section 2.5 we

consider multiple objects rotating at different rates and Section 2.6 contains comments on the application of this model to objects with complicated underlying shape. Section 2.7 contains analysis of the SNR for rotation measurement at low light level and in Section 2.8 the intensity detection methods presented in this paper are compared to heterodyne methods particularly at low light level.

2.2 ANALYSIS OF SPACE-TIME CORRELATION

A single polarization component of the optical field scattered by a rough object can always be written as a sum of contributions from discrete scattering cells on the surface. The optical field at an observation point p is thus

$$U(p) = \sum_k |A_k| \exp[i\phi_k] \quad (2-1)$$

where $|A_k|$ and ϕ_k are the amplitude and phase of the contribution from the k^{th} scattering cell respectively. The value of $|A_k|$ is determined by the scattering cross-section (or inclination factor) of the particular cell and the strength and uniformity of the illuminating field. The phase, ϕ_k , is given by the optical path length of the light as it travels from the source to the scattering cell to the detection point. In this treatment we ignore phase shifts caused by reflection from the surface and if the object depolarizes the incident light it is assumed that a polarization analyzer is placed in front of the detector.

To analyze the dynamics of the speckle pattern produced by target rotation we will use a quasi-static analysis of the optical field and thus concentrate on classical effects caused by position changes of the scattering cells. It is important to note that speckle dynamics predicted by this quasi-static analysis can equivalently be interpreted as self-doppler or autodyne effects [2.7,2.8].

From Eq. (2-1) we see that changes in the optical field caused by object rotation result from the following three effects;

- a) The particular scattering cells that enter the summation in Eq. (2-1) change as scatterers move into and out of the illuminated region of the object. The severity of this effect is dependent both on the extent of the illuminated region and shadowing caused by the underlying shape of the object. Shadowing caused by the surface roughness must also be considered at large bistatic angles.
- b) The amplitude of a scatterer $|A_k|$ can change because of angular dependence of the cross-section. Consider, for example, a faceted surface. The cross-section is very large when a facet normal directs incident rays from the source to the detection point and can drop off greatly as the facet normal rotates.
- c) The phases of the contributions change because of motion of the scattering cells caused by object rotation.

Our analysis, in both theory and experiment, has shown that, for most objects, speckle boiling and translation can be accounted for by the phase changes described in item c) alone. This conclusion is also supported by Leader [2.4]. The other effects can be significant if the underlying shape of the object is very complicated, the illuminated region of the object is small, or the cross section of the scattering cells has significant angular dependence. However, for the remainder of this analysis we concentrate on speckle dynamics that result from phase changes and proceed with the assumption that the other effects are negligible. The validity of this assumption is tested by the experiments presented in Section 2.4.

To quantify the dynamics of the speckle pattern the space-time correlation function of the optical field is used. Following the discussion above, our expression for the correlation function is dependent on object rotation only through the phase of the scattering cells. The space-time correlation function of the optical field is then

$$\langle U_1 U_2^* \rangle = \sum_k \sum_m \langle |A_k| |A_m| \exp[i(\phi_{k1} - \phi_{m2})] \rangle, \quad (2-2)$$

where the subscripts 1 and 2 denote space time coordinates (p_1, t_1) and (p_2, t_2) respectively. The phase term ϕ_{k1} represents the phase of the light from propagation from the source to the k^{th} scattering cell to the detection point p_1 at time t_1 before object rotation. The phase ϕ_{m2} is defined analogously.

To proceed with this calculation we follow Goodman [2.9] and place the following requirements on the field contributions:

- i) The amplitude and phase of the k^{th} scatterer are statistically independent of each other and of the amplitudes and phases of all other scatterers.
- ii) The phases are uniformly distributed over the fundamental interval $[-\pi, \pi]$.

With these requirements satisfied we adopt the delta correlation model,

$$\langle |A_k| |A_m| \exp[i(\phi_{k1} - \phi_{m2})] \rangle = \delta_{km} \langle |A_k|^2 \rangle \exp[i(\phi_{k1} - \phi_{k2})], \quad (2-3)$$

where δ_{km} is the Kronecker delta function. The space-time correlation function of the optical field then reduces to

$$\langle U_1 U_2^* \rangle = \sum_k \langle |A_k|^2 \rangle \exp[i\Delta\phi_k] \quad , \quad (2-4)$$

where we have substituted $\Delta\phi_k = \phi_{k1} - \phi_{k2}$.

To calculate the correlation function we will modify the sum in Eq. (2-4); instead of summing over the scattering cells indexed by k , we will sample the expected cross-section, $\langle |A_k|^2 \rangle$, and phase change, $\Delta\phi_k$, over a discrete grid of points and sum over these samples. This new sum is equivalent to tracing a series of rays that coarsely sample the object and adding up the corresponding magnitudes and phases; for this reason we refer to the technique as a ray-trace method. Using modified notation, the correlation function as calculated using the ray-trace method is

$$\langle U_1 U_2^* \rangle = \sum_k \langle |A(x_k)|^2 \rangle \exp[i\Delta\phi(x_k)] \quad (2-5)$$

where x_k denotes the ray coordinates. There are several subtle issues associated with choosing the proper ray coordinates for sampling a given object. For this investigation we have used a sampling grid with equally spaced ray coordinates; the corresponding grid for a 2-D object is shown in Fig. 2-2 (the extension to 3-D objects is straightforward and will not be discussed here). The line of the sampling grid passes through the axis of rotation of the object and is perpendicular to the vector connecting the axis of rotation and detection point p_1 . The sampling rays are traced from the source to points on the surface with x axis positions given by

$$x_k = x_0 + k \Delta x \quad (2-6)$$

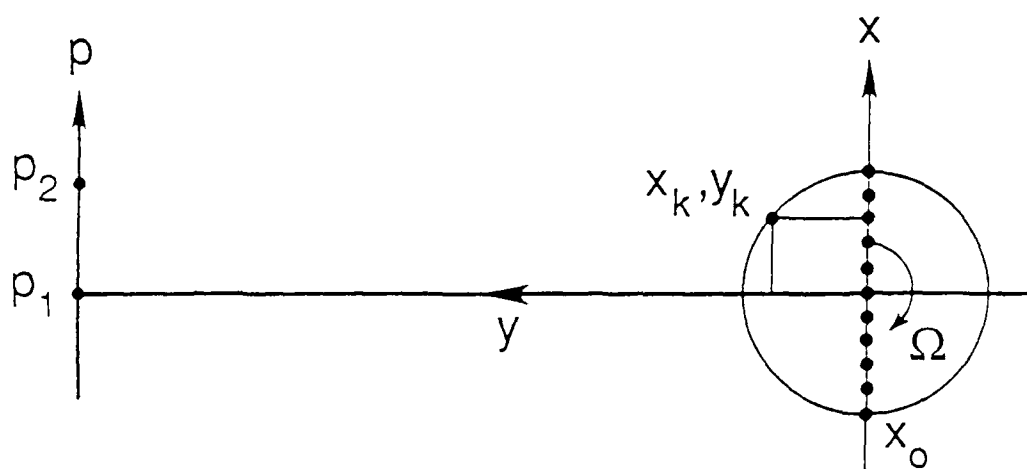


Figure 2-2. Sampling grid of equally spaced ray coordinates used to compute the speckle correlation function. The relationship of this grid to the object and detection points is shown.

where x_0 designates the beginning of the object as shown in Fig. 2-2 and Δx is the sample spacing. The axis of rotation is located at $x = 0$. A computer program used to calculate the correlation function would first determine the coordinate y_k on the surface that corresponds to the coordinate x_k as shown in Fig. 2-2. The program would then determine the cross-section, $\langle |A(x_k)|^2 \rangle$ of the object at (x_k, y_k) and compute the value of ϕ_{k1} , the phase corresponding to the optical path of a ray that travels from the source to (x_k, y_k) and to the detection point p_1 . Rotation of the object is then accounted for by rotating the coordinates of (x_k, y_k) as follows

$$x'_k = x_k \cos \Delta\theta + y_k \sin \Delta\theta \quad (2-7)$$

$$y'_k = -x_k \sin \Delta\theta + y_k \cos \Delta\theta \quad , \quad (2-8)$$

where the object rotates about the point $x = y = 0$ and $\Delta\theta$ is the amount of object rotation given by $\Delta\theta = \Omega(t_2 - t_1)$ with Ω being the angular rotation rate. More complicated object motions can be handled by modifying the transformation in Eqs. (2-7) and (2-8). The value of $\Delta\phi(x_k)$ is found by computing the difference $(\phi_{k1} - \phi_{k2})$ where ϕ_{k2} is the phase of the optical path between the source, the scatterer at (x'_k, y'_k) and the detection point p_2 .

With knowledge of $\langle |A(x_k)|^2 \rangle$ and $\Delta\phi(x_k)$ at many points on the object we can compute the correlation function of the optical field using Eq. (2-5). However, it is often more convenient to use the normalized form of the correlation function which is given by [2.9]

$$\mu_{12} = \frac{\langle u_1 u_2^* \rangle}{[\langle u_1 u_1^* \rangle \langle u_2 u_2^* \rangle]^{1/2}} \quad . \quad (2-9)$$

Values of μ_{12} fall in the range $0 \leq |\mu_{12}| \leq 1$ with $|\mu_{12}| = 1$ corresponding to pure speckle translation and $|\mu_{12}| < 1$ indicating boiling. After substituting Eq. (2-5), μ_{12} is given by

$$\mu_{12} = \frac{\sum_k \langle |A(x_k)|^2 \rangle \exp[i\Delta\phi(x_k)]}{\sum_k \langle |A(x_k)|^2 \rangle} \quad (2-10)$$

From Eq. (2-10) it is apparent that pure speckle translation results when $\Delta\phi(x_k)$ is a constant for all x_k and that the amount of speckle decorrelation is dependent on the deviation of $\Delta\phi(x_k)$ from being a constant. There is strong similarity between $\Delta\phi(x_k)$ and wavefront aberration of imaging systems. In fact $|\mu_{12}|^2$ is analogous to the normalized intensity from the diffraction theory of aberrations [2.10]. The normalized intensity is used to quantify the aberration content of an imaging system.

In summary, we have developed a model in which speckle dynamics can be accounted for by phase changes of the scattered light caused by object rotation. Speckle translation results when the phase changes imparted by object rotation are cancelled by the phase change caused by translation of the detection point. Speckle boiling results when the phase cancellation is not complete; the residual phase encountered with speckle boiling has the same effect on the correlation function as phase aberration has on the impulse response function of an imaging system.

2.3 CALCULATIONS OF NORMALIZED CORRELATION

In this section we apply the theory developed above to investigate speckle from rotating objects. For simplicity we consider the 2-D circular disk object shown in Fig. 2-3. Uniform plane wave illumination is used with the direction of propagation parallel to the vector

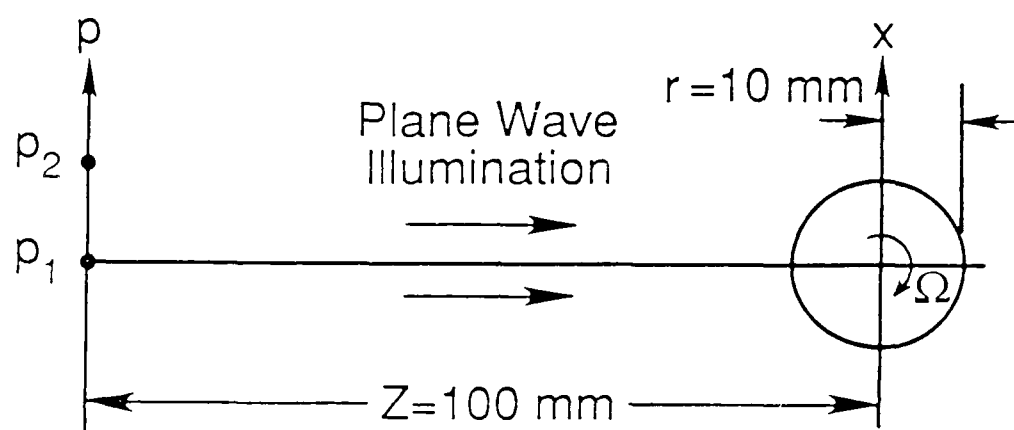


Figure 2-3. Optical system used in the simulation to investigate speckle from rotating disk objects.

connecting the object's axis of rotation with the detection point p_1 . The detection point p_1 is defined to be located at the $p = 0$ position on the p -axis. As the object rotates, the speckle pattern in the detection plane translates from p_1 toward p_2 . For the calculations presented here we took the object radius to be $r = 10$ mm and the range $z = 100$ mm.

The first step in computing the speckle correlation function is to characterize the scattering properties of the object by specifying the spatial dependence of the expected scattering cross-section $\langle |A(x)|^2 \rangle$. Here we consider three surface types; the first is an object for which the scattering cross-section is uniform for all x . This would result if the object is covered with perfect retroreflective paint; in this case

$$\langle |A(x)|^2 \rangle_U = 1, \quad (2-1i)$$

where the subscript U stands for uniform. Because the measured correlation is normalized, Eq. (2-11) can have any constant value; unity was chosen for simplicity.

The second type of surface to be considered is Lambertian for which the scattering cross-section varies as the cosine of the angle between the underlying surface normal and the direction of observation. For the coordinate system shown in Fig. 2-3 with $z \gg r$ we have approximately

$$\langle |A(x)|^2 \rangle_L \approx \left[1 - \left(\frac{x}{r} \right)^2 \right]^{1/2}, \quad (2-12)$$

where the subscript L stands for Lambertian and r is the object radius.

The final object type to be considered has a Gaussian cross-section function given by

$$\langle |A(x)|^2 \rangle_G = \exp \left[-\frac{x^2}{w^2} \right] , \quad (2-13)$$

where the subscript G stands for Gaussian. For the simulations reported here with a 10 mm radius object we used $w = 5$ mm which corresponds to an object that exhibits largely specular reflection.

The correlation functions computed using Eq. (2-10) for the disk objects are shown in Figs. 2-4(a-c). For each of the rotations considered the normalized correlation was computed for several locations of p_2 ; thus Fig. 2-4 shows $|\mu_{12}|^2$ as a function of detector separation for various amounts of object rotation, $\Delta\theta = \Omega(t_2 - t_1)$. The correlation for each point on the curves was found by tracing 100 rays equally spaced along the x-axis. The wavelength of the laser illumination was $\lambda = 0.5 \mu\text{m}$.

Figure 2-4(a) contains the correlation function for an object with uniform scattering cross-section given by Eq. (2-11). Each curve shows only the most significant sidelobes. The first curve, $\Delta\theta = 0.0$, designates the speckle size; the first zero is located at $2.375 \mu\text{m}$ while the formula $\lambda z/2r$ predicts $2.5 \mu\text{m}$. Notice that for increased rotation the speckle pattern translates and boils.

A rough estimate for the amount of speckle translation is well known to be $2z\Delta\theta$. For the middle curve in Fig. 2-4(a), $\Delta\theta = 0.2$ mrad and the expected translation is thus $40.0 \mu\text{m}$ while the observed value was $38.75 \mu\text{m}$. For $\Delta\theta = 0.4$ mrad the observed translation was $77.5 \mu\text{m}$ which is precisely twice the value for $\Delta\theta = 0.2$ mrad.

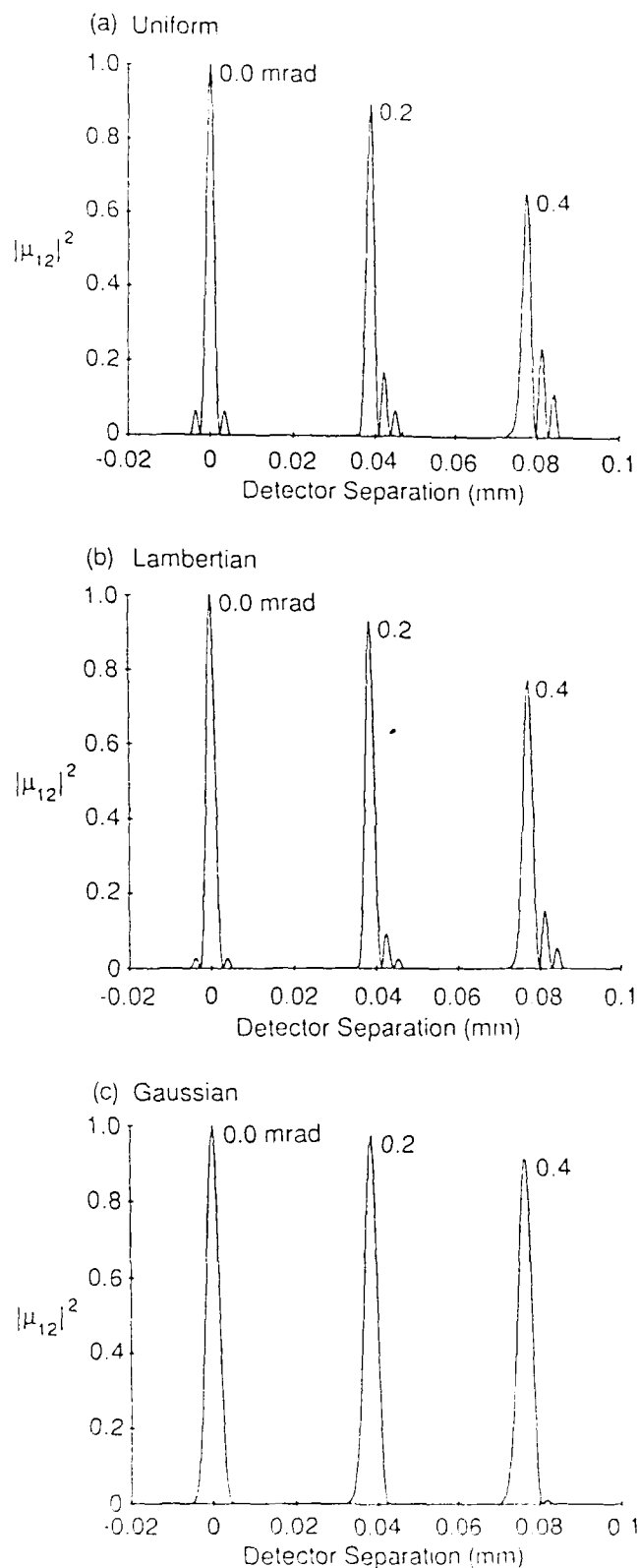


Figure 2-4. Correlation functions for objects with uniform, Lambertian, and Gaussian scattering profiles are shown in (a), (b) and (c) respectively. Each plot shows correlation as a function of detector separation for the various amounts of object rotation.

An interesting feature of Fig. 2-4(a) is the sidelobes. Notice that their magnitude increases steadily with rotation. From the severity of the sidelobes one can expect that the phase of the correlation function given in Eq. (2-10) is significantly aberrated. This aberration is further studied in the discussion of Fig. 2-5 below.

Figure 2-4(b) contains the correlation function calculated for the Lambertian object described in Eq. (2-12). The same trends are observed as for the uniform object, however now the speckle size is slightly larger and the boiling and sidelobes are less severe.

Figure 2-4(c) shows the correlation function for the object with Gaussian cross-section given in Eq. (2-13) with parameter $w = 5.0$ mm. Notice that the speckle size has increased over the previous two surfaces and that the amount of boiling and sidelobe magnitude is decreased.

To gain more insight into the behavior of the curves shown in Fig. 2-4, we have plotted the phase function $\Delta\phi(x)$ as a function of x in Fig. 2-5 for various amounts of rotation. For all cases the phase functions plotted are for the separations of p_1 and p_2 that correspond to the correlation peaks in Fig. 2-4(a). We have also subtracted $\Delta\phi(0)$ and thus plotted relative phase. Notice that the aberration increases with the amount of rotation. To understand how these curves affect the speckle dynamics consider Eq. (2-10). For the object with uniform cross-section the correlation value is given by the sum over the phases from the entire aberrated wavefront and thus with increased rotation the speckle boils markedly and sidelobes appear. For the Lambertian object the contribution from the highly aberrated edge region in Eq. (2-10) is reduced and thus the correlation is higher than for the uniform object. Finally for the Gaussian case only the central portion of the wavefronts in Fig. 2-5 contribute and thus essentially no boiling is exhibited.

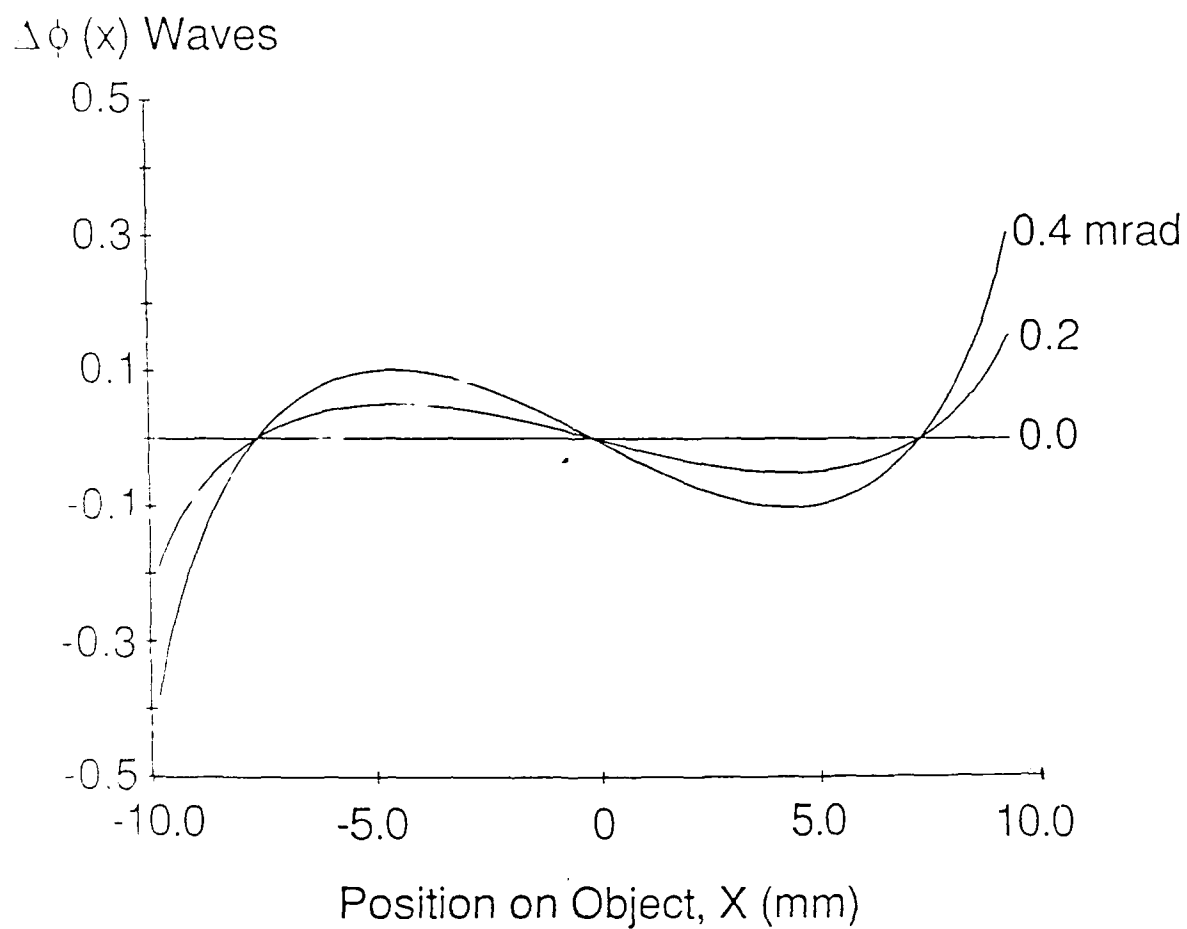


Figure 2-5. The phase function $\Delta\phi(x)$ that appears in Eq. (2-5) is plotted as a function of position on the object for various amounts of object rotation.

One important observation to make from this investigation is that the surface cross-section has the same effect on the correlation function as an apodizer does on the impulse response of an imaging system.

2.4 EXPERIMENTAL MEASUREMENTS OF SPECKLE CORRELATION

In this section results of experimental measurement of the normalized speckle correlation are given. The optical system used in the experiments is shown in Fig. 2-6. A uniform, collimated and polarized beam from an Ar^+ laser operating at $\lambda = 0.5145 \mu\text{m}$ is reflected by a beamsplitter and illuminates the target. The target was a 4.6mm diameter cylinder with height 4.6mm. Three different surface materials were used; they are summarized in Table 2.1. These materials were chosen to demonstrate that the theory applies to a broad range of materials. A linear polarizer was placed in front of the detector to insure that a single polarization was recorded even if the target depolarized the illumination.

The speckle patterns were recorded using a CCD camera with a pixel size of $18 \mu\text{m}$ in the direction of speckle translation and $21.3 \mu\text{m}$ in the other direction. The camera was oriented in a monostatic arrangement so that the central pixel was on the virtual axis of the illuminating beam. The distance from the target's axis of rotation to the video camera was 750 mm.

The output from the video camera was recorded with an eight bit digitizer. Correlation functions were computed from the recorded speckle patterns using an array processor. The relationship between the intensity measurements recorded by the detector array and the normalized correlation is given by [2.9]

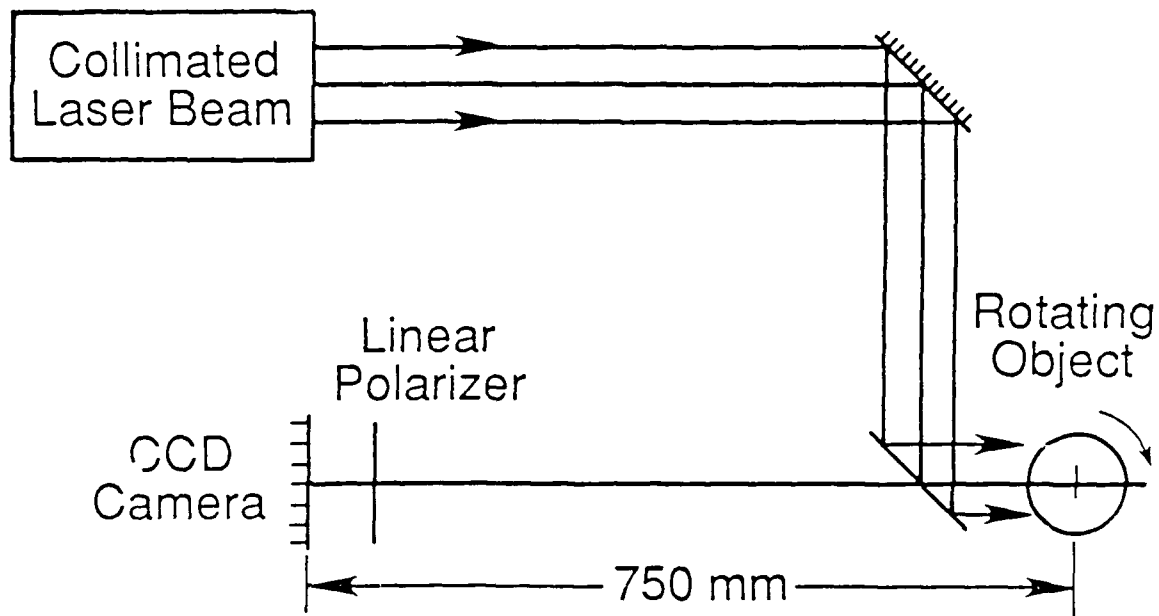


Figure 2-6. Optical system used in the experiments.

Material A	Retro-reflective paint composed of glass beads in a base material. 3M model 7216.
Material B	Typists correction fluid. Produces a uniform, flat-white surface.
Material C	Silver paint.

Table 2.1 Materials used to coat cylindrical objects.

$$|\mu_{12}|^2 = \frac{\langle I_1 I_2 \rangle}{\langle I_1 \rangle \langle I_2 \rangle} - 1 \quad , \quad (2-14)$$

where I_1 and I_2 denote the speckle patterns recorded before and after rotation. To compute the ensemble averages in Eq. (2-14) we used the statistically stationary nature of the speckle patterns so that instead of averaging over an ensemble of rough surfaces, the spatial average was computed. Simulations were conducted to determine that the speckle pattern was indeed statistically stationary over the area of the recorded speckle patterns. The speckle pattern was recorded over a 128 x 128 pixel array both before and after object rotation. Each of these data arrays was imbedded in a 256 x 256 array of zeros and the correlation in the numerator of Eq. (2-14) was computed using FFT techniques. We found that the computed values of $|\mu_{12}|^2$ were least noisy if the expected values $\langle I_1 \rangle$ and $\langle I_2 \rangle$ in Eq. (2-14) were computed only over the overlap region corresponding to each correlation offset. Thus the values of $\langle I_1 \rangle$ and $\langle I_2 \rangle$ are actually arrays. This technique for computing $|\mu_{12}|^2$ is superior to using constant values for $\langle I_1 \rangle$ and $\langle I_2 \rangle$ because it introduces positive correlation between the numerator and denominator of Eq. (2-14) which enhances the signal-to-noise ratio [2.11]. Each of the correlation functions was computed from a single pair of speckle data frames; there was no averaging over multiple frames.

Before computing the normalized correlation we had to correct the speckle data for pixel-to-pixel non-uniformities originating at the CCD camera. The two effects we considered were dark current and responsivity. To correct the responsivity we recorded a frame of data with the sensor exposed to uniform light from a distant broadband incoherent source and divided each frame of speckle data by this correction frame. We found that non-uniformities in the dark current were insignificant, however, the dark current was responsible for adding a uniform bias to the data. To correct this we modified the bias of the

speckle data so that the speckle contrast (the ratio of the standard deviation to the mean) was unity. Unity contrast is a property of fully-developed speckle, so by appropriately biasing the speckle data the correspondence to fully-developed speckle is increased.

Examples of experimentally measured correlation functions are shown in Figs. 2-7(a) and (b). For both figures the data was collected using the setup shown in Fig. 2-6 and the object was coated with material B. Figure 2-7(a) corresponds to zero object rotation and in Fig. 2-7(b) the object has rotated 2.0 arcmin. These photographs result from recording the 128 x 128 frames of speckle data before and after object rotation and computing the normalized correlation given by Eq. (2-14). The grey levels were set so that $|\mu_{12}| = 0.0$ is darkest and $|\mu_{12}| = 1.0$ is brightest and for intermediate values the grey level increases linearly. If the measured value of $|\mu_{12}|$ was below zero the grey level was set to the darkest value and if it was above unity the grey level was set to the brightest value.

The central pixel in Figs. 2-7(a) and (b) corresponds to zero correlation offset; thus for zero rotation (Fig. 2-7(a)) the correlation peak appears in the center. In Fig. 2-7(b) the object has rotated 2.0 arcmin and the corresponding translation of the speckle pattern gives the shifted correlation peak.

The extent of the correlation functions is limited by the 128 x 128 pixel size of the speckle data arrays. Notice that the statistical noise, which has a cloudlike appearance, increases radially from the center of each photograph. This is because the number of independent speckles used to compute the normalized correlation decreases with increased detector offset. As a result, one can expect false correlation peaks to occur in the corners of the correlation function where relatively few speckles enter the correlation measurements.

EXPERIMENTAL CORRELATION MEASUREMENTS

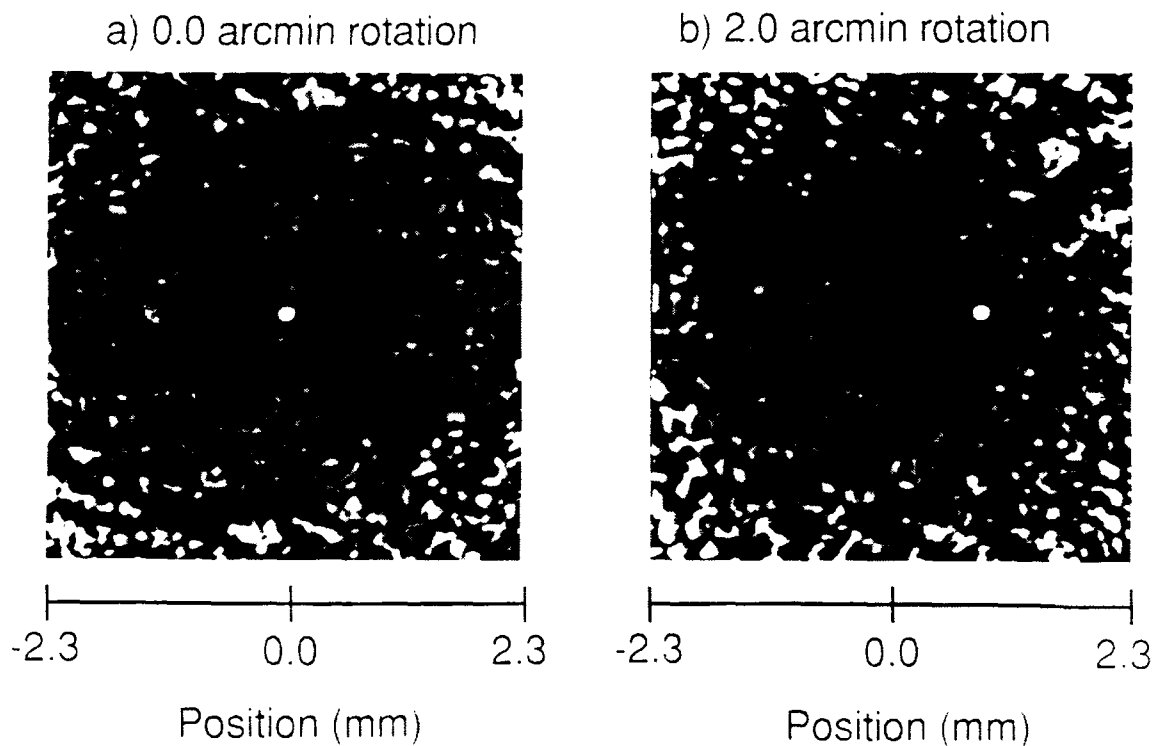


Figure 2-7. Examples of the speckle correlation functions computed from experimental data. (a) Object rotation is zero. (b) Object rotation is 2.0 arc min.

To theoretically predict the correlation functions for the various objects we used the ray trace procedure discussed in Section 2.3 of this paper. Because the height of the objects was small (4.6mm), we found that the correlation function calculated using many cross-sections of the object was identical, in the direction of speckle translation, to the correlation function computed using only the central cross-section of the object. In fact, we found that the height of the cylinder could be increased by several times before affecting the correlation function. All of the theoretical correlation functions given here are thus calculated from only the central cross-section of the object.

To compute the theoretical correlation function we had to experimentally measure the expected scattering profile, $\langle |A(x)|^2 \rangle$, for each target material. To accomplish this we imaged the target onto the CCD camera by placing a lens between the CCD camera and beamsplitter and illuminated the target with spatially incoherent light produced by passing the laser beam through a rotating diffuser. This procedure worked well for the objects covered with materials B and C, however, for material A more averaging was needed because of the strong point-like returns from the glass beads. To achieve more averaging, we rotated the target while collecting the profile data. The scattering profiles for target materials A, B and C are shown in Fig. 2-8(a), (b) and (c) respectively. Notice that the profiles are all different with material A being the most diffuse and material C the most specular. We found that the computed correlation functions are dependent on gross features of the profiles and insensitive to the noise in Figs. 2-8(a-c).

The theoretically calculated correlation functions along with the experimental measurements are shown for materials A, B and C in Figs. 2-9(a), (b) and (c) respectively. The correlation functions for the different materials are shown in separate illustrations with $|\mu_{12}|^2$ plotted vs. detector separation. The solid lines are theory and the circles are experimental measurements. The experimental results are

cuts in the direction of speckle translation through the correlation peak of the 2-D correlation function computed by the array processor as shown in Figs. 2-7(a) and (b). In each figure, the correlation functions are shown for increasing amounts of object rotation from 0 to 3 arcmin. Notice that for zero object rotation theory and experiment are in excellent agreement for materials A and B while the agreement for material C is not as close. For material C the experimental correlation function is considerably narrower than theory. We believe that this discrepancy results because the measured scattering profile shown in Fig. 2-8(c) is broader than the true profile should be. This indicates that the size of the simulated incoherent source (illuminated region of rotating diffuser) was too large. In future experiments, especially for objects with strong specular returns, the size of the incoherent source should be better controlled.

With increasing object rotation the speckle translates which causes the correlation peaks to shift. Theory and experiment remain in good agreement in Figs. 2-9(a-c) except for the largest rotation for which the agreement is less marked. For the larger rotations, the speckle has translated a considerable fraction of the width of data array which gives a lower signal-to-noise ratio that is evident in the disagreement between theory and experiment regarding the peak value of the correlation function. For the larger rotations also notice the slight disagreement between theory and experiment regarding the position of the correlation peak. At this point we do not know where the disagreement originates. It seems plausible that it originates in measuring the target distance and rotation or the detector pixel spacing, but we were extremely careful in measuring these parameters. One other possible source is the theory; the model used to theoretically compute the correlation functions is based on several simplifying approximations which may combine to cause the slight discrepancy.

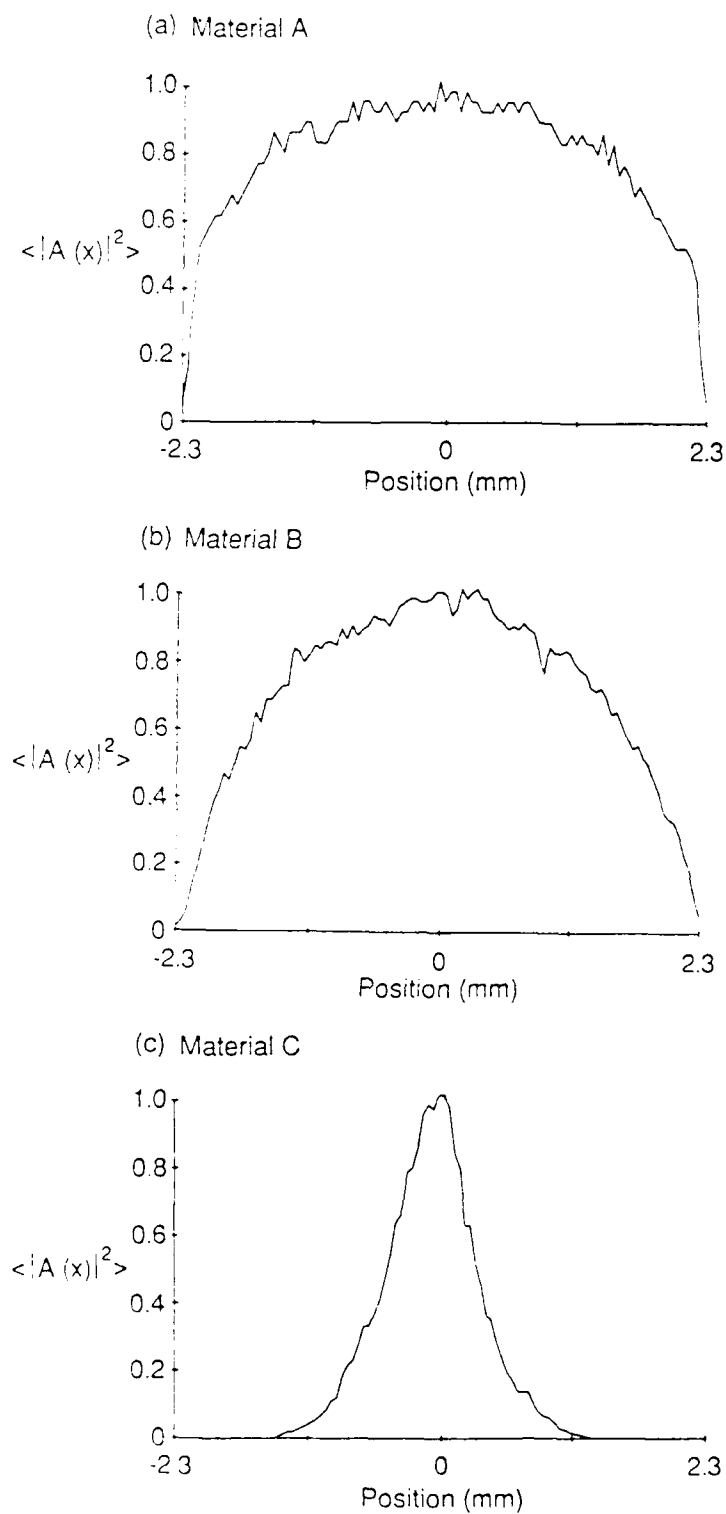


Figure 2-8. Scattering profiles for materials A, B and C of Table 1 are shown in (a), (b) and (c) respectively.

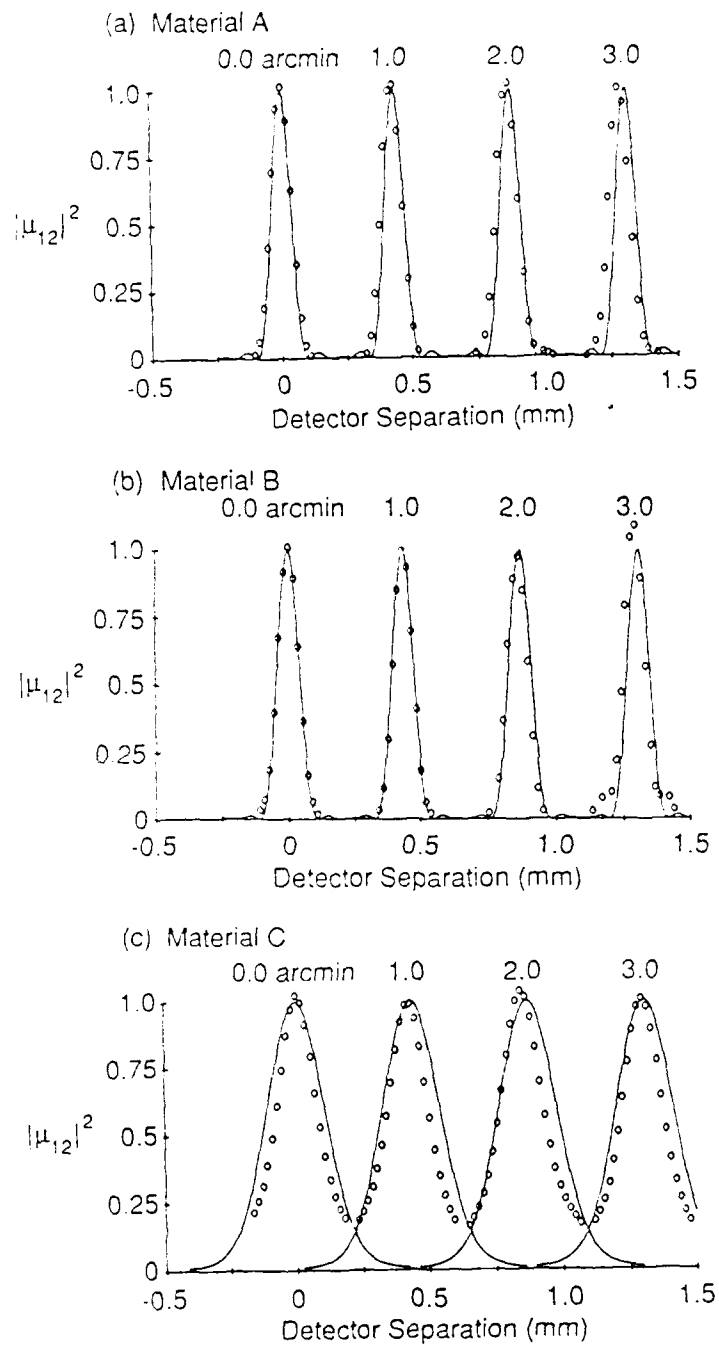


Figure 2-9. Theoretical and experimental correlation functions are compared for materials A, B and C in (a), (b) and (c) respectively. The correlation functions are plotted versus detector separation for the various amounts of object rotation. Solid lines are theory and circles are experimental measurements.

2.5 MULTIPLE OBJECTS ROTATING AT DIFFERENT RATES

Consider the dynamics of the speckle pattern produced when multiple rotating targets are illuminated simultaneously. Laboratory observation of such a speckle pattern reveals that each rotation rate imparts a component of translation to the speckle pattern, however, there is considerable boiling because the patterns from each target add coherently.

To further analyze the speckle dynamics consider the two target case. Eq. (2-10) gives

$$\mu_{12} = \frac{\sum_k \langle |A(x_k)|^2 \rangle \exp[i\Delta\phi(x_k)] + \sum_k \langle |A'(x_k)|^2 \rangle \exp[i\Delta\phi'(x_k)]}{\sum_k \langle |A(x_k)|^2 \rangle + \sum_k \langle |A'(x_k)|^2 \rangle} \quad (2-15)$$

where the primed and unprimed values of A and $\Delta\phi$ denote contributions from the two targets. In Section 2.2 it was noted that for a single object pure speckle translation results when $\Delta\phi(x_k)$ is constant for all x_k , and the amount of decorrelation is dependent on the deviation of $\Delta\phi(x_k)$ from being constant. Based on this observation we can make the following conclusions for the two target case:

- a) if $\Delta\phi(x_k)$ is constant for both targets the value of μ_{12} is unity. This situation would result, for example, if two identical targets were at the same distance with the same rotation rate. It could also result if the two targets were at different distances with proportionately different rotation rates.
- b) If $\Delta\phi(x_k)$ is constant for one object and deviates markedly for the other the correlation value would be

$$\mu_{12} = \frac{\sum_k \langle |A(x_k)|^2 \rangle}{\sum_k \langle |A(x_k)|^2 \rangle + \sum_k \langle |A'(x_k)|^2 \rangle} \quad (2-16)$$

For such targets we can conclude that a separate correlation peak will exist for each and the corresponding peak value is given by the fraction of the total return that is due to the particular object as dictated by Eq. (2-16). Thus for two targets of equal intensity the peak values are $\mu_{12} = 0.5$.

- c) If the values of $\Delta\phi(x_k)$ are neither constant nor vary substantially, Eq. (2-15) indicates that the contributions to μ_{12} from the two objects will add coherently.

The above conclusions also extend to more than two objects. With several objects we could thus expect a peak for each distinct rotation rate with the value at each peak given by the fraction of the total return from the specific target.

Experiments were performed to test the above conclusions. The experiments were identical to those of Section 2.4 except that two targets were used, one stationary and one rotating. The individual targets were identical to those used in the experiments reported in Section 2.4 with cylinder diameter and height equal to 4.6 mm. Both were coated with material B. The rotating object was placed on the optical axis of the system. The stationary object was placed above the other with the axes of symmetry coaligned. As in Section 2.4 we found that the theoretical predictions based on a single cross section from each object were equivalent to the predictions from multiple cross sections and therefore single cross-sections were used to form the theoretical predictions.

Theory and experiment are compared in Figs. 2-10(a-d). In each figure $|\mu_{12}|^2$ is plotted as a function of detector separation for rotation values of 0 arcmin to 1.5 arcmin in increments of 0.5 arcmin. The solid lines are theory and the connected circles are experimental measurements. For zero rotation, shown in Fig. 2-10(a), theory and experiment are in excellent agreement. For 0.5 arcmin of rotation in Fig. 2-10(b) there is excellent agreement regarding the position of the correlation peaks, however, there is substantial disagreement regarding the peak values. In the experiments we did adjust the illumination so that the peak values were equal, however, the peak values were both roughly $|\mu_{12}|^2 = 0.40$ in Fig. 2-10(b) while the theoretical prediction is slightly greater than 0.25 (for larger rotations the peak values approach a minimum of 0.25 as discussed above).

For larger rotations the trends continue; excellent agreement regarding peak location with experimental peak values significantly larger than theory. Also notice that a sidelobe not predicted by theory appears in Fig. 2-10(c). In Fig. 2-10(d) the correlation peaks are completely separated.

At this point we believe that the experimental values are consistently higher than theory because of distortions to the statistics of the speckle patterns imparted by the CCD camera and digitizer electronics. In the experiments the contrast of the speckle patterns was set to unity which increases the correspondence to fully developed speckle, however, we believe that the probability density functions of the data deviated from being negative exponential. In future research we will modify the instrumentation in hopes of improving the agreement between theory and experiment.

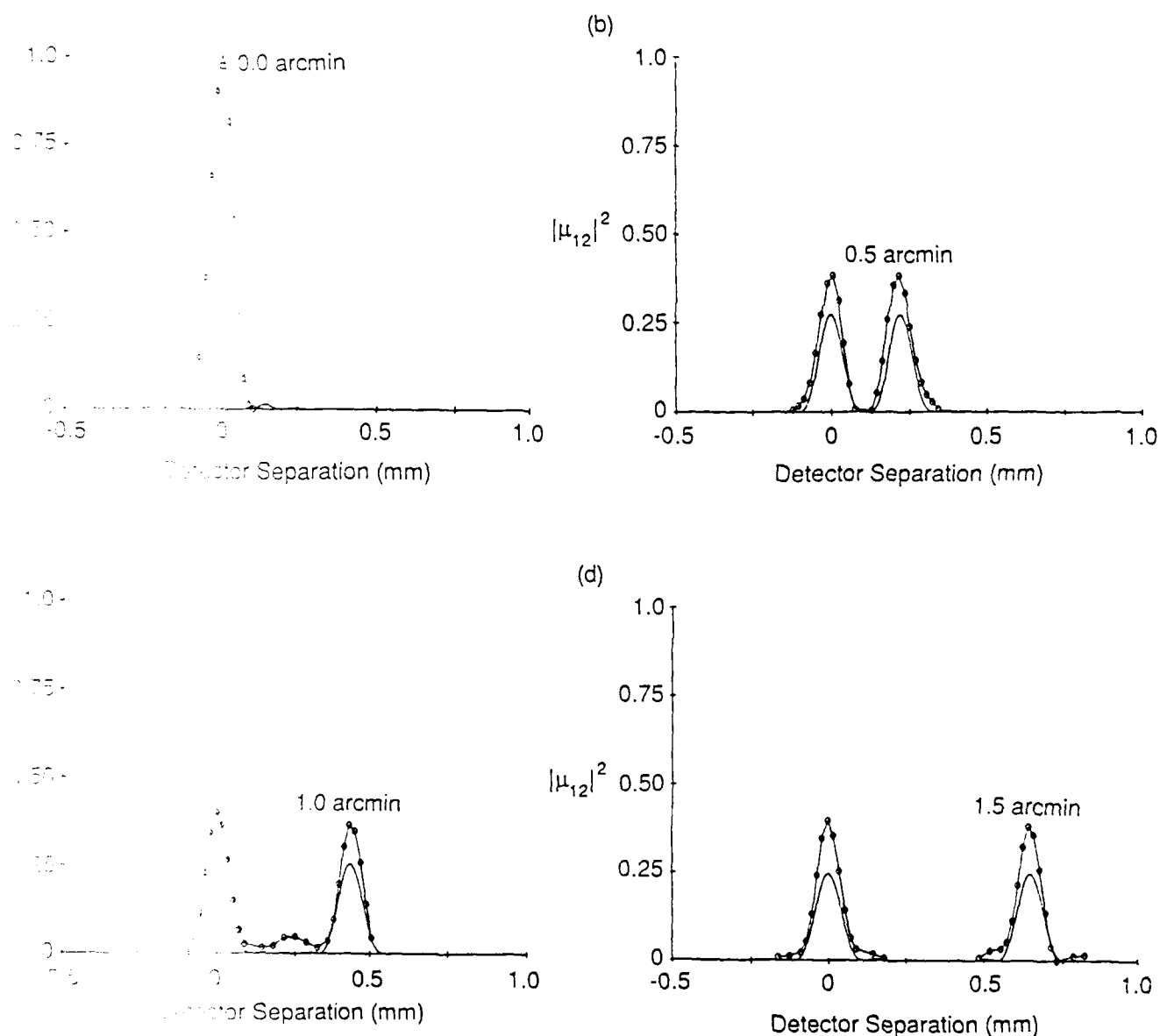


Figure 2-7 Correlation functions for speckle from two objects. One object is stationary and the other object rotates increasing amounts in (a), (b), (c) and (d) as shown. Solid lines are theory and connected circles are experimental measurements.

2.6 COMPLICATED ROTATING OBJECTS

Experiments were also conducted using objects with complicated underlying shape. The experimental setup shown in Fig. 2-6 was used and the object was a metallic scale model of a military jeep. The surfaces of the object were rough and the underlying shape had several concave features. The dimensions of the model in the directions transverse to the illumination were roughly 15 mm by 8 mm so the speckle size was considerably smaller than for the cylinders used in Section 2-4. The results of the experiments exhibited the same trends as for the cylindrical objects; the speckle translation is proportional to object rotation with negligible boiling. The only detectable difference was the speckle size which resulted in correlation peaks that were considerably narrower. From these results one can conclude that rotation measurements can be accomplished equally well for objects with simple or reasonably complicated underlying shapes.

2.7 ROTATION MEASUREMENT AT LOW LIGHT LEVEL

In this section we analyze the ability to perform rotation measurement at low-light level. The SNR for performing low-light level speckle correlation has been considered extensively in the literature. Analysis applicable to this application is contained in Ref. 2.12. Let us adapt the results of Ref. 2.12 to consider the case using a 2-D detector array to measure rotation. Let us assume that the speckle pattern does not move in the time between sequential recordings of the 2-D speckle pattern. As shown in previous sections, we are thus concerned with measuring a correlation function that has a peak value of $|\mu| = 1.0$ at the origin and gradually goes to zero value in a region equal to the speckle size of $\lambda R/D$. The SNR for such correlation measurements is [2.12]

$$\text{SNR} = \left[\frac{4MK}{20 + 12/N\langle n \rangle + 2/N\langle n \rangle^2} \right]^{1/2} \quad (2-17)$$

where M is the number of independent speckles encompassed by the detector array, K is the number of independent frame pairs used to measure the correlation, N is the number of detection channels per speckle and $\langle n \rangle$ is the mean number of photons per detection channel. With the number of photons per speckle large ($N\langle n \rangle \gg 1$), it follows that the first term in the denominator dominates. This first term is thus associated with statistical noise imparted by the speckle. As the number of photons per speckle decreases, the last two terms in the denominator of Eq. (2-17) dominate. To minimize noise at these low light levels, it follows by inspection of the last terms that with $N\langle n \rangle$ being constant, the number of detectors per speckle N , should be as small as possible.

We conducted some low-light level simulations to test the validity of the SNR formula in Eq. (2-17). In the laboratory we recorded a high-light level speckle pattern produced by back-illuminating a small diffuse square aperture with laser light. The pattern was recorded using a 2-D detector array. A region of size 128 x 128 pixels was used in the simulation. The detector pixel spacing and illuminating aperture size were such that there were 9 and 11 pixels per speckle in the vertical and horizontal directions respectively. These dimensions were extracted by correlating the high light level speckle pattern. In this simulation we thus had $M = 164$ and $N = 99$.

To simulate speckle recorded at low light level, a Poisson random number generator was applied to the recorded speckle pattern. For the Poisson generator we used, the expected number of photons per pixel, $\langle n \rangle$, is equal to the grey value per pixel averaged over the recorded pattern. Thus to achieve specific values of $\langle n \rangle$ the recorded pattern was multiplied by a scaling constant and then passed through the Poisson random number generator.

One goal of these simulations is to determine the lowest light level at which the rotation measurements can be made. In the limit of low light level, the expression for the SNR reduces to

$$\text{SNR} = \left[2MN \langle n \rangle^2 \right]^{1/2}, \quad (2-18)$$

where we have taken $K = 1$. By setting the SNR to unity and substituting $M = 164$ and $N = 99$, we find that the lower limit of acceptable light level is $\langle n \rangle = 5.54 \times 10^{-2}$ photons per pixel, or 0.55 photons per speckle. Note that if the experiment conducted with 1 pixel per speckle ($N = 1$), the lowest light level would be 0.055 photons per speckle. Thus the lowest acceptable light level is decreased by an order of magnitude by not oversampling this speckle. Oversampling should therefore be avoided in experimental design.

The results of this simulation are shown in Figs. 2-11, 2-12 a : 2-13. Figure 2-11 shows the original speckle pattern and the pattern at levels of 10^4 , 10^3 , 10^2 , 10, 5, 3 and 1 photons per speckle. Notice that the appearance of the speckle pattern gradually degrades as the light level decreases.

To simulate the correlation measurements at low light level we generated two independent realizations of the speckle noise for both from the same digitized speckle pattern. These were then correlated using the same Fourier transform procedure as in the experiments reported in Section 2.4. The simulation thus corresponds to situations in which the object has not rotated between the recordings of the speckle pattern.

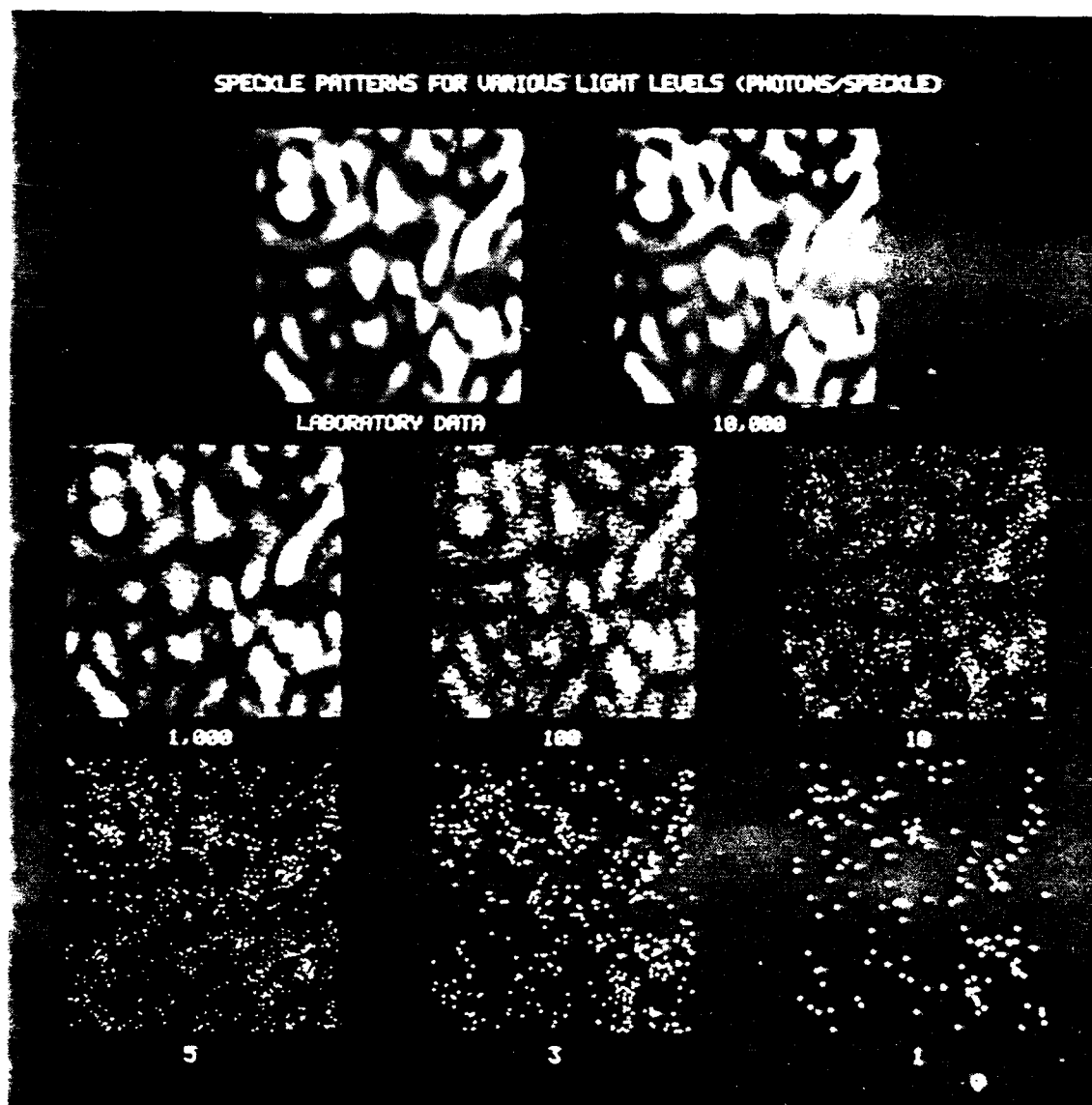


Figure 2-11. Examples of speckle patterns are shown for the indicated light levels.

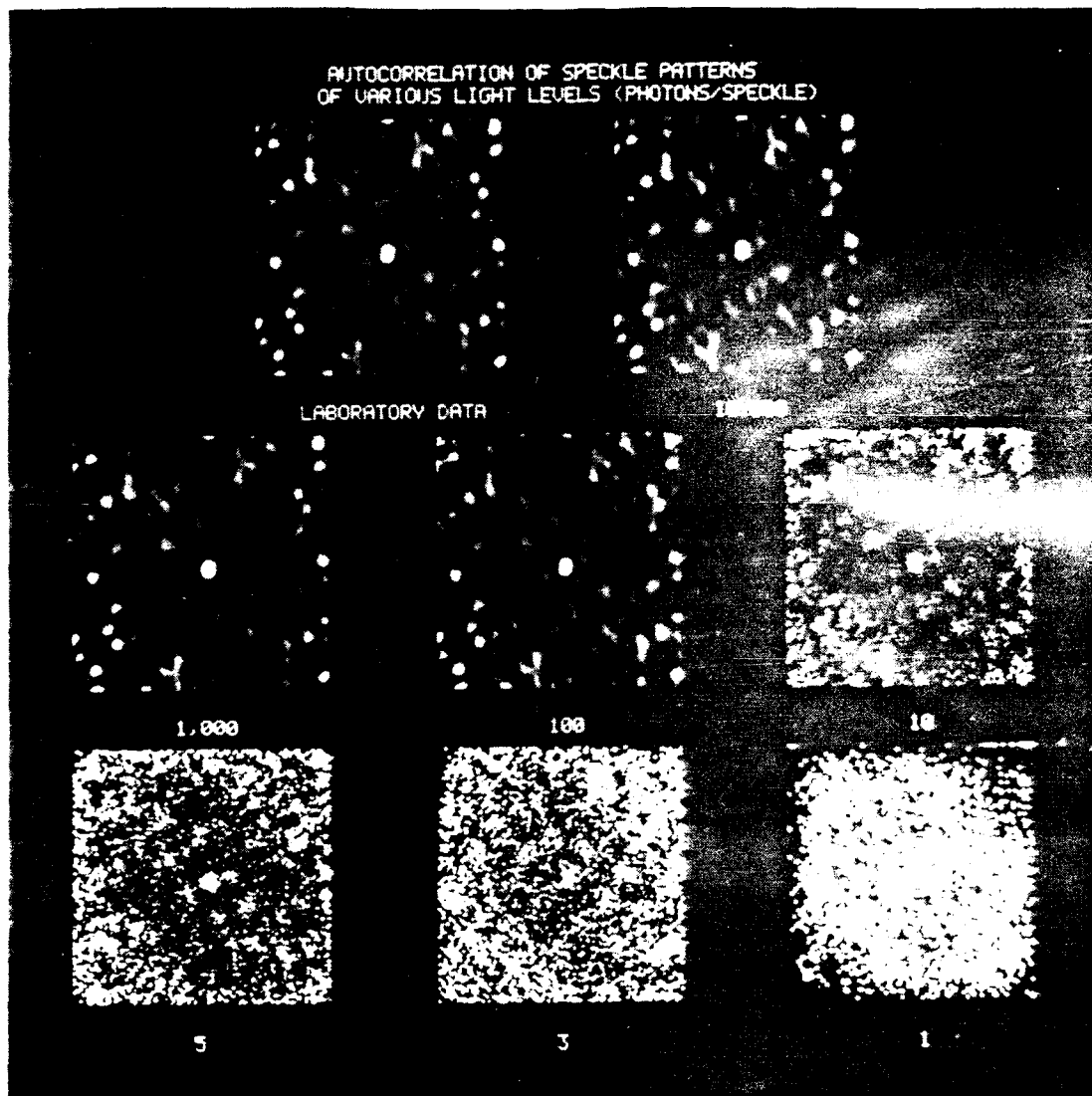


Figure 2-12. Correlation functions generated at the various light levels.

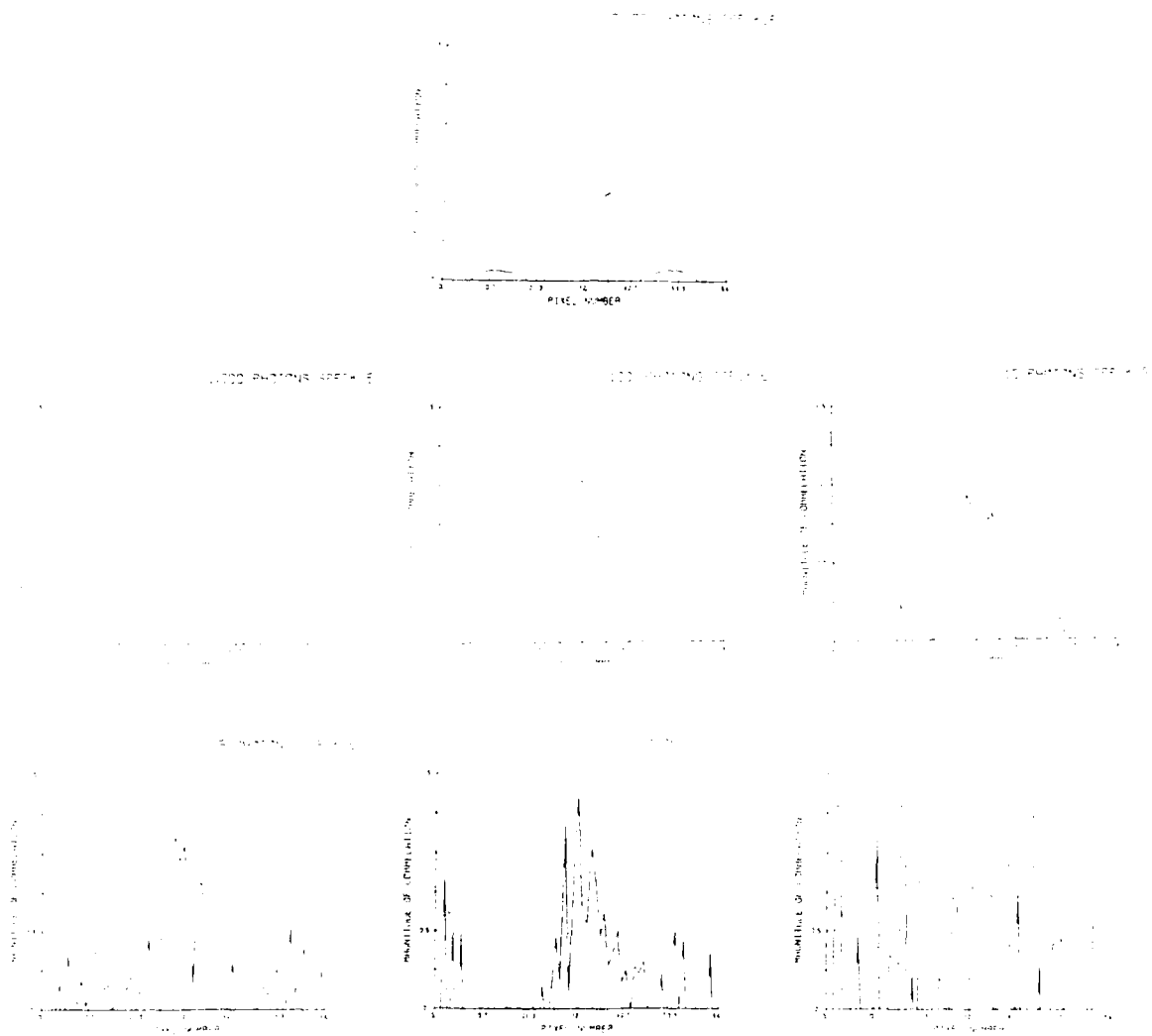


Figure 2-12. Correlation functions taken horizontally through the center of the image. The correlation functions shown in Fig. 2-12.

The correlation functions obtained for the various light levels are shown in Fig. 2-12. Along with the high light level correlation function the figure shows the correlation function at light levels of 10^4 , 10^3 , 10^2 , 10, 5, 3 and 1. Note that the correlation peak is recognizable at 3 photons per speckle and that it is not recognizable at 1 photon per speckle.

To better characterize the correlation performance, horizontal cross-sections through the correlation peak are shown for the various light levels in Figs. 2-13(a)-(g). Even at 100 photons per speckle in Fig. 2-13(c), the correlation function is barely degraded. The degradation increases, however, until it is not distinguishable in Fig. 2-13(g) at 1 photon per speckle.

For these simulations we have found that the lowest acceptable light level is roughly 1 photon per speckle. This result is in general agreement with the result of 0.5 photons per speckle predicted by Eq. (2-18). It must be stressed that this lower limit on the light level is for specific values of M and N and for other configurations the lower limit on the light level can vary substantially.

2.8 COMPARISON TO CONVENTIONAL DOPPLER RADAR

The basic difference between rotation rate measurement using speckle intensity and conventional Doppler radar is that the former uses autodyne detection while the later uses heterodyne detection. With autodyne detection the signal results from the interference of light scattered from different regions of the object and the phenomenon of Doppler beating corresponds to speckles passing over the detector. For heterodyne detection the signal corresponds to the interference of light from the entire object with a local oscillator and the Doppler signal is caused primarily by relative motion between the transmit/receive platform and the object. The heterodyne Doppler signal is also

modulated by the speckles passing over the detector. In fact, this speckle modulation, which gives rise to the Doppler spread, is the signal component that gives the rotation rate information.

In a comparison conducted in Ref. 2.8, it was found that autodyning and heterodyning are equally sensitive at measuring Doppler spread and thus rotation rate. It was also shown that autodyning is far less sensitive to the optical quality of the receiver and laser frequency stability. For SDI applications laser frequency stability over the long propagation distances is a fundamental problem for heterodyne systems.

One other issue is the SNR for autodyne detection vs. that for heterodyne detection. Let us assume that the return signal is shot noise limited; this assumption is applicable to the SDI scenario. Noise sources such as background noise and dark current are thus taken to be small compared to the signal level. It follows that in this limit the SNR's for the two detection schemes are equivalent; both are capable of single photon detection [2.13]. If the return signal is not shot noise limited, heterodyne detection does allow one to achieve the shot noise limit [2.13].

In summary, speckle intensity methods and heterodyne methods can, in theory perform equally well in measuring object rotation rate. In practice, however, the heterodyne methods require optical instrumentation of much higher quality and lasers with much greater frequency stability. These requirements are particularly imposing when a large array of heterodyne receivers is required. Using current technology, we do not feel that heterodyne detection is feasible for the SDI scenario, however, it does provide valuable information, particularly for image reconstruction, and does warrant technology development.

REFERENCES

- 2.1 N. George, "Speckle from rough, moving objects," J. Opt. Soc. Am. 66, 1182-1193 (1976).
- 2.2 J.C. Erdmann and R.I. Gellert, "Speckle field of curved, rotating surfaces of Gaussian roughness illuminated by a laser spot," J. Opt. Soc. Am. 66, 1194-1203 (1976).
- 2.3 N. Takai, T. Iwai, and T. Asakura, "An effect of curvature of rotating diffuse objects on the dynamics of speckles produced in the diffraction field," Appl. Phys. B 26, 185-192 (1981).
- 2.4 J.C. Leader, "An analysis of the frequency spectrum of laser light scattered from moving rough objects," J. Opt. Soc. Am. 67, 1091-1098 (1977).
- 2.5 J.L. Smith, "Far-field speckle and Doppler shifts for rough laser illuminated rotating cylinders," Appl. Opt. 18, 755-756 (1979).
- 2.6 A. Hayashi and Y. Kitagawa, "High-resolution rotation-angle measurement of a cylinder using speckle displacement detection," Appl. Opt. 22, 3520-3525 (1983).
- 2.7 E.R. Pike, Photon Correlation Spectroscopy and Velocimetry, B23, H.Z. Cummins and E.R. Pike, eds. (Plenum, New York, 1977), p. 6.
- 2.8 D.V. Fluckiger, R.J. Keyes and J.H. Shapiro, "Optical autodyne detection: theory and experiment," Appl. Opt. 26, 318-325 (1987).
- 2.9 J.W. Goodman, "Statistical properties of laser speckle patterns," in Laser Speckle and Related Phenomena, J.C. Dainty, ed. (Springer-Verlag, Berlin, 1975), Chapter 2.

- 2.10 M. Born and E. Wolf, Principles of Optics, 5th ed. (Pergamon, Oxford, 1975), Chapter 9.
- 2.11 J. Marron, "Accuracy of Fourier magnitude estimation from speckle intensity correlation," J. Opt. Soc. Am. A, 5, 864-870 (1988).
- 2.12 K.A. O'Donnell, "Time-varying speckle phenomena in astronomical imaging and in laser scattering," doctoral dissertation (University of Rochester, Rochester, NY, 1983).
- 2.13 A. Yariv, Introduction to Optical Electronics, (Holt, Rhinehart and Winston, New York, 1976), p. 308.

3
MEASUREMENT OF OBJECT SEPARATION USING LASER SPECKLE

3.1 INTRODUCTION

Consider a distant object consisting of two separate segments as shown in Fig. 3-1(a). The ability to resolve the segments using a conventional imaging system can be characterized by the Rayleigh criterion and the minimum resolvable angular separation is

$$\Delta\theta = 1.22 \lambda/D, \quad (3-1)$$

where λ is the wavelength and D is the diameter of the imaging lens. It follows that to measure the separation, rather than simply resolve it, requires a significantly larger aperture [3.1]. The achievable measurement accuracy is thus limited by the ability to construct large aperture, diffraction limited optics.

In this section of this report we analyze an alternative method for separation measurement that is based on laser speckle. This method requires active laser illumination of the separated object which is assumed to be diffusely reflective. Rather than using an imaging lens, the speckle pattern is detected using a 2-D detector array. While this technique does not relax the size requirement of the detection aperture, it does eliminate the need for large aperture, diffraction limited optics by instead using a 2-D detector array.

The basic idea behind this speckle technique is illustrated in Fig. 3-1. An example of a speckle pattern from the separated object shown in Fig. 3-1(a) is shown in (b). Notice the spatial modulation of the speckle pattern introduced by the object separation. The frequency of this modulation is proportional to the amount of separation. This spatial frequency information can be extracted using the Fourier transform. The squared magnitude of the Fourier transform of the

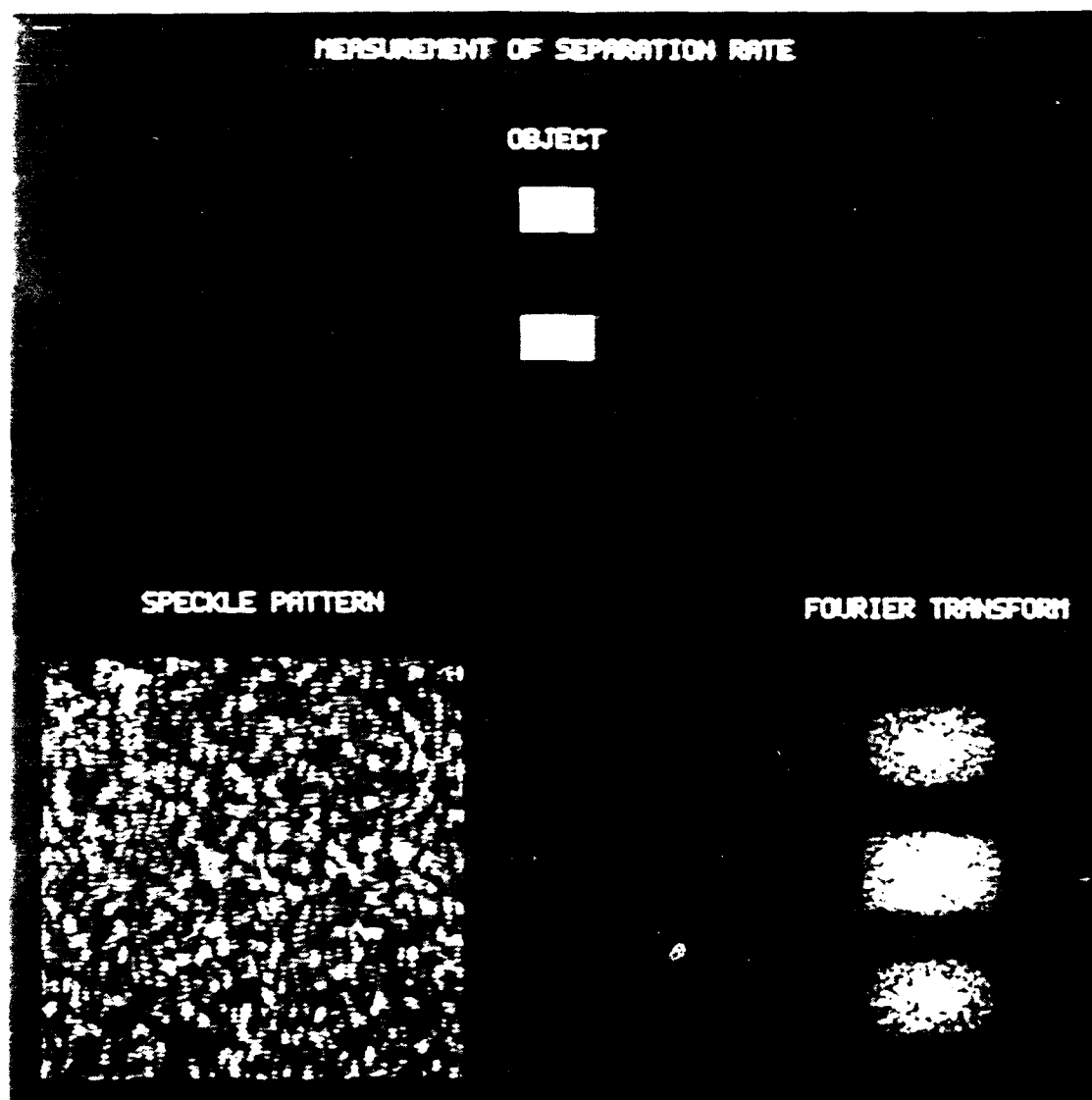


Figure 3-1. Separation measurement using laser speckle. (a) Separated object. (b) Realization of speckle pattern. (c) Fourier transform of speckle intensity.

speckle intensity is shown in Fig. 3-1(c); this transform essentially gives a speckled version of the object's autocorrelation. Measurement of the object separation is reduced to computing the distance between the center of this transform and the adjacent lobes. In Section 3.3 we discuss the use of centroid measurements to extract this information.

In summary, this investigation concerns a technique for measurement of target separation using laser speckle. While this technique does not reduce the aperture requirement below that of a conventional imaging system, it does not require a diffraction limited lens to cover the aperture, but instead a detector array. The requirement for precision optics is thus reduced.

In Section 3.2 of this report, statistical properties of the Fourier transform of a speckle pattern are investigated. The relationship between the transformed speckle pattern and the autocorrelation of the incoherent representation of the object is derived. A brief discussion of the sampling frequency required to record the speckle pattern without aliasing is also given.

In Section 3.3 the measurement of object separation by computing centroids of the transformed speckle pattern is examined. The measurement accuracy is quantified using laboratory data by comparing the actual and measured separations for several realizations of the speckle pattern with varying numbers of speckles over the detection aperture.

3.2 PROPERTIES OF THE FOURIER TRANSFORM OF A SPECKLE PATTERN

Let $I(x)$ be the intensity of a speckle pattern produced by illuminating a distant, rough object with coherent light. To simplify notation, this treatment is conducted in one dimension, however, the analysis is directly extendable to the 2-D case. It is assumed that $I(x)$ represents the intensity of a fully-developed speckle pattern in which case $I(x)$ is a negative exponential random variable.

The Fourier transform of an ideally recorded version of the speckle pattern is written as

$$\tilde{I}(u) = \int_{-b/2}^{b/2} I(x) \exp(-i2\pi ux) dx, \quad (3-2)$$

where b denotes the extent of the detection aperture. Inspection of Eq. (3-2) reveals that for each value of u , with the exception of u near zero, \tilde{I} is essentially a sum of randomly weighted phasors. Excluding u near zero, it follows from central limit theorem that when the detector array encompasses many independent speckles, \tilde{I} is a circular, complex Gaussian random variable. The Fourier transform of the speckle intensity thus obeys the same statistical model as the optical field in a speckle pattern.

The expected value of \tilde{I} is written as

$$\langle \tilde{I}(u) \rangle = \int_{-b/2}^{b/2} \langle I(x) \rangle \exp(-i2\pi ux) dx, \quad (3-3)$$

where the angular brackets denote an ensemble average. Because the object is taken to be at a large distance from the detection plane, it can readily be assumed that the speckle pattern is spatially stationary, in which case $\langle I(x) \rangle$ is independent of x . By defining $\langle I(x) \rangle = \langle I \rangle$ we have

$$\begin{aligned} \langle \tilde{I}(u) \rangle &= \langle I \rangle \int_{-b/2}^{b/2} \exp(-i2\pi ux) dx, \\ &= b \langle I \rangle \text{sinc}(bu), \end{aligned} \quad (3-4)$$

where $\text{sinc}(x) = (\sin \pi x)/\pi x$. In the limit of large b it follows that

$$\lim_{b \rightarrow \infty} \langle \tilde{I}(u) \rangle = \langle I \rangle \delta(u) \quad , \quad (3-5)$$

where δ is the Dirac delta function. Thus the transform of the intensity has zero expected value except near $u = 0$.

The expected value of the squared magnitude of \tilde{I} , or power spectrum, is written as

$$\langle |\tilde{I}(u)|^2 \rangle = \int_{-b/2}^{b/2} \int_{-b/2}^{b/2} \langle I(x_1) I(x_2) \rangle \exp[-i2\pi u(x_1 - x_2)] dx_1 dx_2 \quad (3-6)$$

The expected value that appears on the RHS of Eq. (3-6) can be factorized as follows [3.2]

$$\langle I(x_1) I(x_2) \rangle = \langle I \rangle^2 (|\mu(x_1 - x_2)|^2 + 1) \quad , \quad (3-7)$$

where μ is the complex normalized correlation of the speckle pattern which has a value in the range $0 \leq |\mu| \leq 1$. As noted in Ref. 3.2, μ is given by the normalized Fourier transform of the intensity distribution of the object. This relationship is analogous to the van Cittert-Zernike theorem from classical coherence theory [3.3]. In writing Eq. (3-7) we have used the stationary nature of the speckle pattern and thus only the difference of spatial coordinates appears.

To further evaluate Eq. (3-6) with Eq. (3-7) substituted, one must transform the integration to the difference coordinates, $r = x_1 - x_2$, which gives

$$\langle |\tilde{I}(u)|^2 \rangle = \langle I \rangle^2 \int_{-b}^b (b - |r|) (|\mu(r)|^2 + 1) \exp(-i2\pi ur) dr \quad (3-8)$$

Notice that Eq. (3-8) is the Fourier transform of a product. The important components of this product are first

$$\int_{-b}^b (b - |r|) \exp(-i2\pi ur) dr = b^2 \text{sinc}^2(bu) \quad (3-9)$$

which by assuming that b is much greater than the speckle size gives

$$\int_{-b}^b |\mu(r)|^2 \exp(-i2\pi ur) dr = \int_{-\infty}^{\infty} f(\xi) f(\xi - u) d\xi \quad (3-10)$$

$$= f(u) * f(u) \quad (3-11)$$

where f is the Fourier transform of μ and $*$ denotes autocorrelation. As mentioned above it follows from the van Cittert-Zernike theorem that f is the intensity distribution of the object. Using Eqs. (3-9), (3-10) and (3-11), Eq. (3-8) is re-written as

$$\langle |\tilde{I}(u)|^2 \rangle = b^2 \langle I \rangle^2 \text{sinc}^2(bu) * [f(u) * f(u)] + b^2 \langle I \rangle^2 \text{sinc}^2(bu) \quad (3-12)$$

The most important term in Eq. (3-12) is the autocorrelation of the object's intensity distribution, $f * f$. As shown in Fig. 3-1, this autocorrelation gives the distinct lobes from which the separation is measured.

Added to the autocorrelation is a sinc function which for large b reduces to a delta function at the origin. The result of the addition is then convolved with a sinc^2 that also amounts to a delta function for large b .

One other important feature of the Fourier transform of the speckle pattern is the size of the speckle in the transform domain. If the original speckle data is contained in an array of length M , which is then imbedded in a larger array of zeros of length N , the speckle size in the transform domain is N/M .

One final consideration is how finely the speckle pattern must be sampled to avoid aliasing in the transform of the speckle intensity. Let us define d to be the size of the 1-D object; that is, the object intensity is zero outside of a region of size d . It follows that the maximum detector pixel spacing before aliasing occurs in the transform is

$$s = \lambda Z / 2d \quad (3-13)$$

where Z is distance between the object and detector array.

3.3 MEASUREMENT OF OBJECT SEPARATION

In the last section it was shown that the Fourier transform of the intensity of a speckle pattern is essentially a speckled version of the autocorrelation of the object's intensity distribution. In this section we consider the extraction of object separation from the autocorrelation.

One way to measure object separating from the autocorrelation would be to measure the distance from the peak of one of the sidelobes to the center (see Fig. 3-1(c)). Because of the speckle, however, this procedure is likely to be inaccurate especially for objects with smoothly peaked autocorrelation sidelobes.

Another method for separation measurement is to compute the centroid of the sidelobe which is defined by

$$\bar{x} = \frac{1}{M} \sum_m m |\tilde{I}_m|^2, \quad (3-14)$$

where M is the sidelobe mass

$$M = \sum_m |\tilde{I}_m|^2. \quad (3-15)$$

The sums in Eqs. (3-14) and (3-15) extend only over the area of the sidelobe. Because the center of the autocorrelation is at $m = 0$, the centroid gives the object separation directly. Two dimensional separations are computed by defining the sums in Eqs. (3-14) and (3-15) to extend over the 2-D sidelobe and \bar{y} is computed analogously to \bar{x} .

For objects with diameter larger than their separation the sidelobes are not separated. In this case one can use a thresholding procedure whereby the threshold is raised until the sidelobes are distinct and then the centroid is computed.

Analytic computation of the accuracy for separation measurement using centroiding is very complicated. For this reason we have determined the accuracy empirically. Particularly we have investigated the number of speckles encompassed by the detector array required to accurately measure the separation. This aperture requirement can then be compared to the Rayleigh criterion given in Eq. (3-1) and the analysis of Ref. 31.

Experimental separation measurements were conducted using the setup shown in Fig. 3-2. The diffuse object consisted of two vertically separated circles both of diameter 3.05 mm with center-to-center spacing equal to twice the diameter. This object was illuminated with coherent illumination at $\lambda = 0.5145 \mu\text{m}$ and the speckle pattern was recorded at a distance of 154 cm using a CCD detector array. The center-to-center

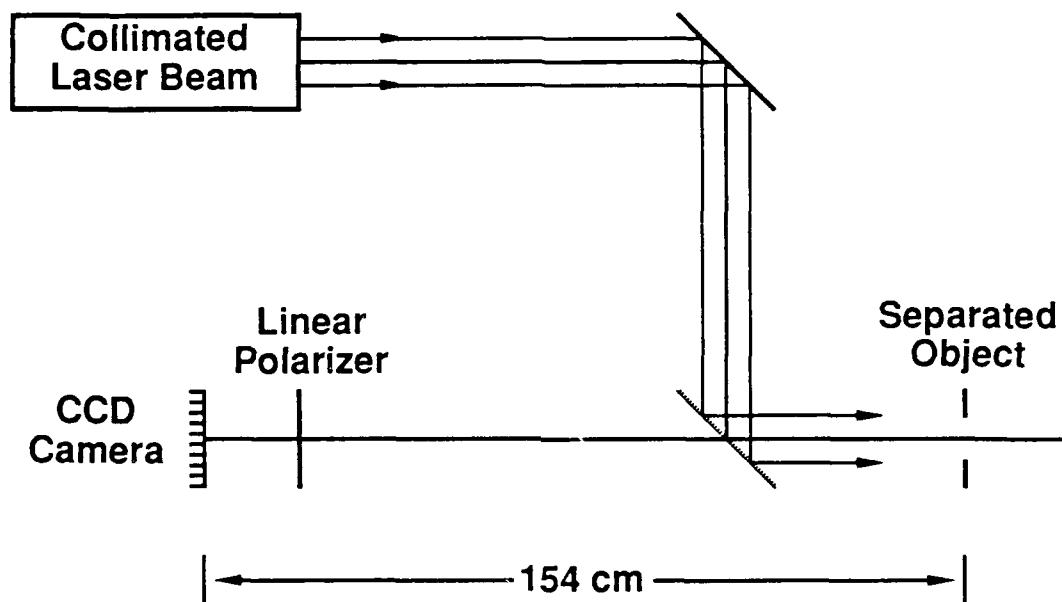


Figure 3-2. Experimental setup used for separation measurements.

pixel spacing of the detector array was $S_x = 21.3 \mu\text{m}$ in the horizontal direction and $S_y = 18.0 \mu\text{m}$ in the vertical direction. These pixel spacings are well under the upper limits established in Eq. (3-13).

If, for example, the autocorrelation sidelobe has a centroid of \bar{y} in the vertical direction, the angular separation of the objects in the vertical direction is

$$\theta_y = \frac{\lambda \bar{y}}{S_y L_y} , \quad (3-16)$$

where L_y is the number of detector elements in the vertical direction of the array including zero padding. For example, if the speckle data array has 64×64 pixels and is imbedded in a 256×256 array, the value of L_y is 256.

In the experiments, we took sections of the speckle data with sizes of 128×128 , 64×64 , and 32×32 pixels and imbedded this data into an array of zeros with size 256×256 pixels. The left column of Fig. 3-3 shows examples of the speckle data for the different data array sizes. The center and right columns show the autocorrelation estimates for two independent realizations of the speckle data. Notice that the quality of the autocorrelations decrease as the size of the speckle data array decreases.

The autocorrelation centroids were computed for the various speckle data array sizes and were compared to the expected centroids. The results of this experiment are shown in Fig. 3-4. From Eq. (3-16) the expected object separation is $\bar{y} = 35.4$ pixels. This is shown as the horizontal line in the Fig. 3-4. The horizontal axis of Fig. 3-4 gives the dimension of the speckle data array size. For each of the array sizes (32, 64 and 128), the centroid was computed for three realizations of the speckle data. Notice that the accuracy increases with the size

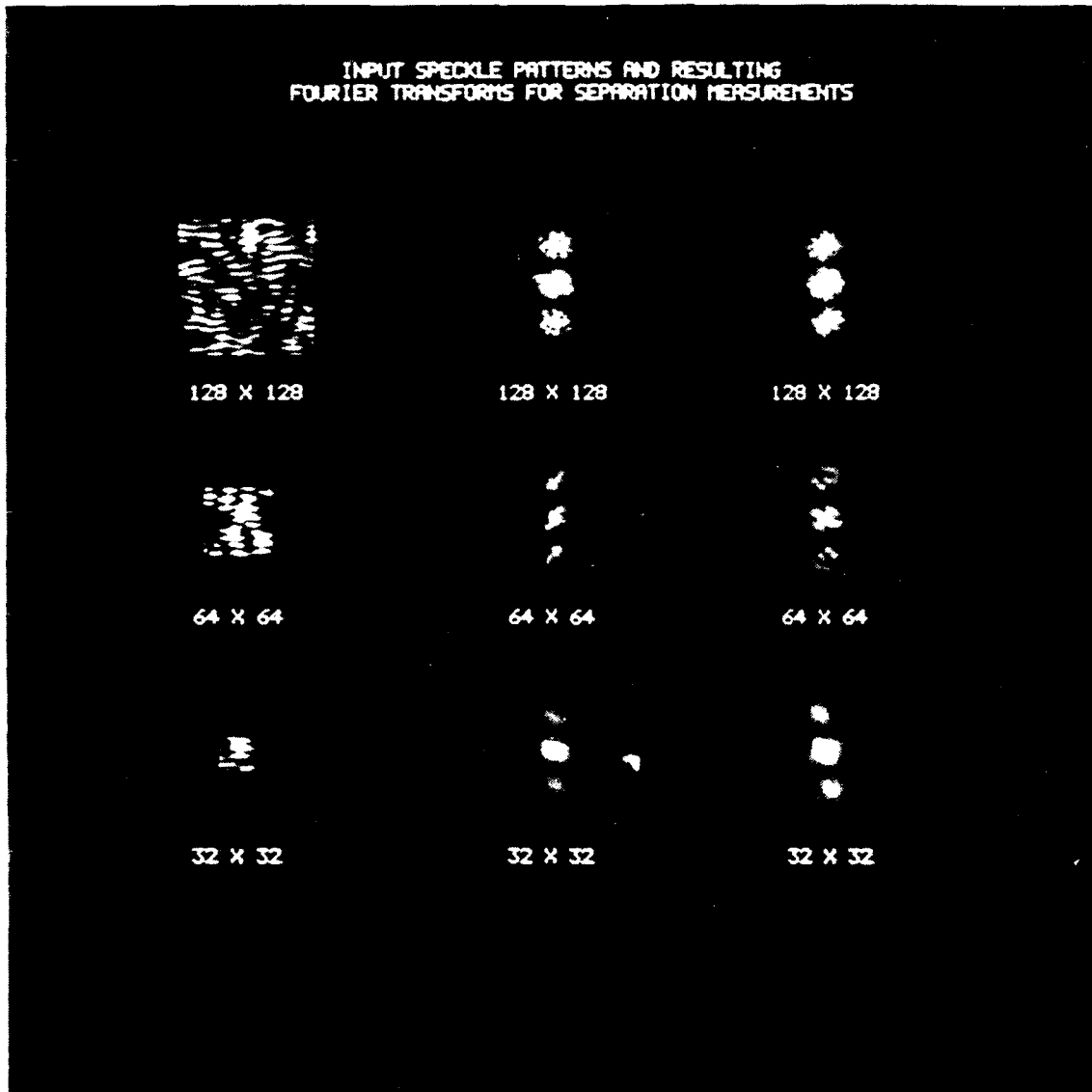


Figure 3-3. Examples of various sized speckle patterns are shown in the left column. Two realizations of the autocorrelation from independent speckle patterns are shown in the center and right columns.

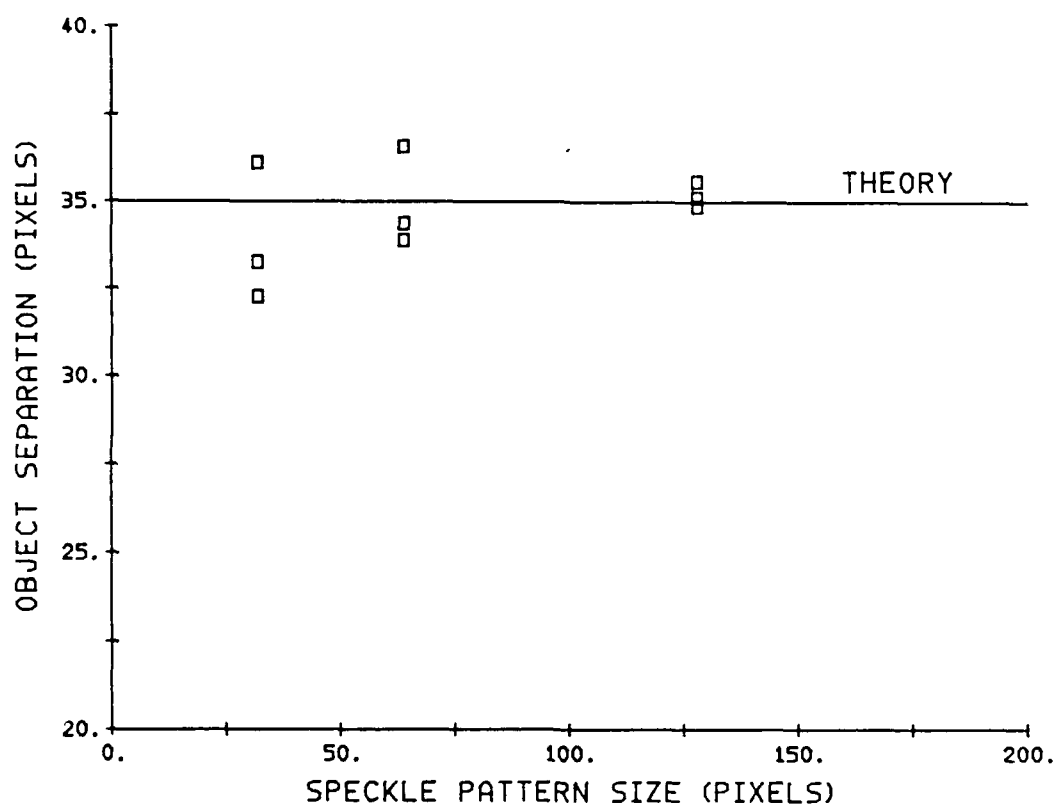


Figure 3-4. A comparison of experimentally measured separation to the true value for various speckle pattern sizes. For each size 3 independent realizations of the separation measurement are shown.

of the data array. For the largest array size, all of the separation measurements appear within one pixel of the true value. For comparison, the smallest array size (32) is roughly 4 times the size of the minimum aperture required to resolve the separation as dictated by the Rayleigh criterion in Eq. (3-1).

REFERENCES

- 3.1 D.N. Grimes and B.J. Thompson, "Two-Point Resolution with Partially Coherent Light," J. Opt. Soc. Am 57, 1330-1334 (1967).
- 3.2 J.W. Goodman, "Statistical Properties of Laser Speckle Patterns," in Laser Speckle and Related Phenomena, J.C. Dainty, ed. (Springer-Verlag, Berlin, 1984), Sec 2.5.1.
- 3.3 M. Born and E. Wolf, Principles of Optics, 5th ed. (Pergamon, Oxford, 1975), Chap. 10.

PHASE RETRIEVAL FOR A COMPLEX-VALUED OBJECT
USING A LOW-RESOLUTION IMAGE

4.1 SUMMARY

It is very difficult to reconstruct an image of a complex-valued object from the modulus of its Fourier transform (i.e., retrieve the Fourier phase) except for some special cases. Using additionally a low-resolution intensity image from a telescope with a small aperture, a fine-resolution image of a general object can be reconstructed by a two-step approach. First the Fourier phase over the small aperture is retrieved using the Gerchberg-Saxton algorithm. Then that phase is used, in conjunction with the Fourier modulus data over a large aperture together with a support constraint on the object, to reconstruct a fine-resolution image (retrieve the phase over the large aperture) by the iterative Fourier transform algorithm.

4.2 BACKGROUND

Phase retrieval from a single intensity distribution for the case of complex-valued objects arises in a number of applications such as holography, wavefront sensing, and imaging with coherent illumination. If the support of the object (the set of points over which it is nonzero) is well known or of a favorable type, then it is often possible to reconstruct an image of the object from the modulus of its Fourier transform (the square root of the Fourier intensity) using the iterative Fourier transform algorithm [4.1]. Favorable support constraints include polygons with no parallel sides (particularly triangles), which must be known a priori [4.1,4.2], and supports with separated parts, which need not be known a priori [4.1,4.3]. If, on the other hand, the object has a polygonal support that is not known very well a priori, or if the object has tapered edges, then both the

ability to converge to a solution and the quality of the reconstructed image deteriorate [4.1,4.4-4.6]. This contrasts sharply with the case of real, nonnegative objects, for which phase retrieval is much easier [4.7-4.9]. Image reconstruction is also possible if the complex-valued object has a strong glint or glints (for example, a single glint well-separated from the object gives rise to a hologram which can be reconstructed easily [4.10]).

In this chapter we show that even the difficult types of complex-valued objects can be reconstructed if one has a low-resolution intensity image of the object, taken through a telescope having a small aperture contiguous with the Fourier intensity measurements, to supplement the Fourier intensity data. In Section 4.3 an example is given of an optical system that would produce the desired measurements. Section 4.4 describes the data processing steps required to reconstruct a fine-resolution image. A two-step method is used, employing an accelerated version of the Gerchberg-Saxton algorithm [4.11-4.15] in the first step and a modified version of the iterative Fourier transform algorithm [4.1,4.7-4.9,4.13-4.15] in a second step. This new modification, the expanding weighted modulus algorithm, was necessary for convergence with a reasonable number of iterations. In Section 4.5 an example of reconstructing an image using this approach is given, and in Section 4.6 are conclusions.

4.3 OPTICAL SENSOR CONFIGURATION

Suppose that the object being imaged is illuminated by a coherent laser and is far away so that the relationship between the optical field at the object, $f(x)$, and that in the aperture plane of the optical receiver, $F(u)$, is approximately a Fourier transform [4.16]. Here u and x are both two-dimensional coordinates: u in the aperture plane and x in the object or image plane. (If it is a Fresnel

transform, then the method described here will work with minor modifications [4.17].) Figure 4-1 depicts an example of an optical receiver that gathers the type of data needed for the reconstruction described here. An array of light-bucket detectors (shown with field lenses in front of them) samples the intensity of the optical field in the aperture plane. In order to adequately sample the intensity of the speckle pattern in the aperture plane, there must be at least two detectors per speckle width in each dimension (as determined by the wavelength of the laser, the distance to the object, and the object diameter). Since only the intensity is detected, these measurements are independent of any phase errors that may be present due to atmospheric turbulence in front of the aperture (assuming that atmospheric scintillation is negligible) or due to misalignment of the detector array. In addition, imbedded in the array (or contiguous with the array on the edge of the array) is a small-aperture diffraction-limited telescope. If located on earth, the small-aperture telescope could be diffraction-limited by virtue of having an adaptive optics system that compensates for atmospheric turbulence in real time. Such an adaptive optics system may not be practical for a telescope with an aperture the size of the entire large aperture. If in space, then adaptive optics would not be needed for the small telescope. A beamsplitter in the small telescope allows for the detection of intensity simultaneously in two planes: the usual focal plane, where there exists a diffraction-limited image of the object, and a demagnified image of the aperture plane. The diffraction-limited image of the object has low resolution since it comes from a small aperture. It is assumed that the intensity measurements are made over a short enough time that the object and the receiver are essentially fixed in space relative to one another.

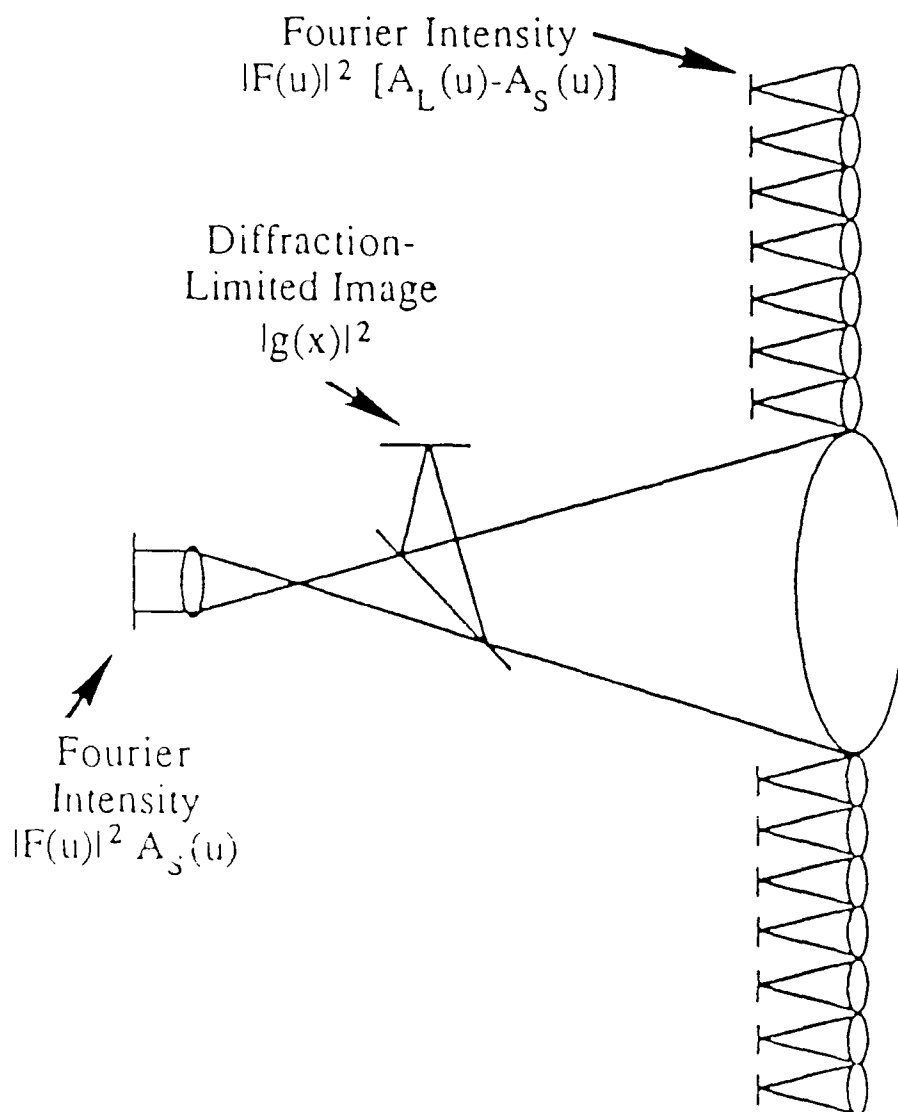


Figure 4-1. Optical sensor configuration. Data collected for a coherently-illuminated object (not shown, located far to the right) includes aperture-plane (Fourier) intensity and a low-resolution diffraction-limited intensity image from a small-aperture telescope.

In summary, the optical receiver makes the following intensity measurements. Letting A_L (a binary function) denote the entire large aperture (including the small aperture) and A_S denote the small aperture, we have $|F(u)|^2 [A_L(u) - A_S(u)]$ from the light-bucket detectors, $|F(u)|^2 A_S(u)$ from the reimaged aperture of the small telescope, and $|g(x)|^2$, the intensity of the low-resolution image, where $g(x) = a_S(x) * f(x)$, $a_S(x)$ is the Fourier transform of $A_S(u)$ and $*$ denotes convolution.

4.4 DATA PROCESSING STEPS

Figure 4-2 shows a block diagram depicting how these three intensity measurements (or their square roots, the moduli or magnitudes) are used to retrieve the phase over the large aperture and reconstruct a fine-resolution image. A support constraint for the object is computed (in either of two ways), and the phase over the small aperture is retrieved. Then the fine-resolution image is reconstructed using all the available information. In what follows each of these steps is described in some detail.

4.4.1 Support Estimation

A support constraint for the object can be obtained in one of two ways: from the low-resolution image or using a triple-intersection of the autocorrelation support [4.3,4.18].

An estimate of the support of the object can be obtained from the low-resolution image, $|g(x)|^2$, by thresholding it at an appropriate level (i.e., the support function is set equal to unity where $|g(x)|^2$ exceeds the threshold and zero elsewhere). If the threshold level is set too high, then the support of the object is underestimated. If the threshold level is set too low, then the support is overestimated

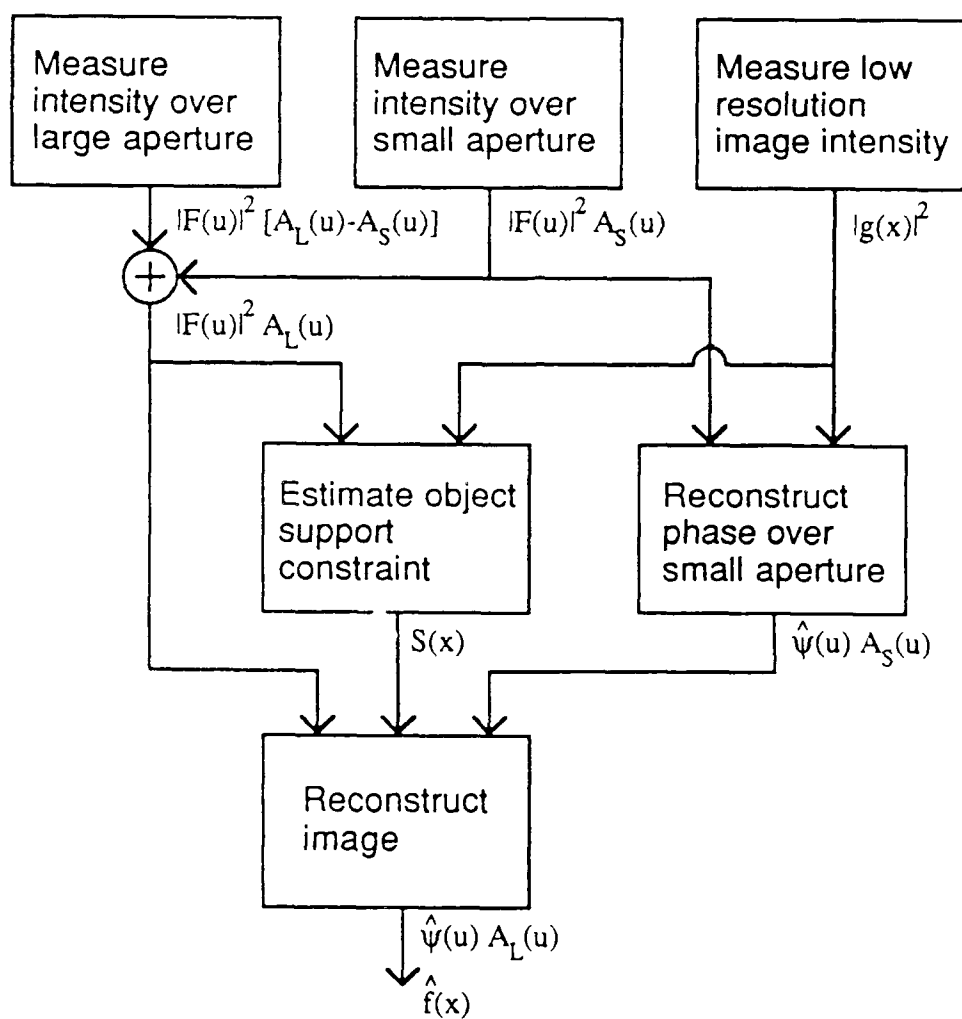


Figure 4-2. Data processing steps to reconstruct a fine-resolution image (retrieve the phase in the aperture plane) from the intensity measurements.

because of noise and sidelobes due to diffraction. The sidelobes can be minimized by placing an apodization (weighting) across the small aperture, but at the expense of optical efficiency and resolution of the low-resolution image.

The method we find useful for selecting the threshold level is as follows. Several candidate thresholded low-resolution images are computed using different threshold values. When the threshold value is too high, small changes in the threshold value tend to cause small changes in the area of the thresholded image. When the threshold falls below the value needed to pick up the noise and/or sidelobes, then the area of the thresholded image grows very rapidly, spreading over the entire image space, and the thresholded image breaks up very rapidly. This is illustrated by the example shown in Figure 4-3 for the case of a telescope with a small circular aperture (a diameter-16 circle imbedded in a 128 x 128 array). Thus a good choice of threshold value is one just larger than the values for which the area of the thresholded image grows rapidly. Figure 4-4 shows the corresponding results for the case of a weighting function across the small aperture. The weighting function was chosen to be the autocorrelation of a circle of half the diameter of the small aperture; that is, the weighting function falls to zero at the edges of the small aperture. With the aperture weighting included, the diffraction sidelobes are greatly reduced and the area of the thresholded image is much less sensitive to changes in the threshold value, making the aperture weighting worthwhile despite the loss of resolution it causes.

For the case of diffusely scattering objects, the Fourier intensity is a speckle pattern and the image (the low-resolution image as well as the fine-resolution image), is speckled [4.19], as can be seen in Figures 4-3 and 4-4. Nulls in the thresholded image due to speckle nulls in $|g(x,y)|^2$ can be eliminated by convolving the thresholded

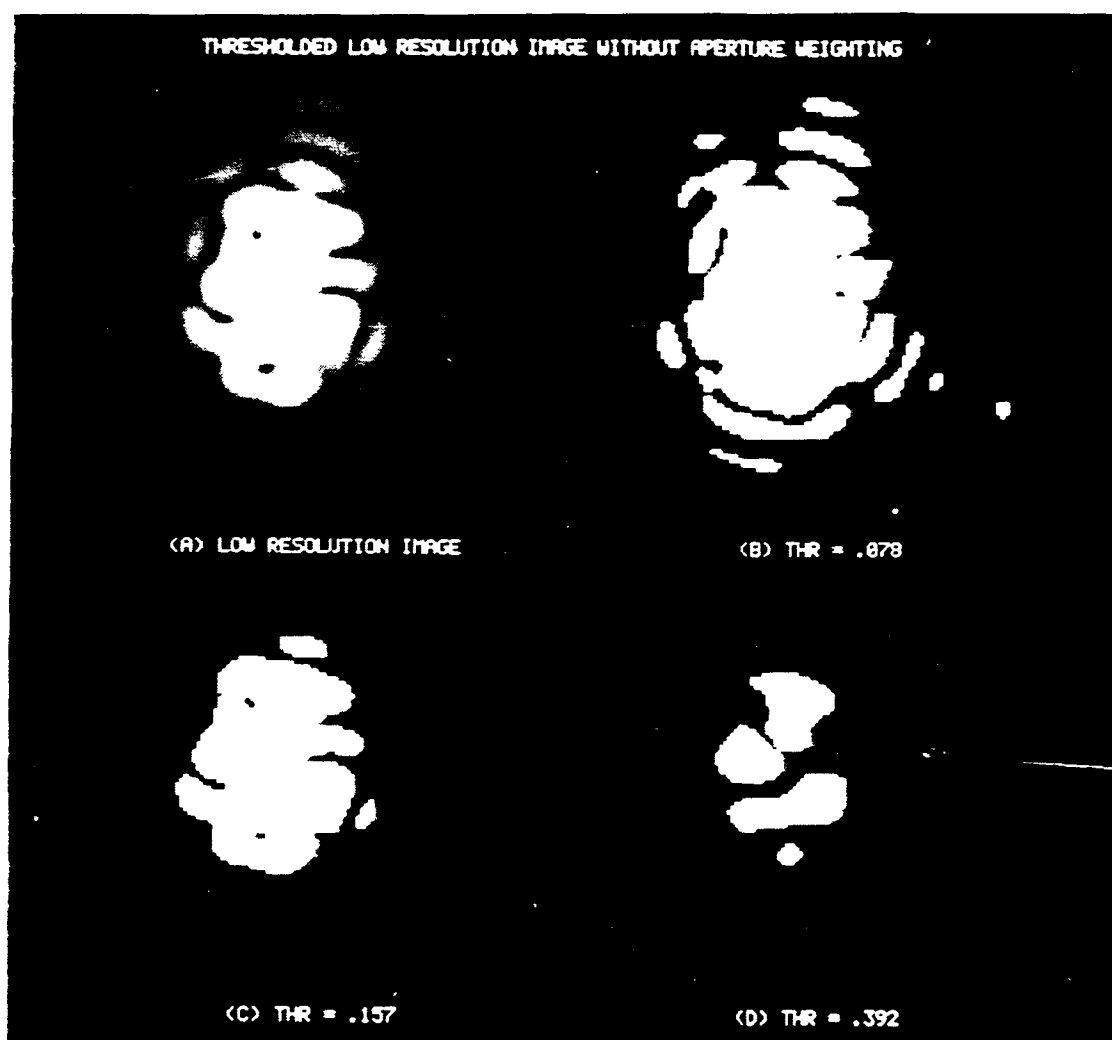


Figure 4-3. Thresholding the low-resolution intensity image to estimate a support constraint, with no weighting on the small aperture. (A) Diffraction-limited low-resolution image (overexposed in order to show the sidelobes that extend beyond the support of the object); (B)-(D) thresholded images, with threshold values equal to (B) 0.078, (C) 0.157, and (D) 0.392 of the maximum value of the image.

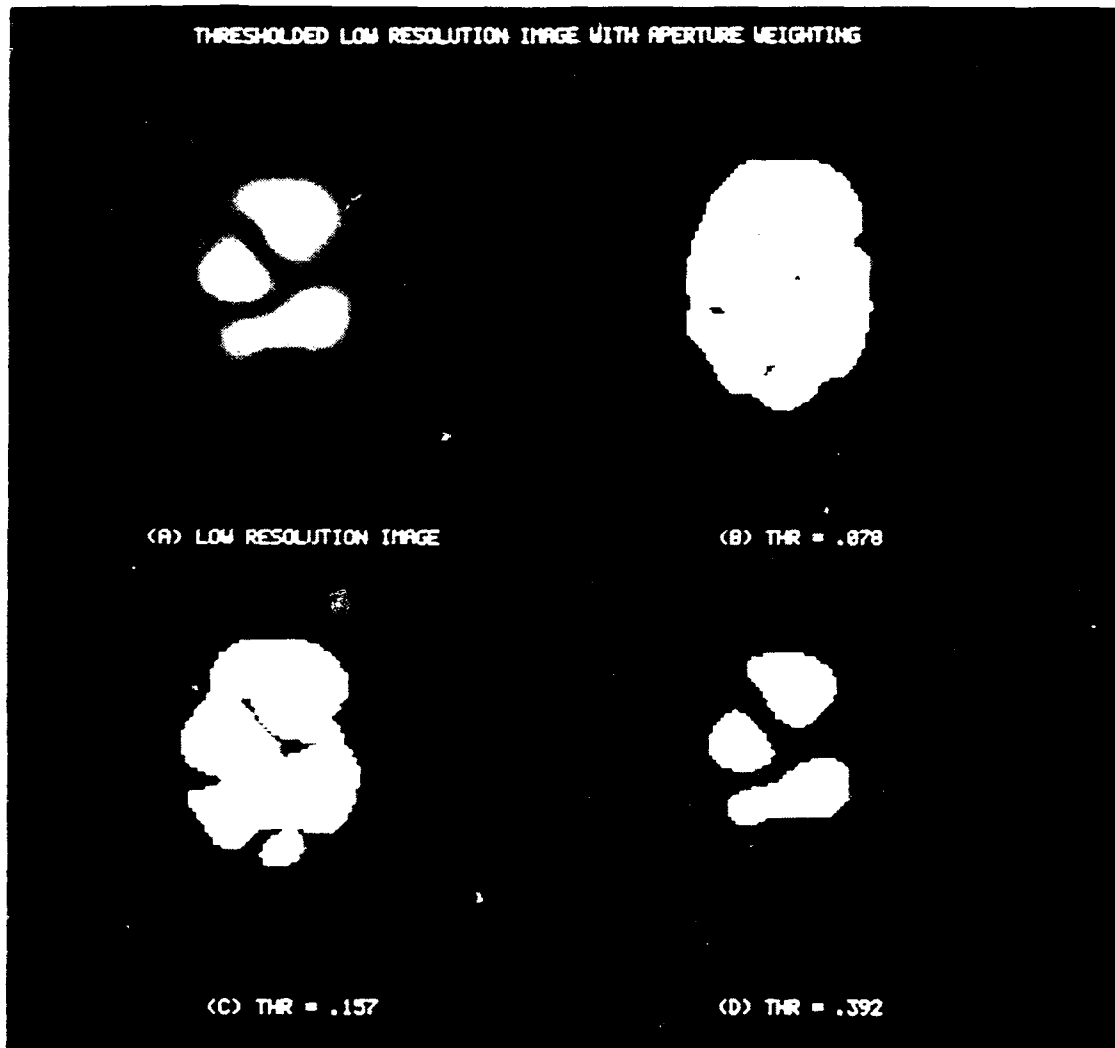


Figure 4-4. Thresholding the low-resolution intensity image to estimate a support constraint, with a weighting on the small aperture. (A) Diffraction-limited low-resolution image (not overexposed); (B)-(D) thresholded images, with threshold values equal to (B) 0.078, (C) 0.157, and (D) 0.392 of the maximum value of the image.

image with a small circle, then rethresholding, as illustrated in Figure 4-5. The estimate of the support of the object, shown in Figure 4-5(C), is used as a support constraint in the final step of fine-resolution image reconstruction by the iterative Fourier transform algorithm. Since this support constraint is only approximate and may be too small, it is often useful to enlarge the support constraint to ensure that the object fits within it. We typically enlarge the support constraint by adding pixels to the edges of the initial support constraint, as shown by the example in Figure 4-5(D).

A second method of generating a support constraint, which uses the Fourier intensity over the entire aperture, is the method of triple intersection of the autocorrelation support [4.3]. First the Fourier intensities over the small aperture and from the light-bucket detectors are combined to arrive at the intensity over the entire aperture. This intensity is inverse Fourier transformed to obtain a fine-resolution autocorrelation of the object. The autocorrelation function is thresholded and the nulls due to speckles are eliminated in a way similar to that shown in Figure 4-5. Noise and sidelobes outside the true autocorrelation support are eliminated to the extent possible by a similar method operating on the complement of the support. The result is an estimate of the support of the autocorrelation. Then three appropriate translates of the autocorrelation support are intersected to arrive at an upper bound on the support of the object [4.3]. In this case the support constraint is not an estimate of the support of the object, but is an upper bound that contains all possible object supports consistent with the support of the autocorrelation.

The support constraint computed from the autocorrelation function is from finer-resolution data and therefore may be more accurate, but it may also be too large since reconstruction of the support of an object from the support of its autocorrelation function is ambiguous



Figure 4-5. Removal of nulls due to speckles in the image. (A) Thresholded image from Figure 4-4 (C), (B) convolution of (A) with a circle of diameter 7 pixels (about half the diameter of a speckle), (C) thresholding of (B) at 0.58 of its peak, (D) enlarged version of (C) that may be used to ensure that the object fits within it.

for wide classes of objects [4.20,4.3]. The thresholded low-resolution image avoids these ambiguity problems, but, being lower resolution, may not be as accurate. Further study is required to determine which of the two methods is better and to devise a way to combine the best features of each into a composite support estimate.

4.4.2 Small-Aperture Phase Retrieval Using Gerchberg-Saxton

The phase, $\Psi(u)$, of the optical field, $F(u) A_s(u)$, in the plane of the small aperture is determined from the intensities in the focal plane and the image of the aperture plane using a variation of the Gerchberg-Saxton algorithm that is accelerated. Figure 4-6 shows a block diagram for the Gerchberg-Saxton algorithms. Here we will refer to the original Gerchberg-Saxton algorithm [4.11,4.12] as GS and the accelerated versions as GS1 and GS2 [4.13-4.15], the latter having the image-domain operation [4.14, Eqs. (9) and (10)]

$$\tilde{g}_{k+1}(x) = g'_k(x) + \beta \left[2 |g(x)| \frac{g'_k(x)}{|g'_k(x)|} - g'_k(x) - |g(x)| \frac{\tilde{g}_k(x)}{|\tilde{g}_k(x)|} \right] \quad (4-1)$$

where β is a constant, $|g(x)|$ is the modulus of the low-resolution image, $\tilde{g}_k(x)$ is the input image to the k th iteration and $g'_k(x)$ is the output image from the k th iteration. The rates of convergence for these three algorithms were compared and β was optimized. The differences in the convergence rates are affected not only by the choice of β but also by the choice of the random phase used as the initial estimate. It was found that GS2 generally converges much faster than GS1 which in turn converges significantly faster than GS. A better method than using any single algorithm is to combine GS2 and GS: perform several iterations with GS2, which initially converges quickly, then finish off with several iterations of GS, which is more

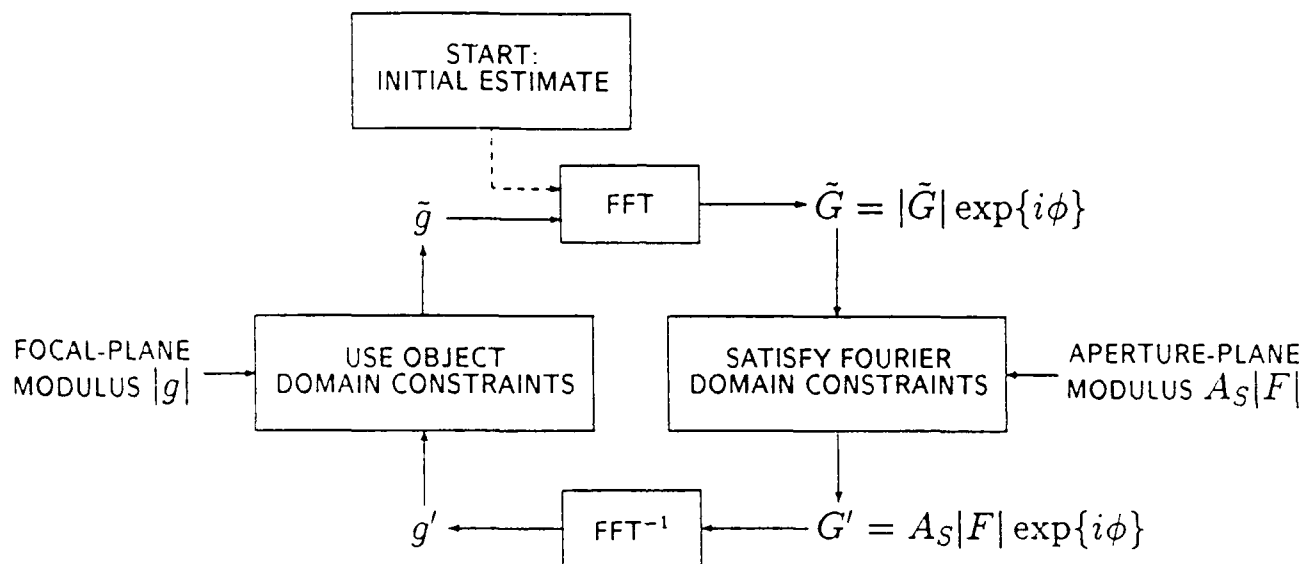


Figure 4-6. Block diagram of the Gerchberg-Saxton algorithms. The object domain constraint is the square root of the measured intensity of the low-resolution image and the Fourier constraint is the square root of the measured intensity over the small aperture.

stable and converges to a smaller error. For these algorithms the object domain error metric (ODEM), a normalized root-mean-squared (RMS) error, is given by

$$\text{ODEM}^2 = \frac{\sum_x \left[|g'_k(x)| - |g(x)| \right]^2}{\sum_x |g(x)|^2} \quad (4-2)$$

which is a measure of how close the output image modulus agrees with the modulus of the measured low-resolution image and is the criterion by which we judge whether the algorithm has converged. (A similar error metric in the Fourier domain can also be used.) Note that in order for Eq. (4-2) to be meaningful it is necessary to normalize $|g(x,y)|$ so that it has the same energy (sum of squares) as the Fourier modulus data. The quality measure we use to evaluate the reconstruction results is the absolute error of the complex-valued reconstructed image, also a normalized RMS error, which is given by

$$\text{ABSERR}^2 = \frac{\sum_x |\alpha g'(x - x_0) - g(x)|^2}{\sum_x |g(x)|^2} \quad (4-3)$$

where α is the complex factor, and x_0 is the shift, that minimizes ABSERR. It can be shown that x_0 is given by the location of the maximum magnitude of $r_{g',g}(x)$, the cross-correlation of g' with g ; and $\alpha = r_{g',g}(x_0) / \sum |g(x)|^2$. This absolute error can only be computed in digital simulation experiments for which the true image is known. Although it measures the error in the complex numbers, which includes both magnitude and phase errors, ABSERR correlates well with the standard deviation, σ_ϕ , of the error of the phase retrieved over the small aperture. As shown in the Appendix, the expected relationship, ignoring errors in the modulus, is

$$\text{ABSERR}^2 \approx 1 - \exp(-\sigma_\phi^2) \quad . \quad (4-4)$$

Figure 4-7 shows examples of algorithm convergence. Twenty iterations of either GS2 or GS were followed by 20 iterations of GS. The optimum value of β was found to be about 1.5 to 2. The algorithm is not very sensitive to small changes in the value of β . Retrieval of the phase over the small aperture was found to be relatively fast (only about 30 iterations are required).

To test the sensitivity of the combined algorithm to noise, low light levels (quantum-limited measurements) were simulated by subjecting the intensity measurements in both planes to a Poisson noise process. We chose to simulate the same number of photons in each of the two planes. After scaling the intensity data to have a given expected total number of detected photons, each pixel was replaced with a sample drawn from a Poisson distribution with mean and variance equal to the pixel value.

For these experiments, the object is approximately of size 40×60 pixels imbedded in a 128×128 array. Therefore the intensity of the Fourier transform of the object (computed using an FFT) is a speckle pattern with about 3×2 samples per speckle. The Fourier data was set to zero outside a circle of diameter 16 pixels to simulate the effect of the small aperture (without weighting). Therefore there should be about $\pi 8^2/6 \approx 33$ speckles in the small aperture.

Figure 4-8 shows the convergence of the algorithm for a variety of noise levels. Figure 4-9 shows ABSERR, the quality of the output image, as a function of iteration number for a variety of noise levels. Figure 4-10 shows ABSERR for the reconstructed image as a function of the total number of detected photons. Very good results are obtained for 10^4 or more photons, which corresponds to $10^4/33 \approx 300$ photons per

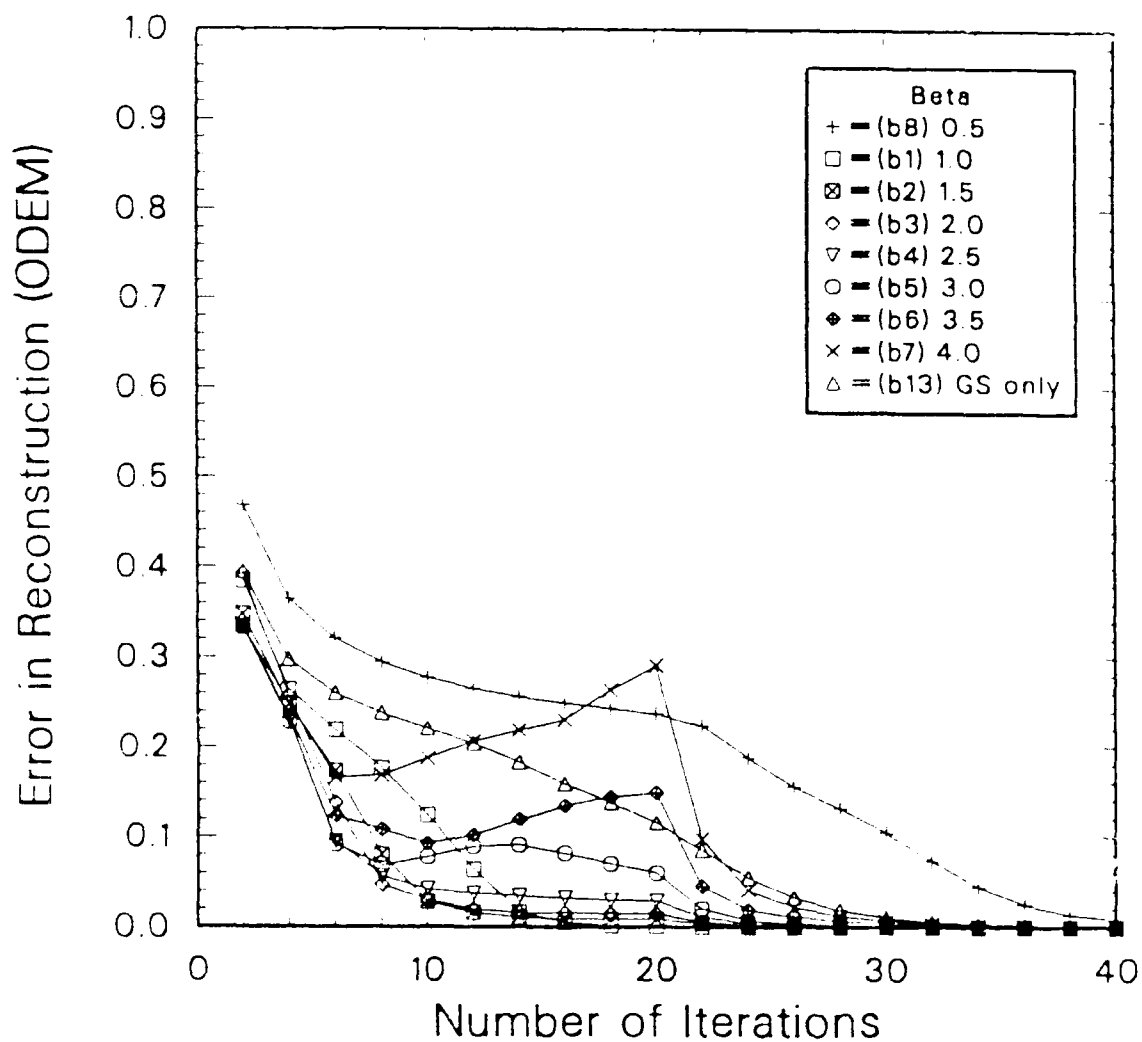


Figure 4-7. Convergence of the Gierchberg-Saxton (GS) and accelerated Gierchberg-Saxton (GS2) algorithms. 20 iterations of either GS2 or GS were followed by 20 iterations of GS. GS2 with feedback parameter $\beta = 1.5$ to 2 converged fastest.

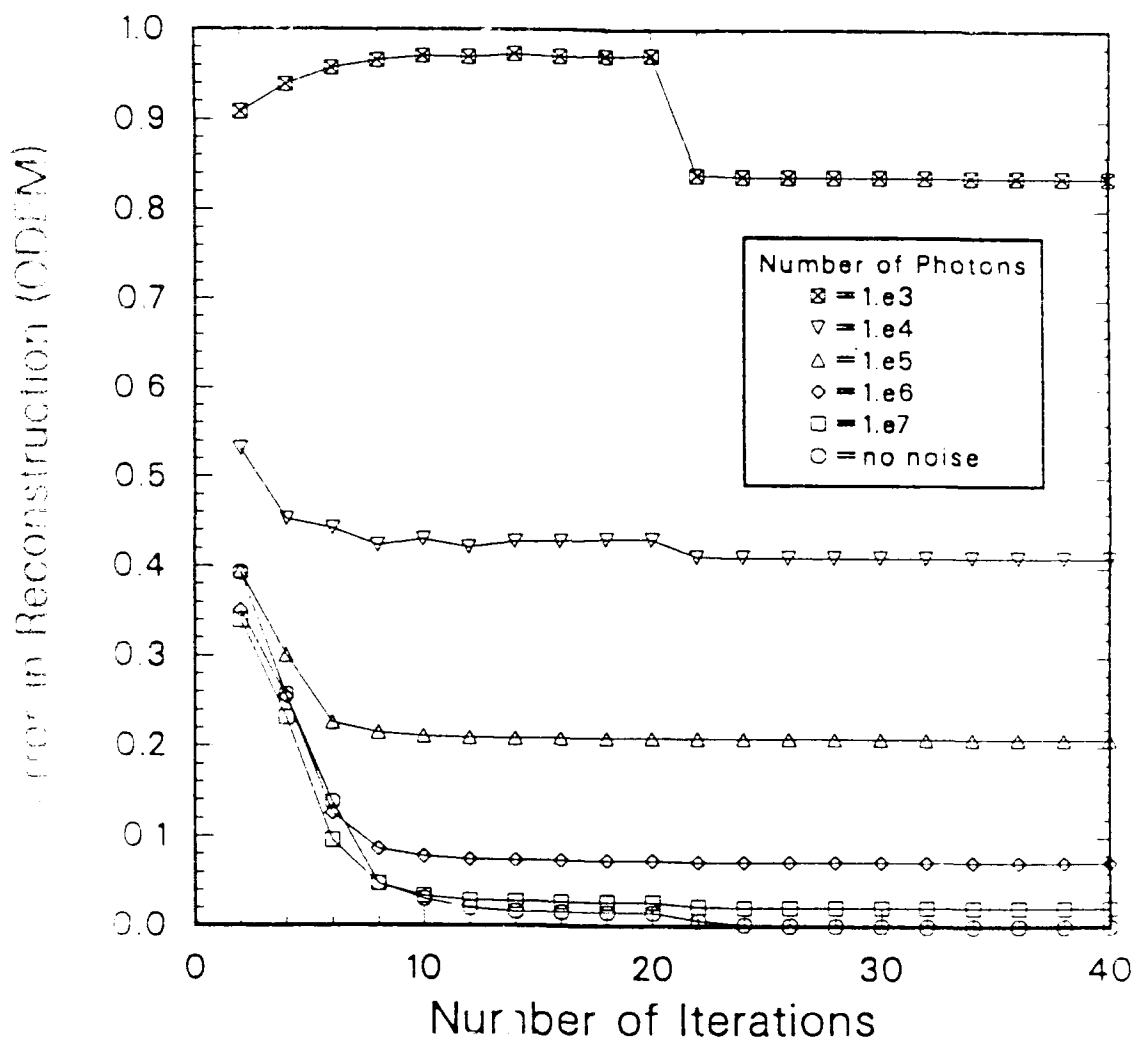


Figure 4-8. Convergence of the combined GS2 and GS algorithms for a variety of light levels.

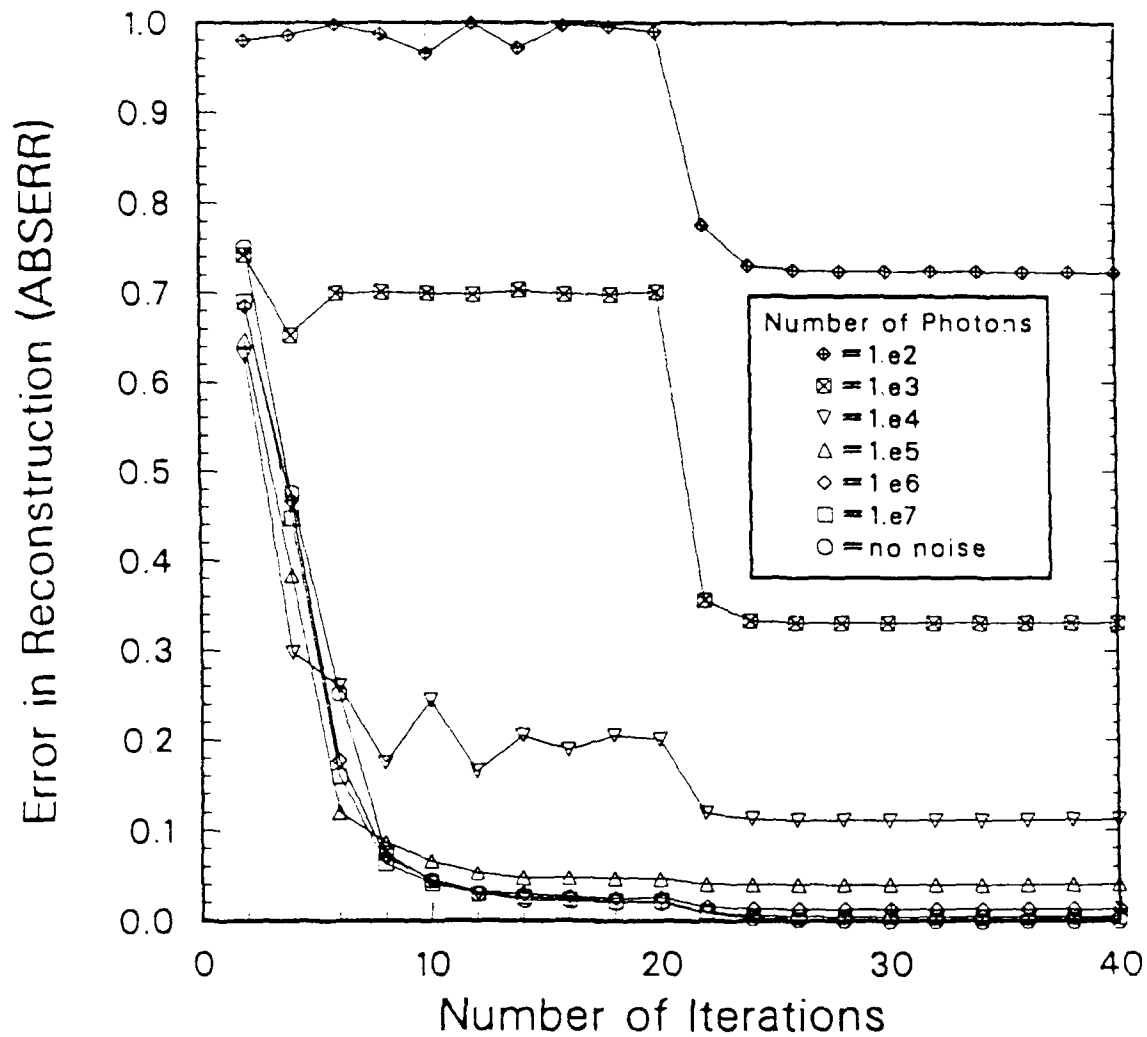


Figure 4-9. RMS error (ABSERR) of the complex-valued reconstructed low-resolution image as a function of iteration number for a variety of light levels.

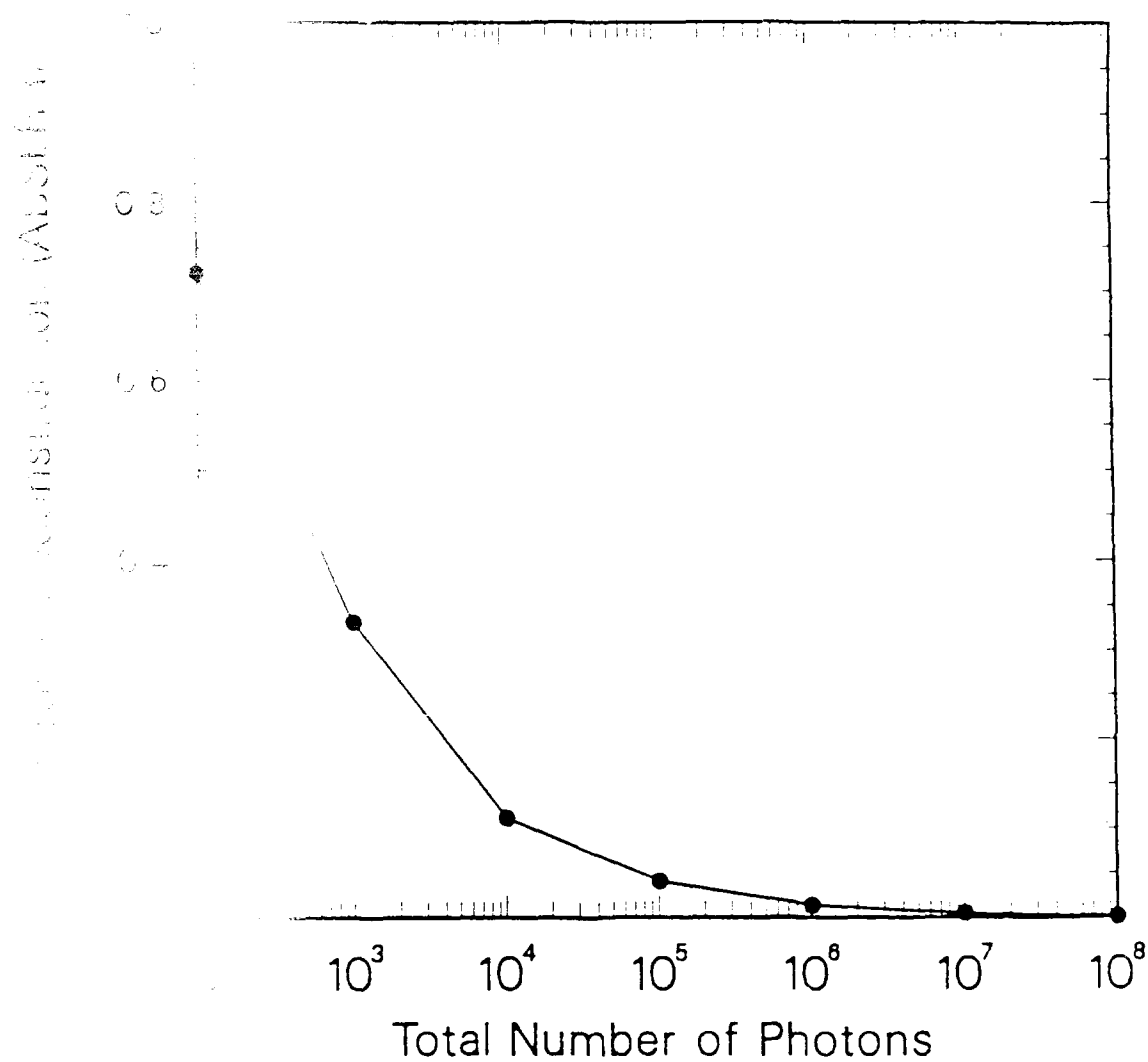


Figure 4-10. RMS error of the complex-valued reconstructed low-resolution image as a function of light level.

speckle. From these results we see that the Gerchberg-Saxton algorithms converge rapidly and are reasonably robust in the presence of noise.

Comparing Figures 4-8 and 4-9, one sees that $ODEM > ABSERR$, which is contrary to what one would ordinarily expect. This can be explained as follows. In our simulation the Fourier- (aperture-) domain data was only slightly oversampled whereas the image-domain data was highly oversampled, that is, there are many pixels per speckle. Therefore, even though both planes have the same average number of photons per speckle (the number of speckles being the same in both domains), the image domain received far fewer photons per pixel. This causes the image-domain data to have a much greater mean-squared error than the Fourier-domain data. Therefore, the output image, $g'(x)$, which is consistent with the Fourier modulus data, has an error appropriate to the lower error of the Fourier modulus data, and it is closer to the true image (as measured by $ABSERR$) than it is to the noisy image-plane modulus data (as measured by $ODEM$).

Since the image domain was highly oversampled, we performed a simple noise filtering. The noisy image intensity was Fourier transformed, the Fourier transform was set to zero outside a circle of diameter 32 pixels (since the ideal complex-valued image has a Fourier transform that is zero outside a circle of diameter 16 pixels), and the result was inverse Fourier transformed to yield a smoothed image with reduced noise. Before taking the square root to compute the image modulus, small negative numbers introduced by the filtering process were set to zero. Figures 4-11 and 4-12 show the convergence and image quality for a set of experiments similar to the ones described above, but using the filtered images. As expected, $ODEM$ was lower for the case of noise filtering than without it. However, $ABSERR$, which is ultimately of greater importance, was slightly better without

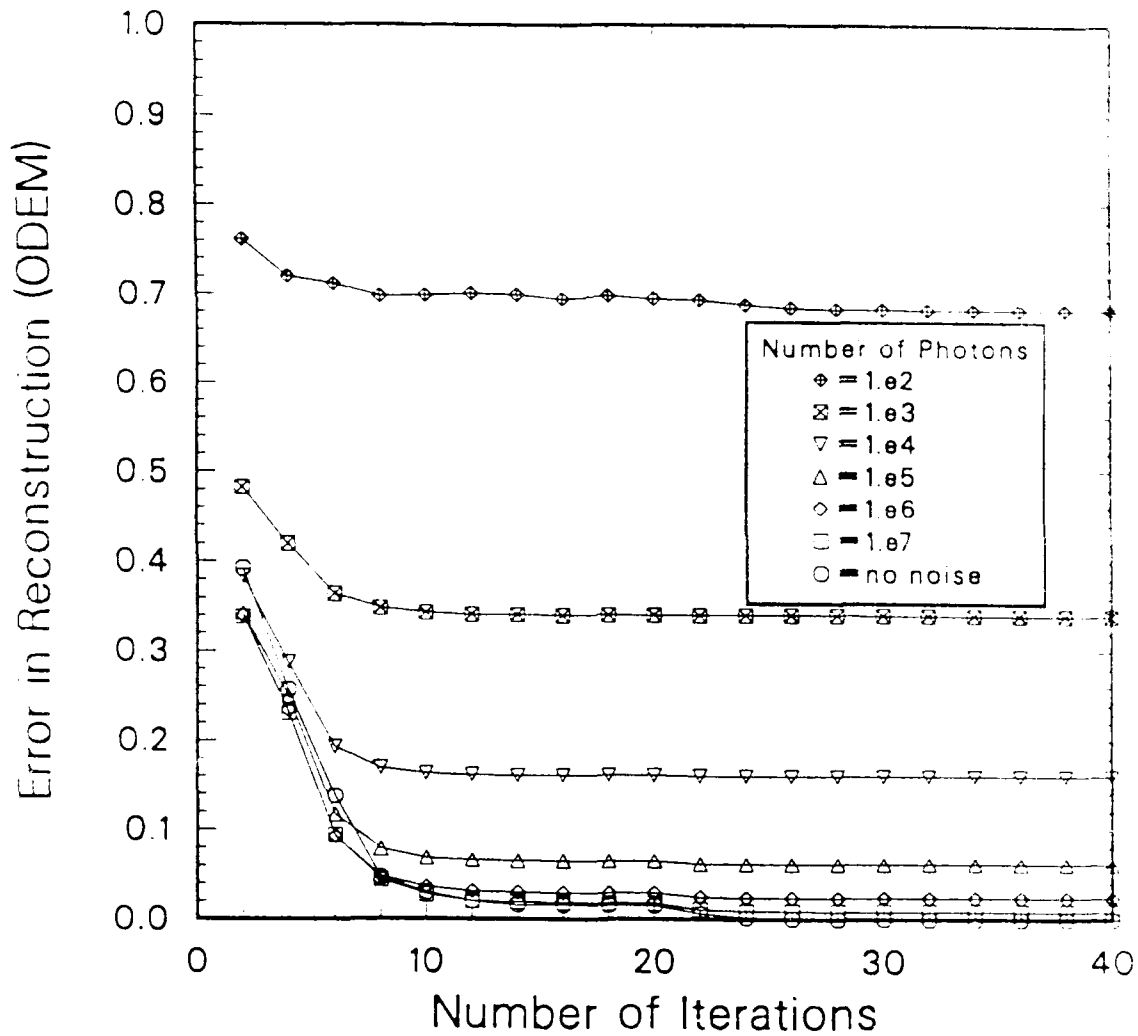


Figure 4-11. Convergence of the combined GS2 and GS algorithms, using a filtered version of the noisy image, for a variety of light levels.

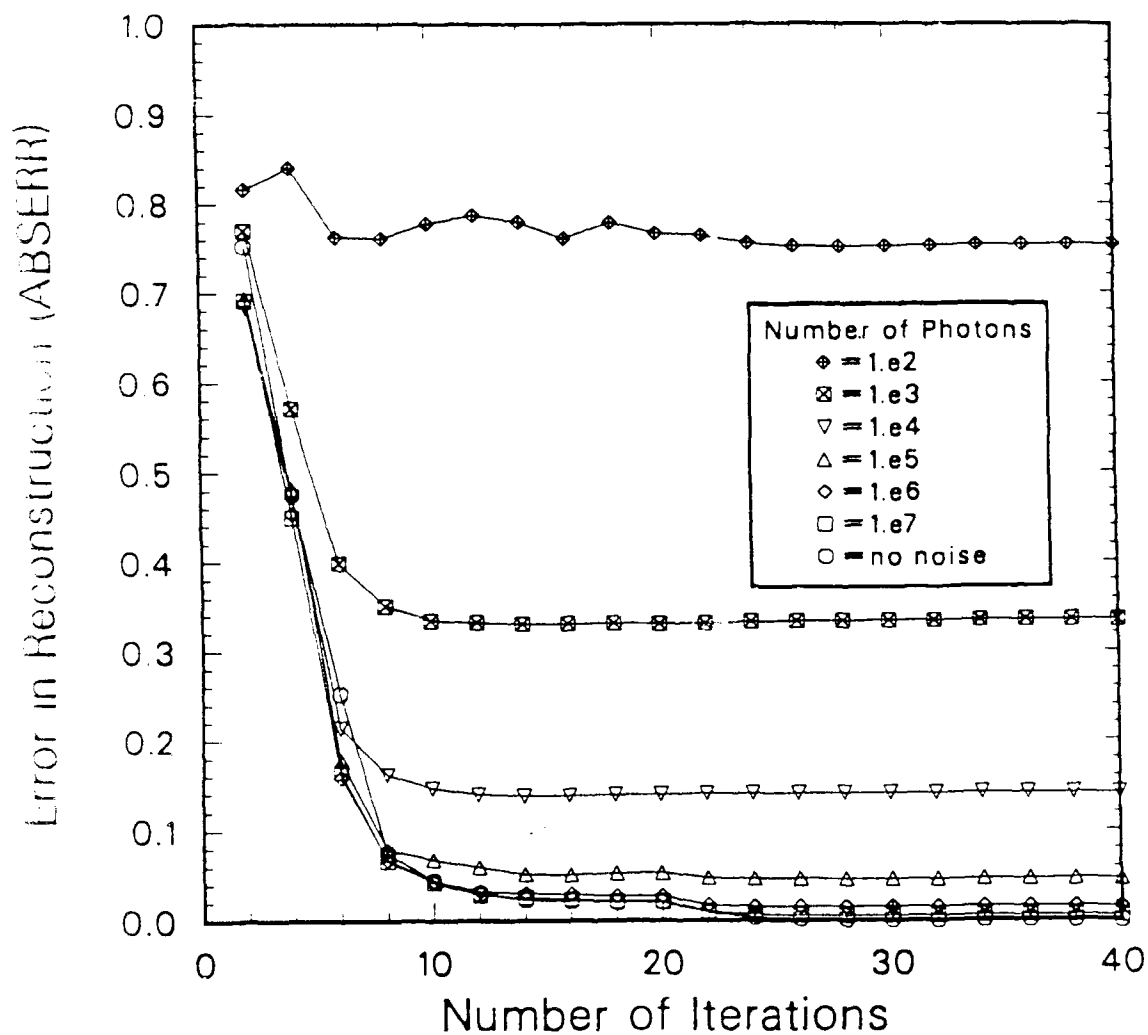


Figure 4-12. RMS error of the complex-valued reconstructed low-resolution image as a function of iteration number, when using the filtered version of the noisy image, for a variety of light levels.

tering; consequently it is better not to allow it in this instance. This filtering issue requires further study.

Note from Figures 4-8 and 4-11 that the initial convergence rate of the algorithm is not monotonically related to the amount of noise present. This results from the fact that some of the random phases used as the initial estimate are closer to the true solution than others.

4.3 Fine-Resolution Image Reconstruction

With all the data in hand -- including the Fourier intensity over the entire aperture, the phase over the small aperture, and the support constraint -- we perform image reconstruction using the iterative Fourier transform algorithm, which seeks a solution consistent with all the data and constraints [4.1, 4.7-4.9, 4.13-4.15]. A block diagram of the algorithm, which is a generalization of the Gerchberg-Saxton algorithm, is shown in Figure 4-13.

When using any phase information in the Fourier domain, the position of the support constraint in the image domain must be chosen to be consistent with the given Fourier phase. (For the conventional phase retrieval with no a priori phase information, it does not matter.) One way to ensure this is to cross-correlate the support constraint with the low-resolution image and use the location of the peak value of the cross-correlation to determine the optimal position of the support constraint.

For the case of a difficult-to-reconstruct complex-valued object, initial attempts to use the small-aperture phase with the iterative Fourier transform algorithm were unsuccessful, whether the phase was just used in the initial estimate or reinforced during the iterations.

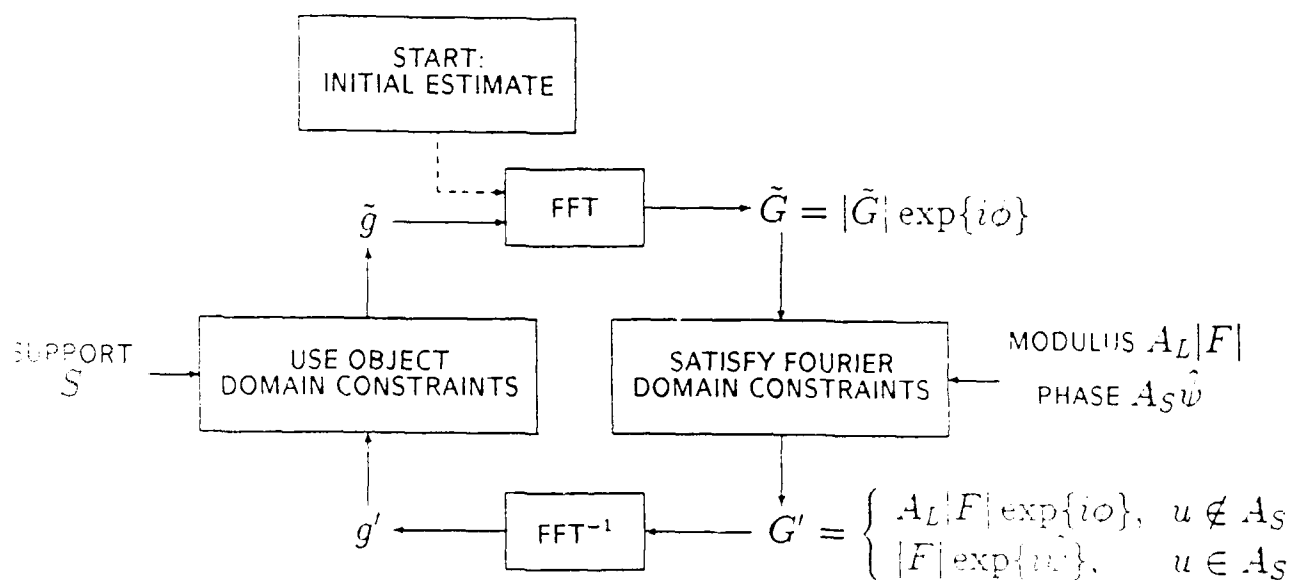


Figure 4-13. Block diagram of the iterative Fourier transform algorithm. The object-domain constraint is a support constraint derived from the measured data, and the Fourier-domain constraints are the square root of the measured intensity over the entire large aperture and the phase retrieved by the Gerchberg-Saxton algorithm over the small aperture.

A possible reason for this failure is the fact that the area of the small aperture is a small fraction of the area of the entire large aperture, and so the incorrect phase over the rest of the aperture overwhelms the influence due to the correct phase over the small aperture.

The following modifications to the algorithm were found to be necessary for a reliable reconstruction. First, in order to reduce impulse-response sidelobes it is advantageous to use a weighting function on the Fourier modulus. This is important since large sidelobes extending beyond the edges of the object support will violate the support constraint and hinder convergence. The Fourier modulus weighting function was chosen to be the autocorrelation of a circle. Initially the diameter of the circle was chosen to be such that the Fourier modulus weighting went to zero over an area just slightly larger than the area over which the small-aperture phase was known. Then a cycle of 30 hybrid input-output iterations followed by 10 error-reduction iterations [4.1] was performed, reinforcing the phase over the small aperture at each iteration. (In practice, reasonably good results can also be obtained if the phase over the small aperture is used for the first iteration only, without being reinforced during later iterations; but better results are obtained by continual reinforcement of the known phase.) This was sufficient to converge to a solution for the phase over the nonzero area of the weighted Fourier modulus, since the phase was already known over most of that area to begin with. Then the Fourier modulus was re-weighted with a weighting function of slightly larger area, and another cycle of iterations was performed. This process was continued until the weighting function encompassed the entire area of the measured Fourier modulus data. Thus the phase retrieval proceeded by a bootstrap approach, with successively larger areas of phase retrieved, and successively finer-resolution images reconstructed, during each cycle of iterations. When

we compute ABSERR by Eq. (4-3), we use for $g(x)$ the diffraction-limited image for the same weighting of the Fourier transform as is being used for the Fourier modulus weighting for that cycle of iterations. We have recently learned that others have also found an expanding weighted modulus approach to be important for reconstructing complex-valued images [4.21].

Ordinarily when reconstructions are performed using a poorly-known support constraint (as is the case here), we have found it best to start with a smaller support constraint for early iterations and expand the support constraint for later iterations. However, when using the expanding weighted modulus algorithm, the images that are reconstructed during the early iterations are larger than the images reconstructed during the later iterations, since for the early iterations the point-spread function is much larger due to the use of a narrow weighting function in the Fourier domain. By experimentation with support constraints that were expanded or shrunk as the iterations progressed, we found that a good strategy was to use a support constraint appropriate for the low-resolution image, and keep it fixed during all the iterations. However, an alternate strategy may be necessary depending on the ratio of the diameters of the small and large apertures or on how the support constraint is formed.

For fine-resolution image reconstruction from the Fourier modulus, for which the only image-domain constraint is a support constraint, the object-domain error metric is given by, instead of Eq. (4-2),

$$ODEM^2 = \frac{\sum_{x \notin S} |g_k'(x)|^2}{\sum_x |g_k'(x)|^2}, \quad (4-5)$$

i.e., the energy outside the support constraint S .

4.5 IMAGE RECONSTRUCTION EXAMPLE

Figure 4-14 shows an example of image reconstruction using the approach described above. In the upper left is the Fourier modulus data (noise free) over the entire aperture, a circle of diameter 64 pixels (imbedded in a 128 x 128 array) with the aperture of the small telescope indicated by a dark circle. In the upper right is the low-resolution image obtained through the small aperture of diameter 16 pixels, weighted by the autocorrelation of a diameter-8 circle. The support constraint, shown in the lower left, was obtained by thresholding the low-resolution image as described above, and the small-aperture phase was estimated using the accelerated Gerchberg-Saxton algorithm. All that information -- the Fourier modulus over the large aperture, the support constraint, and the Fourier phase over the small aperture -- was combined to retrieve the phase over the large aperture by the iterative Fourier transform algorithm using the expanding weighted modulus approach. After 25 cycles of iterations during which the weighting was expanded, plus an additional 6 cycles at the end, for a total of over one thousand iterations, the image shown in the lower center was obtained. It is very close to the true fine-resolution diffraction-limited image, shown in the lower right. Figure 4-15 shows intermediate results with different weightings on the Fourier modulus. The phase is retrieved well for each weighting of the Fourier modulus before the weighting function is expanded, and so at each step a diffraction-limited image (for the resolution given by the weighting function) is reconstructed. Figure 4-16 shows the object-domain error metric (ODEM) and the absolute error (ABSERR) as a function of iteration number. Also indicated is the diameter of the Fourier-weighting function as the iterations progress. It was found that if substantially fewer iterations per cycle were used or if larger jumps in the size of the weighting function were used, then the convergence of the algorithm was much less reliable. Unlike previously

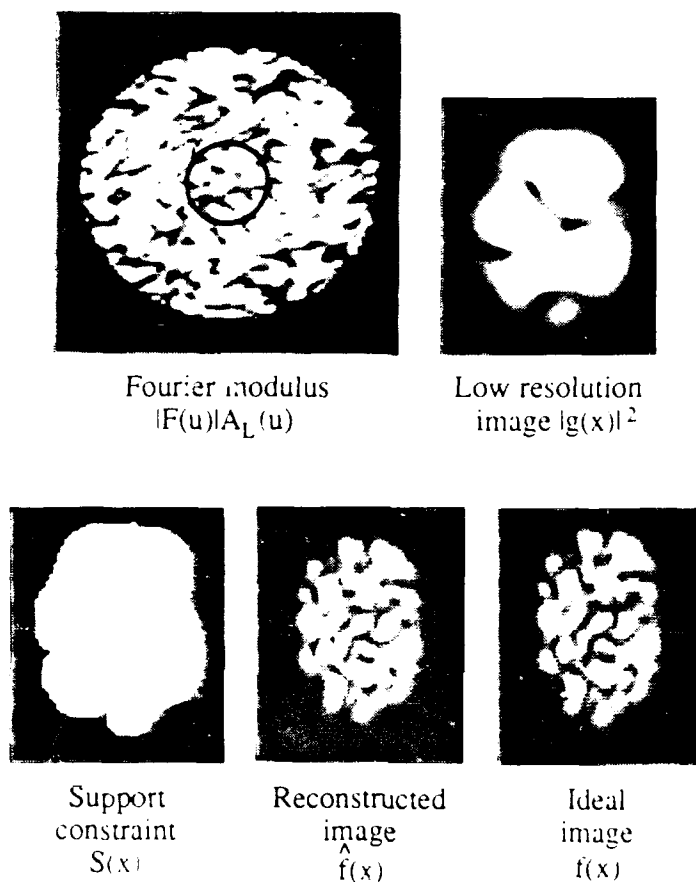


Figure 4-14. Image reconstruction example. (Left to right:) (A) Fourier modulus data over a large circular aperture -- the black circle shows the area of the small aperture; (B) low-resolution image from the small aperture; (C) object support constraint derived from (B); (D) image reconstructed by the Gerchberg-Saxton algorithm followed by the iterative Fourier transform algorithm using (A), (B) and (C); (E) ideal image for comparison.

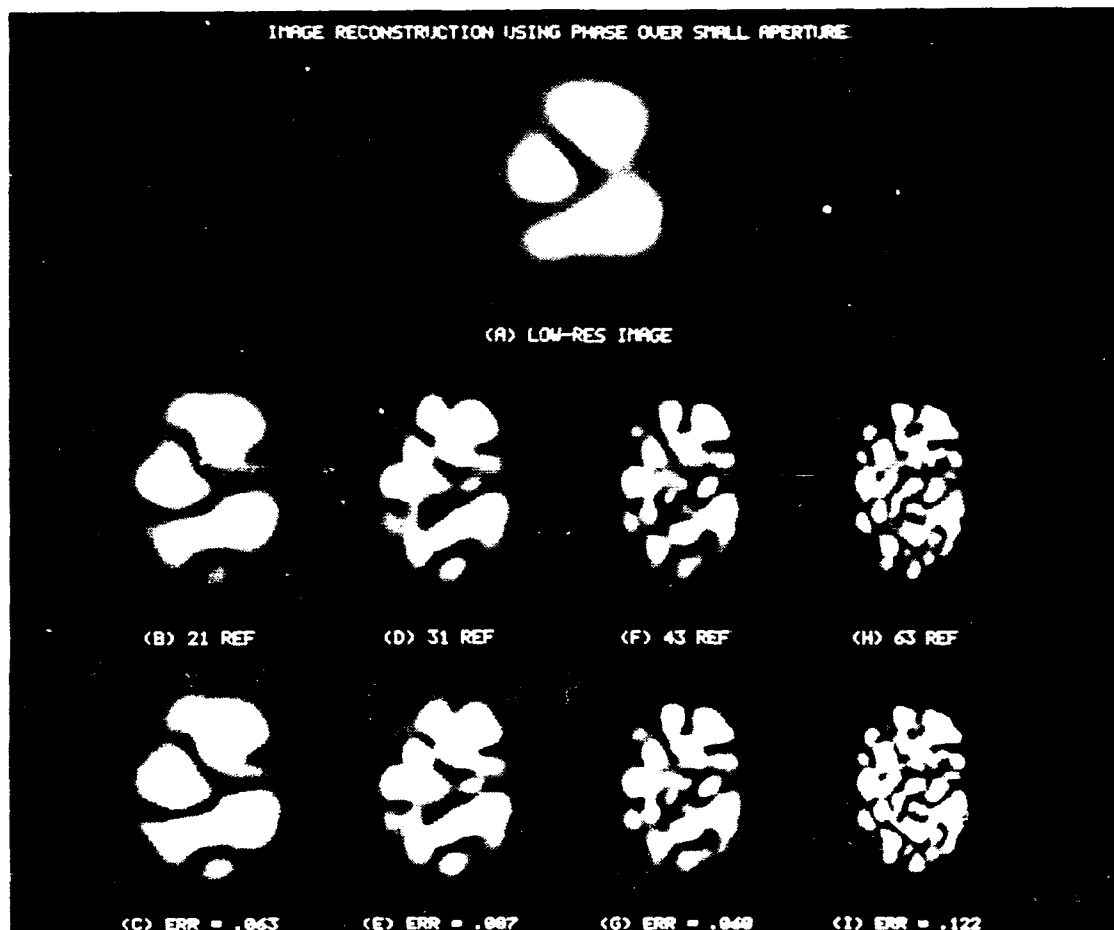


Figure 4-15. Intermediate reconstruction results with different weightings on the Fourier modulus. Bottom row: reconstructed images; top row: ideal images with the same Fourier weighting. Diameter of weighting function in pixels: (A) 21, (B) 31, (C) 43, (D) 63.

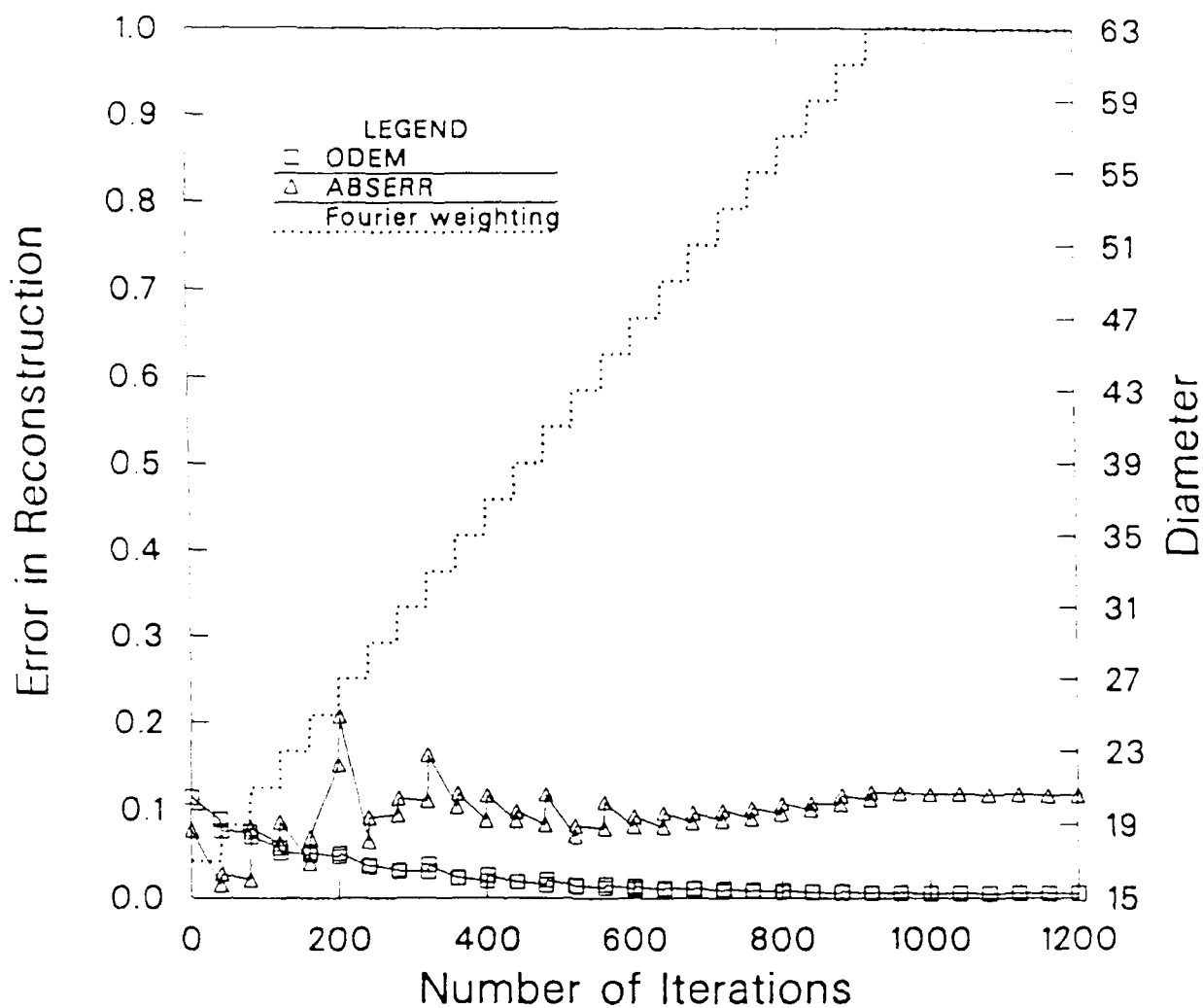


Figure 4-16. Convergence of the iterative Fourier transform algorithm: ODEM (\square) and ABSERR (Δ) (solid lines -- scale at left) and the diameter of the Fourier-modulus weighting function (dashed line -- scale at right) as a function of iteration number.

published results, in which ODEM (or ABSERR) starts out large and decreases with iteration number, here it starts low and stays low since at any given point we are trying to retrieve only an additional thin annulus of phase. A sawtooth behavior is seen since the error jumps up each time the weighting on the Fourier modulus is enlarged.

4.6 CONCLUSION

A complex-valued image of an object with convex support and without bright glints, whose support is not known a priori, is ordinarily very difficult to reconstruct from its Fourier modulus. We have demonstrated that a low-resolution intensity image of the object, taken through a small-aperture telescope contiguous with intensity measurements over a large aperture, can be used to help reconstruct a fine-resolution image. The low-resolution image is used both to determine the Fourier phase over the small aperture and to form a support constraint for the object. The retrieval of the phase over the small aperture, using an accelerated version of the Gerchberg-Saxton algorithm, was found to be not only fast, but also robust in the presence of noise. The reconstruction of the fine-resolution image was also successful, but was found to take a large number of iterations. The determination of its performance in the presence of noise will require further research, which is presently being planned.

Portions of this chapter were presented at the O.S.A. Topical Meeting on Signal Recovery and Synthesis III, N. Falmouth, MA, 14-16 June 1989 [4.22].

REFERENCES

- 4.1 J.R. Fienup, "Reconstruction of a Complex-Valued Object from the Modulus of Its Fourier Transform Using a Support Constraint," J. Opt. Soc. Am. A 4, 118-123 (1987).
- 4.2 J.N. Cederquist, J.R. Fienup, C.C. Wackerman, S.R. Robinson and D. Kryskowski, "Wave-Front Phase Estimation from Fourier Intensity Measurements," J. Opt. Soc. Am. A 6, 1020-1026 (1989).
- 4.3 T.R. Crimmins, J.R. Fienup and B.J. Thelen, "Improved Bounds on Object Support from Autocorrelation Support and Application to Phase Retrieval," accepted for publication in J. Opt. Soc. Am. A (1989).
- 4.4 R.H.T. Bates and D.G.H. Tan, "Fourier Phase Retrieval When the Image is Complex" in Inverse Optics II, A.J. Devaney and R.H.T. Bates, eds., Proc. SPIE 558, 54-59 (1985).
- 4.5 R.G. Paxman, J.R. Fienup and J.T. Clinthorne, "Effect of Tapered Illumination and Fourier Intensity Errors on Phase Retrieval," in Digital Image Recovery and Synthesis, P.S. Idell, ed., Proc. SPIE 828, 184-189 (1987).
- 4.6 R.G. Lane, "Recovery of Complex Images from Fourier Magnitude," Opt. Commun. 63, 6-10 (1987).
- 4.7 J.R. Fienup, "Reconstruction of an Object from the Modulus of Its Fourier Transform," Opt. Lett. 3, 27-29 (1978).
- 4.8 J.R. Fienup, "Phase Retrieval Algorithms: A Comparison," Appl. Opt. 21, 2758-2769 (1982).

- 4.9 J.R. Fienup and C.C. Wackerman, "Phase Retrieval Stagnation Problems and Solutions," J. Opt. Soc. Am. A 3, 1897-1907 (1986).
- 4.10 E.N. Leith and J. Upatnieks, "Reconstructed Wavefronts and Communication Theory," J. Opt. Soc. Am. 52, 1123-1130 (1962).
- 4.11 R.W. Gerchberg and W.O. Saxton, "A Practical Algorithm for the Determination of Phase from Image and Diffraction Plane Pictures," Optik 35, 237-246 (1972).
- 4.12 W.O. Saxton, Computer Techniques for Image Processing in Electron Microscopy (Academic Press, New York, 1978).
- 4.13 J.R. Fienup, "Improved Synthesis and Computational Methods for Computer-Generated Holograms," Ph.D. Thesis, Stanford University, May 1975 (University Microfilms No. 75-25523), Chapter 5.
- 4.14 J.R. Fienup, "Iterative Method Applied to Image Reconstruction and to Computer-Generated Holograms," Opt. Eng. 19, 297-305 (1980).
- 4.15 J.R. Fienup, "Reconstruction and Synthesis Applications of an Iterative Algorithm," in Transformations in Optical Signal Processing, W.T. Rhodes, J.R. Fienup, and B.E.A. Saleh, eds., Proc. SPIE 373, 147-160 (1981).
- 4.16 J.W. Goodman, Introduction to Fourier Optics (McGraw-Hill, San Francisco, 1968).
- 4.17 R. Rolleston and N. George, "Image Reconstruction from Partial Fresnel Zone Information," Appl. Opt. 25, 178-183 (1986).

- 4.18 J.R. Fienup, "Phase Retrieval from Fourier Intensity Data," in Digital Image Recovery and Synthesis, P.S. Idell, ed., Proc. SPIE 828, 13-17 (1987).

- 4.19 J.W. Goodman, "Statistical Properties of Laser Speckle Patterns," Ch. 2 in J.C. Dainty, ed., Laser Speckle and Related Phenomena, Second Edition (Springer-Verlag, New York, 1984).

- 4.20 J.R. Fienup, T.R. Crimmins, and W. Holsztynski, "Reconstruction of the Support of an Object from the Support of Its Autocorrelation," J. Opt. Soc. Am. 72, 610-624 (1982).

- 4.21 B.C. McCallum and R.H.T. Bates, "Towards a Strategy for Automatic Phase Retrieval from Noisy Fourier Intensities," J. Modern Optics 36, 619-648 (1989).

- 4.22 J.R. Fienup and A.M. Kowalczyk, "Phase Retrieval for a Complex-Valued Object Using a Low-Resolution Image," in Topical Meeting on Signal Recovery and Synthesis III, 1989 Technical Digest Series, Vol. 15 (Optical Society of America, Washington, DC, 1989), pp. 142-145.

5
IMAGE RECONSTRUCTION LABORATORY EXPERIMENTS

5.1 SUMMARY

A new method for image reconstruction from Fourier intensity and low-resolution image intensity measurements was introduced in Chapter 4 and computer simulation experiments to demonstrate this method were described. An important next step in the development of this method is the investigation of image reconstruction from experimental data collected in the laboratory. Therefore, an experiment was set up, laboratory data was collected, and image reconstruction procedures were applied with and without the use of the low-resolution image. An image was reconstructed using Fourier intensity measurements alone. Further work to improve data collection procedures is required to reconstruct an image using the additional low-resolution image.

The remainder of this section gives further details. In Section 5.2, it is shown that accurate Fourier intensity data can be collected in the Fresnel zone of the illuminated test object. In Section 5.3, experimental work to verify the linearity and spatial uniformity of the 2-D CCD detector is discussed. The experimental set-up is described in Section 5.4. Necessary data sampling and pre-processing is discussed in Section 5.5 and image reconstruction results are given in Section 5.6.

5.2 FRESNEL ZONE DATA COLLECTION

Image reconstruction procedures based on phase retrieval require measurement of the Fourier intensity of the illuminated object. It is well-known that the Fourier intensity can be measured in the Fraunhofer region with respect to the object [5.1]. However, for imaging of space objects from space-based sensors, the sensor is more likely to be in the Fresnel region than the Fraunhofer region with respect to the

object. For example, for an object of diameter $d = 1 \text{ m}$, illuminated by a laser of wavelength $\lambda = 1 \text{ } \mu\text{m}$ and a sensor at a distance z with aperture diameter $D = 1 \text{ m}$, the Fraunhofer approximation requires [5.1]

$$z \gg \pi d^2 / 4\lambda \approx 1 \text{ Mm} \quad (5-1)$$

while the Fresnel approximation requires [5.1]

$$z^3 \gg \pi (d + D)^4 / 64\lambda \approx (100 \text{ m})^3 \quad (5-2)$$

A sensor at a likely distance of $z = 1 \text{ Mm}$ would therefore easily satisfy the Fresnel, but not quite satisfy the Fraunhofer, approximation. A similar situation exists in a laboratory experiment unless a Fourier transform lens is used between the object and the detector.

When the Fresnel approximation is satisfied, the relationship between the optical field $U_1(x, y)$ resulting from illumination of the object and the field $U_2(u, v)$ at a distance z is [5.1]

$$U_2(u, v) = \frac{\exp(i2\pi z/\lambda)}{i\lambda z} \exp\left[\frac{i\pi(u^2 + v^2)}{\lambda z}\right] \iint U_1(x, y) \exp\left[\frac{i\pi(x^2 + y^2)}{\lambda z}\right] \cdot \exp\left[\frac{-i2\pi(xu + yv)}{\lambda z}\right] dx dy \quad (5-3)$$

The intensity $I(u, v)$ is

$$I(u, v) = |U_2(u, v)|^2 = (\lambda z)^{-2} \left| \iint U_1(x, y) \exp\left[\frac{i\pi(x^2 + y^2)}{\lambda z}\right] \cdot \exp\left[\frac{-i2\pi(xu + yv)}{\lambda z}\right] dx dy \right|^2 \quad (5-4)$$

If phase retrieval is successfully applied to measurements of the Fourier intensity data $I(u, v)$, the complex-valued image reconstructed will be the diffraction-limited image of $U_1(x, y) \exp[i\pi(x^2 + y^2)/\lambda z]$, whereas a diffraction-limited image of $U_1(x, y)$ is desired. (The diffraction limit will be determined by the aperture diameter D over which Fourier intensity data is collected.)

However, the image obtained of $U_1(x, y) \exp[i\pi(x^2 + y^2)/\lambda z]$ can be equally useful to that of $U_1(x, y)$ under the following conditions. If the object is rough compared to the wavelength of the illumination, then the quadratic phase is added to the random phase of $U_1(x, y)$. The intensities of the diffraction-limited images of $U_1(x, y) \exp[i\pi(x^2 + y^2)/\lambda z]$ and $U_1(x, y)$ are then different realizations (speckle patterns) of the same image of the object. If, in addition, it is not desired to use the phase information of $U_1(x, y)$, then either image gives the same information and reconstruction of images from intensity data measured in the Fresnel region of the object is as acceptable as that from data measured in the Fraunhofer region.

5.3 DETECTOR CALIBRATION

It is known from previous work at ERIM that errors in the Fourier intensity data lead to errors in reconstructed images and, if the error is too large, to an inability to reconstruct an image [5.2, 5.3]. Both the optical propagation path from the object to the detector and the detector itself can cause data errors. Propagation path errors depend on the experimental set-up and are discussed in Section 5.4. Possible errors which can be introduced by a detector include nonlinear response to input intensity, spatially nonuniform response, and additive noise. These detector errors are the subject of this section.

A Fairchild CCD3000F camera using the Fairchild CCD222 sensor with 380 by 488 pixels had been used in earlier successful phase retrieval demonstration experiments [5.4] and was chosen for the current

experiments as well. The linearity of the response was carefully measured using a controllable light source and calibrated detector. Spatial uniformity of response was also measured in this way for all pixels. The linearity of the typical CCD pixel was $\pm 2\%$ and the spatial uniformity (standard deviation computed over all pixels) was 1.5% when measured at a light level corresponding to the maximum signal obtainable when still operating in the quasilinear response region. Software was developed so that the response of each pixel could be independently corrected for nonlinearity and bias. However, the correction was found to be so small that it did not affect the results. The standard deviation of the frame-to-frame noise of the Fairchild CCD camera was measured and found to be $\leq 1\%$, again measured at the light level corresponding to the maximum quasilinear response.

5.4 EXPERIMENTAL OPTICAL SET-UP

The experimental optical set-up is shown in Fig. 5-1. An Argon ion laser operating at a wavelength $\lambda = 0.5145 \mu\text{m}$ was used to illuminate a transmissive object consisting of a binary transmittance mask placed in contact with a ground glass. The maximum width of the object was about 10 mm. The transmitted light propagated 1.54 m to a lens L_1 of focal length $f_1 = 1.54$ m. The lens was about 40 mm thick in the center. As explained later in this section, this lens is used to cancel the quadratic phase due to propagation over a distance f_1 . Two apertures A_1 and A_2 were located behind the last surface of the lens at distances of 8 and 22 mm, respectively. For collection of Fourier intensity data, the CCD detector was placed in plane P_1 about 20 mm behind the second aperture. For collection of image data, the optical field at plane P_1 was Fourier transformed by a lens L_2 to a plane P_2 to which the CCD detector was moved. The imaging lens L_2 had a focal length $f_2 = 189$ mm and was positioned so that the planes P_1 and P_2 corresponded to its front and back focal planes, respectively.

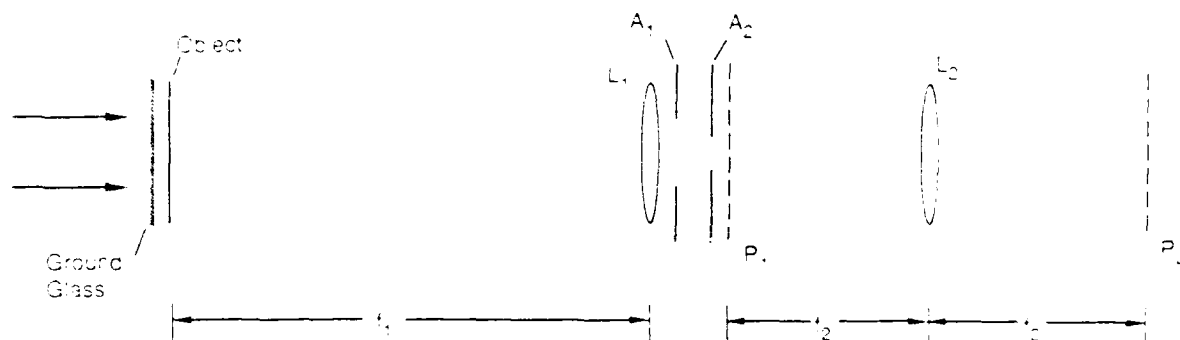


Figure 5-1. Optical Setup for Phase Retrieval Laboratory Experiments.

The data collected consisted of Fourier intensity data over both a large and a small aperture and image data corresponding to both the large and small apertures. The apertures were square and approximately 5 mm and 1.25 mm in width, respectively. The small aperture (A_2) Fourier intensity data and the low-resolution image data (obtained using the small aperture) were input to the Gerchberg-Saxton algorithm described in Chapter 4. For high-resolution image reconstruction, the large aperture (A_1) Fourier intensity data can be input to an iterative Fourier transform algorithm using in addition either (1) an upper bound on object support estimated by the triple intersection method [5.5] or (2) an object support estimated by thresholding the low-resolution image. In the second case, the Fourier phase over the small aperture, estimated by the Gerchberg-Saxton algorithm, can also be used. The first method was investigated via computer simulations in earlier work at ERIM [5.6]. The second method is the new image reconstruction method described in Chapter 4.

Because of its relative simplicity, the optical system was found to be sufficiently stable that many frames of Fourier or image data could be averaged to reduce additive detector noise. The optical path from the object to the detector was enclosed in black velvet to reduce stray light to a very low level.

The object diameter d was about 10 mm, the distance z from the object to the detector in plane P_1 was about 1.5 m, and the maximum detector width D was about 5 mm corresponding to the use of the central 256 by 256 pixels of the detector array. Substituting these values into Eq. (5-2) for the Fresnel approximation gives

$$z^3 \gg (0.17 \text{ m})^2, \quad (5-5a)$$

while the Fraunhofer approximation [Eq. (5-1)] would require

$$z \gg 150 \text{ m} . \quad (5-5b)$$

The detector is therefore in the Fresnel region of the object and Fourier intensity data can be collected as described in Section 5.2.

It should be noted that the small and large apertures are placed in front of the CCD detector by about 20 and 34 mm, respectively. However, the plane P_1 where the Fourier data is collected and the plane P_2 where the image data is collected are related by a Fourier transformation because they are the front and back focal planes of the lens L_2 .

The lens L_1 is required to cancel the quadratic phase [the exponential in front of the integral in Eq. (5-3)] due to propagation from the object to plane P_1 so that the Fourier transformation by the lens L_2 of the optical field in plane P_1 gives a focused image in the plane P_2 . The image formed at plane P_2 will include the quadratic phase described in Section 5.2.

Ideally, the lens L_1 and the two apertures would be located in the plane P_1 . The lens L_1 would then not change the Fourier intensity measurement since the lens and the detector would be in the same plane. Physically, this is impractical. The phase error in plane P_1 caused by the approximately 42 mm distance between the lens L_1 and the plane P_1 can be determined as follows. The optical field immediately after the lens L_1 is given by

$$U(u, v) = \frac{\exp(i2\pi z/\lambda)}{i\lambda z} \iint U_1(x, y) \exp\left[\frac{i\pi(x^2 + y^2)}{\lambda z}\right] \cdot \exp\left[\frac{-i2\pi(xu + yv)}{\lambda z}\right] dx dy \quad (5-6)$$

where, as shown in Fig. 5-1, $z = f_1$. The angular spectrum $A_0(f_u, f_v)$ of this field is [5.1]

$$A_0(f_u, f_v) = U_1(\lambda z f_u, \lambda z f_v) \exp[i\pi \lambda z (f_u^2 + f_v^2)]$$

where

$$f_u = x/\lambda z \quad \text{and} \quad f_v = y/\lambda z \quad . \quad (5-7)$$

The angular spectrum $A(f_u, f_v)$ after propagation an additional distance Δz is

$$A(f_u, f_v) = A_0(f_u, f_v) \exp\left\{\frac{i2\pi \Delta z}{\lambda} \left[1 - \lambda^2 f_u^2 - \lambda^2 f_v^2\right]^{1/2}\right\} \quad . \quad (5-8)$$

The field after this propagation is therefore

$$\begin{aligned} U'(u, v) = & \frac{\exp(i2\pi z/\lambda)}{i\lambda z} \iint U_1(x, y) \exp\left[\frac{i\pi(x^2 + y^2)}{\lambda z}\right] \\ & \cdot \exp\left\{\frac{i2\pi \Delta z}{\lambda} \left[1 - \frac{x^2 + y^2}{z^2}\right]^{1/2}\right\} \exp\left[\frac{-i2\pi(xu + yv)}{\lambda z}\right] dx dy. \end{aligned} \quad (5-9)$$

The field at the plane P_1 differs from that after the lens L_1 by a phase factor

$$\exp\left\{\frac{i2\pi \Delta z}{\lambda} \left[1 - \frac{x^2 + y^2}{z^2}\right]^{1/2}\right\} \quad (5-10)$$

within the integral in Eq. (5-9). The only effect of this phase factor is once again to change the realization of the image of the object. [See the discussion after Eq. (5-4).] Note that aperture effects have not been included in this initial analysis.

Experimentally, the 2-D speckle intensities at a plane behind the lens and at another plane 50 mm behind the first were detected and found to be very nearly equal. This indicates that the 42 mm propagation distance between the lens L_1 and the plane P_2 does not adversely affect the data collected.

5.5 DETECTOR SAMPLING AND DATA PREPROCESSING

For a rectangular diffuse object of width d_x and d_y in orthogonal directions, the expected value of the normalized autocorrelation of the intensity of the speckle pattern at distance z is [5.7]:

$$R(u, v) = 1 + \text{sinc}\left(\frac{d_x u}{\lambda z}\right) \text{sinc}\left(\frac{d_y v}{\lambda z}\right) \quad (5-11)$$

where λ is the wavelength of illumination and u and v are orthogonal coordinates. The first zeros of the second term in the autocorrelation function are located at $u = \lambda z/d_x$ and $v = \lambda z/d_y$. The Nyquist sampling rates are half these distances, so the detector separations Δu , Δv must satisfy

$$\Delta u \leq \frac{\lambda z}{2d_x}, \quad \Delta v \leq \frac{\lambda z}{2d_y} \quad (5-12)$$

For the objects used in these experiments, the maximum width was about 10 mm, so the Nyquist sample spacing was 40 μm in each direction. For the Fairchild CCD detector, the center-to-center detector separations are 30 μm in the horizontal direction and 18 μm in the vertical direction, so the speckle patterns in the Fourier plane were somewhat oversampled. The video digitizer samples each horizontal line at a spacing of 21.3 μm .

For the speckle in the image plane, the required sample spacings are [5.7]:

$$\Delta x = \frac{\lambda f_2}{2D_u}, \quad \Delta y = \frac{\lambda f_2}{2D_v} \quad (5-13)$$

where f_2 is the focal length of the lens L_2 and D_u and D_v are the aperture dimensions. Since $f_2 = 189$ mm, and, for the small aperture, $D_u \approx D_v \approx 1.25$ mm, the required spacing is $39 \mu\text{m}$. For the large aperture, $D_u \approx D_v \approx 5$ mm, and the required detector spacing is $10 \mu\text{m}$. Note that this spacing is smaller than the pixel spacing of the detector array used. Because this high-resolution image is only used for comparison purposes, sampling it at less than the Nyquist rate has no effect on the success of the iterative algorithm.

An optical Fourier transformation exists between the optical fields in planes P_1 and P_2 of Figure 5-1 while a digital Fourier transformation (e.g., an FFT) will be used when processing the data collected in these two planes. The scaling between these two data sets can be determined as follows [5.1]. The Fourier intensity data is collected as N by M values, electronically sampled by the video digitizer at spacings $\Delta u = 21.3 \mu\text{m}$ and $\Delta v = 18 \mu\text{m}$. When this data is FFTed to the image domain, the resulting data will be again N by M samples with spacings, in the image plane P_2 , of $\Delta x_0 = \lambda f_2 / N \Delta u$ and $\Delta y_0 = \lambda f_2 / M \Delta v$. The actual low and high resolution image data is, again, electronically sampled by the video digitizer at spacings $\Delta x = 21.3 \mu\text{m}$ and $\Delta y = 18 \mu\text{m}$, so the data must be rescaled to be sampled at Δx_0 and Δy_0 . The scaling factors are

$$\frac{\Delta x_0}{\Delta x} = \frac{\lambda f_2}{N \Delta x \Delta u} = 0.84$$

and

$$\frac{\Delta y_0}{\Delta y} = \frac{\lambda f_2}{M \Delta y \Delta v} = 1.17 \quad (5-14)$$

for $N = M = 256$.

For phase retrieval, the image to be reconstructed must occupy no more than $N/2$ by $M/2$ samples. The magnification of the image with respect to the object is f_2/f_1 for the setup shown in Fig. 5-1. For an object of extent d_x in the x -direction, the image extent is therefore $f_2 d_x / f_1$. Using Eq. (5-12) with equality for Δu , we find that $(N/2) \Delta x_0 = \lambda f_2 / 2 \Delta u = f_2 d_x / f_1$ verifying that proper sampling has been achieved.

5.6 EXPERIMENTAL RESULTS

In one series of experiments, images were reconstructed using only Fourier intensity data. The result of one of these experiments is shown in Figure 5-2. In part (a), the square root of the detected Fourier intensity data is shown. This 256 by 256 array of 8 bit data is the result of averaging 256 frames of digitized CCD data. From this data, the autocorrelation of the desired complex-valued image was computed via a Fourier transformation. In part (b), the estimate of the upper bound on the image support obtained by applying the triple intersection method to the thresholded autocorrelation is given [5.5]. Part (c) shows the intensity of the image reconstructed from the Fourier intensity data of part (a) and the support of part (b). For comparison, an optically formed image is shown in part (d). It can be seen that additional details such as the dark stripe on the rectangle and the shape of the triangle have been reconstructed correctly although at lower than actual contrast. Because this image data was collected at a different time than the Fourier intensity data, with a slightly different aperture, and had to be resampled for display, the fine details, such as the speckles, are not expected to agree with those in part (c). In a second experiment, images were not

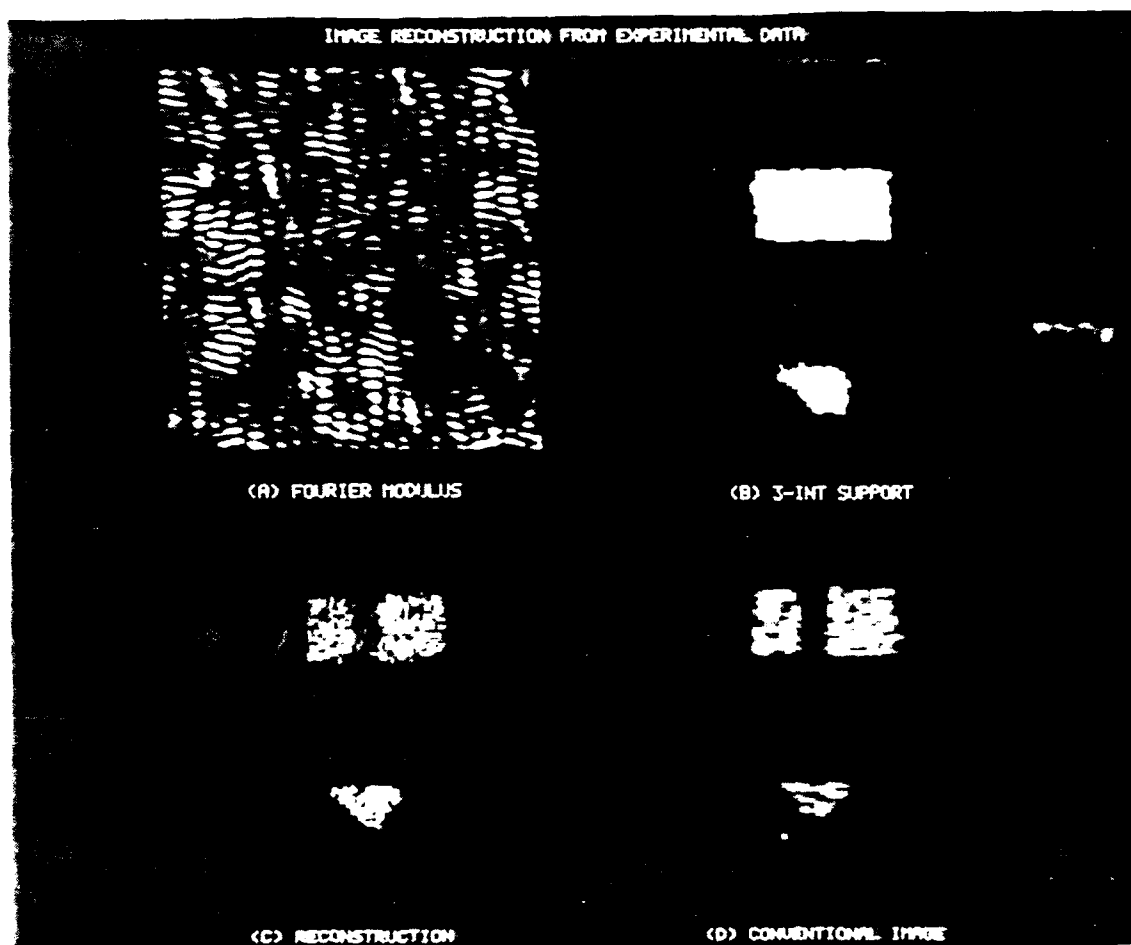


Figure 5-2. Image reconstruction from experimental data. (a) Fourier modulus, (b) image support from triple intersection method, (c) reconstructed image intensity, (d) approximate conventional image intensity for comparison to (c).

successfully reconstructed from Fourier intensity data and low-resolution image data using the method described in Chapter 4. Further work to improve data collection procedures for this case is required.

REFERENCES

- 5.1 J.W. Goodman, Introduction to Fourier Optics (McGraw-Hill, New York, 1968), Chapters 3 and 4.
- 5.2 R.G. Paxman, J.R. Fienup, and J.T. Clinthorne, "The effects of tapered illumination and Fourier intensity errors on phase retrieval," Proc. of the SPIE 828: Digital Image Recovery and Synthesis (in P.S. Idell, ed., San Diego, 1987), pp. 184-189.
- 5.3 J.N. Cederquist and C.C. Wackerman, "Phase-retrieval error: a lower bound," *J. Opt. Soc. Am. A* 4, 1788-1792 (1987).
- 5.4 J.N. Cederquist, J.R. Fienup, J.C. Marron, and R.G. Paxman, "Phase retrieval from experimental far-field speckle data," *Opt. Lett.* 13, 619-621 (1988).
- 5.5 T.C. Crimmins, J.R. Fienup, and B.T. Thelen, "Improved bounds on object support from autocorrelation support and application to phase retrieval," accepted for publication in *J. Opt. Soc. Am. A* (1989).
- 5.6 J.N. Cederquist and J.R. Fienup, "Fine-resolution imaging using phase retrieval (U)," *Proc. 13th DARPA Strategic Systems Symposium* (SECRET, 1987), pp. 393-406.
- 5.7 J.W. Goodman, "Statistical Properties of Laser Speckle Patterns," in Laser Speckle and Related Phenomena, J.C. Dainty, ed. (Springer-Verlag, Berlin, 1984), Section 2.5.

6 SYSTEM ANALYSIS

6.1 INTRODUCTION

A large segment of this research program was devoted to the specification of the hardware and operational characteristics required by a deployed system for image reconstruction and target parameter estimation. In this section of the report, the results of this system analysis study are summarized. Section 6.2 contains a summary of the results pertaining to parameter estimation and Section 6.3 summarizes the results for image reconstruction.

6.2 SYSTEM ANALYSIS FOR PARAMETER ESTIMATION

In this section, several factors that establish limits on the ability to measure target rotation rates using speckle are considered. After an introduction, source requirements, object material properties and receiver requirements are discussed separately.

6.2.1 Principles of Rotation Measurement

Let us consider some of the principles upon which rotation measurement using speckle is based and make a comparison to conventional coherent Doppler radar. The premise for this work is that various components of an SDI target cluster rotate at different rates and that measurement of the rotation rates within a target cluster will allow one to identify the objects present. The use of speckle to measure rotation rate can be regarded as a Doppler technique. Rather than interfering coherent radiation reflected from the object with a local oscillator, as in heterodyning and homodyning, the speckle techniques are autodyne or self-Doppler methods. These methods are based on the interference of light scattered from different regions of the object and do not employ a local oscillator. Researchers have

shown that even though autodyning avoids the complexity associated with having a local oscillator, it has the same sensitivity as heterodyning for measuring Doppler spread [6.1].

Observation of the speckle pattern produced by illuminating a rough, rotating object with a laser beam reveals not only that the intensity at a point in the speckle pattern does exhibit Doppler beating when the object rotates, but also that the beating is imparted by a bodily translation of the speckle pattern. Moreover, the speckle translation is proportional to the object rotation. This observation suggests that rather than measuring rotation simply by temporal processing of the intensity detected at a point as with standard autodyning, one can combine spatial with temporal processing to extract the rotation information. For example, if the speckle pattern is recorded twice by a 2-D detector array with the time interval between recordings equal to Δt , the recordings can be spatially correlated to extract the speckle translation, Δx , which in turn gives the object angular rotation rate, Ω (in radians/sec), via

$$\Omega = \frac{1}{2R} \frac{\Delta x}{\Delta t} \quad (6-1)$$

where R is the range.

One other difference between autodyning and heterodyning worth noting is that heterodyning is intended for measurement of relative motion between the source and target while autodyning is not sensitive to their relative motion. Hence, heterodyning is most sensitive to longitudinal target motion while autodyning concentrates on differences of motion within a target or target cluster. For this reason the frequency content of the heterodyne signal from an object is biased significantly by relative motion which can complicate the extraction of rotation information.

Another quantity important to the discussion of system capabilities is the time that it takes a speckle to translate over a point in the detection plane. This time is the inverse of the required detector bandwidth. With the speckle size given by $\lambda R/d$, where λ is the illumination wavelength, R is the object range and d is the object diameter, it follows that the bandwidth required of each detector to ensure Nyquist sampling is given by

$$B = 4\Omega d/\lambda \quad (6-2)$$

The system used to conduct these rotation measurements could actually be constructed to operate in a number of possible modes. We believe that the optimal system would have a laser source that operates in a long pulse mode and a 2-D detector array for which each element has bandwidth given by Eq. (6-2). As the object rotates the speckle pattern is recorded as a function of time. To compute the speckle translation, speckle data collected at a minimum of two different times is required. The temporal separation, Δt , of this data should be set so that the speckle translation is detectable.

6.2.2 Source Requirements

To accomplish target rotation measurement for the SDI mission, the laser source must have sufficient output power and coherence length. The coherence length must be twice the depth of the object so that, at a given time, the light scattered from the entire target adds coherently at the detector. If this condition is met, the speckle contrast is unity; otherwise, speckle with reduced contrast results and measurement of speckle translation degrades.

The laser pulse must be long enough so that the speckle translates a detectable amount. The pulse length must also be long enough so that the light at the detector originates from the entire depth, ΔR , of the object. If the pulse is too short, only a slice of the object is

illuminated at a time. With each slice giving an independent speckle pattern, the resultant pattern integrated over the entire pulse has reduced contrast which decreases the ability to measure rotation. Even when the pulse is sufficiently long to illuminate the entire depth at once, the leading part of the pulse (of length ΔR) and the trailing part (of length ΔR) are not useful because the entire object is not illuminated. These regions of the pulse act to reduce the speckle contrast and reduce measurement accuracy. One can define a pulse utilization parameter to quantify the fraction of the pulse that is useful

$$\text{Pulse Utilization} = 1 - 2\Delta R/c\tau \quad (6-3)$$

where c is the speed of light and τ is the pulse length. The value given by Eq. (6-3) should be as close to unity as attainable, that is, long pulses with $\tau \gg 2\Delta R/c$ should be used.

If the value of Eq. (6-3) is positive, which signifies that for some fraction of time the entire object is illuminated, but the value is not close to unity because the pulse is short, one could employ range gating at the receiver to reject the leading and trailing edges of the pulse. Such range gating, however, implies having detection electronics that are more complex, and of higher bandwidth, than those required for long pulse operation.

In summary, it is expected that system complexity is minimized by operation with long pulses for which $\tau \gg 2\Delta R/c$. Furthermore, the pulse length should be long enough so that the desired speckle translation is observed within one pulse. Except for very slow rotation rates, this condition will normally be met by $\tau \gg 2\Delta R/c$. (For slow rotation rates, two pulses can be used to collect data at the required two different times.) For this system the bandwidth for each detector in the receiver is given by Eq. (6-2).

6.2.3 Object Material Properties

To perform rotation measurements using speckle it is assumed that the object is diffusely reflective so that the speckle pattern is fully developed and has unit contrast. The degree of diffuseness is characterized by the scattering cross-section as a function of the angle between the object's local surface normal and the illumination angle. As the degree of diffuseness decreases, or the angular extent of the scattering cross-section becomes narrower, the principle effect is that the speckle size increases due to the smaller effective object size. The increase in speckle size reduces the SNR for rotation measurement because the SNR for rotation measurement is proportional to the square root of the total number of speckles in the detection aperture. Although the SNR is reduced, the bandwidth requirement given by Eq. (6-2) is relaxed because of the increased speckle size.

6.2.4 Receiver Requirements

The receiver described in Section 6.2.1 for making rotation measurements using speckle is a 2-D detector array. The size of the array should be large so that it encompasses a large number of independent speckles since the SNR is given by Eq. (2-17):

$$SNR = \left[\frac{4MK}{20 + 12/(N\langle n \rangle) + 2/(N\langle n \rangle^2)} \right]^{1/2} \quad (6-4)$$

where M is the number of independent speckles encompassed by the detector array, K is the number of independent frame pairs used to measure the correlation from which rotation rate is determined, N is the number of detection channels per speckle and $\langle n \rangle$ is the mean number of detected photons per detection channel. The number of detected photons per speckle is equal to $N\langle n \rangle$. The detector spacing should be set according to the finest expected Nyquist sampling frequency to

avoid aliasing, that is, the spacing should be less than or equal to $\lambda R/2d$. It must be noted, however, that oversampling results in a lower SNR when operating at low-light levels since, by Eq. (2-18):

$$\text{SNR} = [2M K/N]^{1/2} \quad (6-5)$$

and the optimum value of N is the minimum value, two, allowed by Nyquist sampling, when $N\langle n \rangle$ is held constant.

6.3 SYSTEM ANALYSIS FOR IMAGE RECONSTRUCTION

In this section the results of the system study for image reconstruction are given. Section 6.3.1 is devoted to discussion of the source and sensor requirements and Section 6.3.2 contains a discussion of simulation experiments for characterization of image reconstruction error in the presence of noise. Section 6.3.3 contains a brief description of the computational requirements for image reconstruction.

6.3.1 Source and Sensor Requirements

The basic hardware elements for performing image reconstruction are a pulsed laser source, a 2-D array of light-bucket type detectors and a low-resolution imager. As detailed in Section 4, the detector array provides object Fourier magnitude, or pupil-plane information, while the low resolution imager picks off a portion of the Fourier magnitude data using a beamsplitter and provides a low-resolution diffraction-limited image. This low-resolution image serves two purposes; first, application of the Gerchberg-Saxton phase retrieval algorithm yields the phase of the optical field over the region of the pupil plane corresponding to the low-resolution image. Second, the low-resolution image serves as a support constraint for reconstruction of the high-resolution image using the expanding Fourier modulus method described in Section 4.

The source and detector requirements are basically the same as those for parameter estimation discussed in Section 6.2, except that for good image reconstruction performance (yet to be quantified) it is required that one have a higher power laser (to increase the SNR of the data) than is required for parameter estimation. For slowly rotating objects or non-rotating objects it may be possible to integrate returns from several pulses.

6.3.2 Simulation Experiments

In this section the results of simulations conducted to characterize the performance of the image reconstruction algorithm in the presence of noise are presented. The first simulation is a comparison of image quality obtained using phase retrieval (under ideal circumstances) to conventional diffraction-limited imaging. The object used was a simulated PBV-RV complex-valued object. For phase retrieval, the pupil-plane Fourier magnitude was computed with Poisson statistics to simulate low light level noise. An image was then reconstructed using the iterative transform algorithm with the exact image domain support constraint, and the normalized rms error in the reconstructed image intensity was computed. For the conventional diffraction-limited image, Poisson statistics were applied to the image and the resulting image-domain error was computed.

Figure 6-1 compares image quality for phase retrieval and conventional imaging as a function of the number of photons per speckle. For high light levels (26000 photons per speckle) both methods produce very high quality images. At the light level of roughly 1000 photons per speckle, the error in the phase retrieval image begins to increase markedly. It is important to note that, even at the light level of 600 photons per speckle, the error of 0.30 associated with phase retrieval corresponds to an image that does contain recognizable features. In practice, the support will not be known exactly, so imaging performance could be poorer than for these

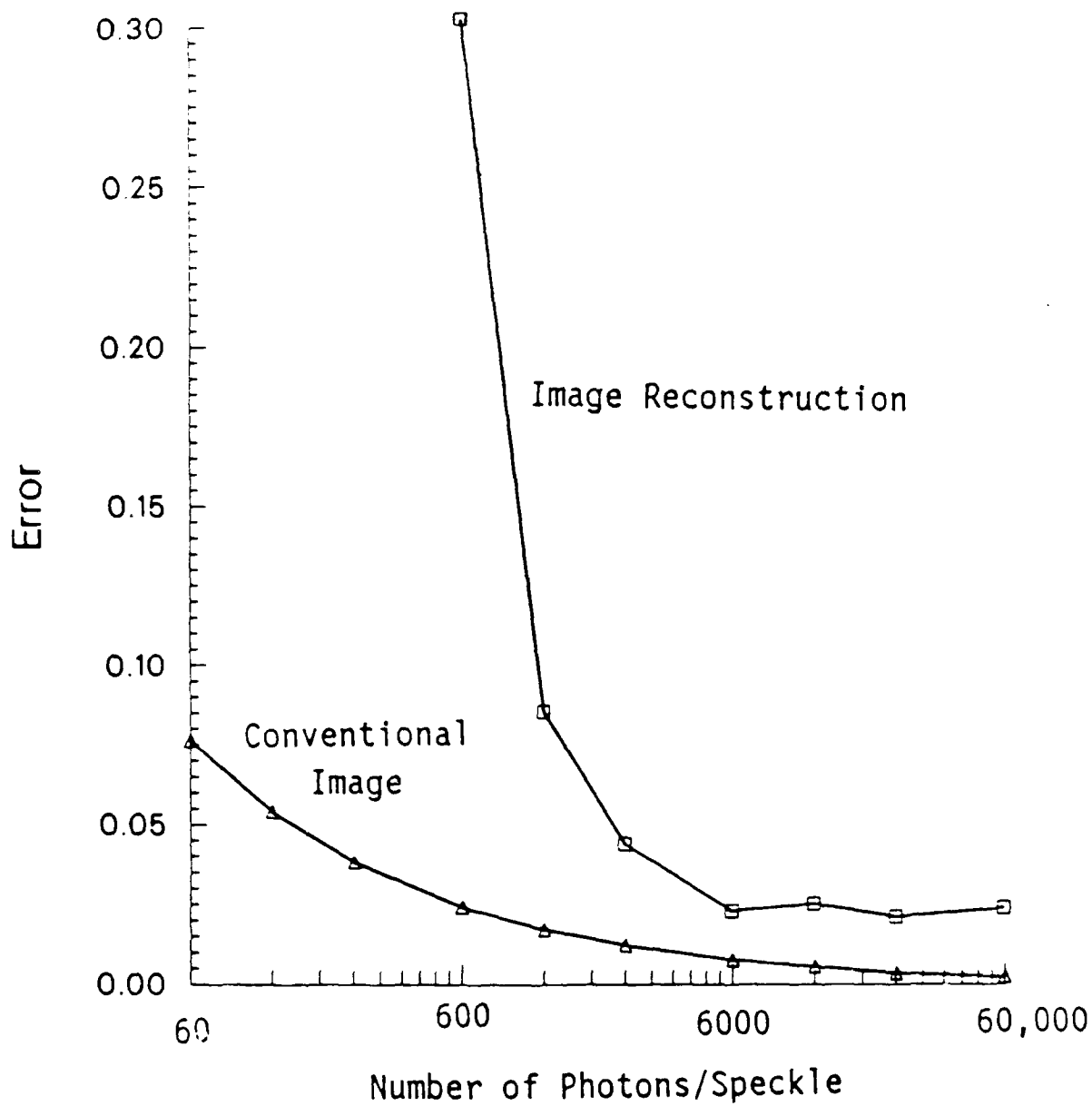


Figure 6-1. Normalized rms error in image intensity for image reconstructed by phase retrieval and for conventional image versus number of detected photons/speckle.

experiments. Thus Figure 6-1 should not be used to establish the lower limit on light level when using phase retrieval. In future work a thorough characterization of the algorithm at low light levels will be conducted to establish the lower limit. This study will include analysis of the sensor configuration, the estimation of the support constraint, and the specific form of the phase retrieval algorithm to obtain an accurate estimate for the lowest allowable light level.

Another series of simulations was conducted to determine reconstructed image quality as a function of noise in the Fourier magnitude data. The exact image domain support constraint was used and Gaussian noise was added to the Fourier intensity. The results of this simulation are shown in Figure 6-2.

6.3.3 Computational Requirements

The dominant computational burden in iterative phase retrieval algorithms is the 2-D FFT operation; two 2-D FFT's are required per iteration. To reconstruct an image it thus follows that the number of real additions and multiplications required is of the order $20MN^2/\log_2 N$, where M is the number of iterations required and N^2 is the number of pixels in the reconstructed image. For $N = 64$ and $M = 100$ it follows that 50×10^6 real additions and multiplications are required.

To assess the ability of advanced hardware to accommodate phase retrieval we considered VHSIC technology and in particular, the Westinghouse Pipelined Arithmetic Unit (PLAU). The PLAU is capable of performing 40×10^6 operations per second. For the above example of $N = 64$ and $M = 100$ it follows that a single PLAU is capable of reconstructing an image in about 1.25 sec. Future advances in processor technology including highly parallel computing architectures can be expected to lower the time required for reconstruction considerably.

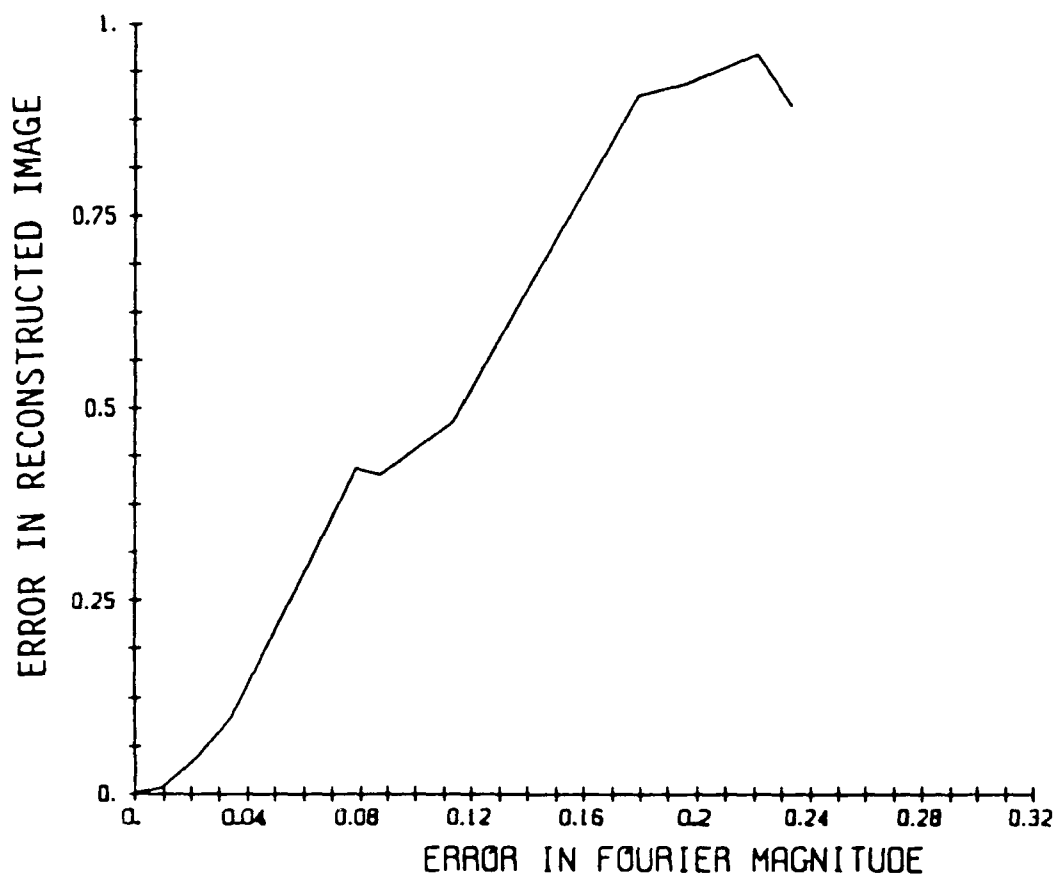


Figure 6-2. Normalized rms error in image reconstructed by phase retrieval versus normalized error in Fourier magnitude data (due to additive Gaussian noise in Fourier intensity).

REFERENCE

- 6.1 D.V. Flukiger, R.J. Keyes, and J.H. Shapiro, "Optical Autodyne Detection: Theory and Experiment", Appl. Opt. 26, 318-325 (1987).

APPENDIX ERROR VARIANCE RELATIONSHIPS

We relate the variance of the error of an optical field (or the Fourier transform of a complex-valued image) to the variance of its phase error for a zero-mean Gaussian-distributed phase error.

Let

$$G(u) = F(u) \exp[i\phi_e(u)] \quad (A-1)$$

be the aberrated optical field, where F is the ideal optical field and ϕ_e is the phase error. Suppose ϕ_e has point statistics that are Gaussian zero mean with standard deviation σ_ϕ . First consider the case without normalizing G . Then the variance of the error (i.e., the mean square error) of $G(u)$ is

$$\begin{aligned} E^2 &= A^{-1} \int |G(u) - F(u)|^2 d^2u \\ &= A^{-1} \int |F(u)|^2 |1 - \exp[i\phi_e(u)]|^2 d^2u \\ &= A^{-1} \int |F(u)|^2 4 \sin^2[\phi_e(u)/2] d^2u \end{aligned} \quad (A-2)$$

where A is the area of integration. Assuming the phase errors are independent of $|F(u)|$, and approximating the integral by an ensemble average yields

$$\begin{aligned} E^2 &\approx 4 \langle |F(u)|^2 \sin^2 [\phi_e(u)/2] \rangle \\ &\approx 4 \langle |F(u)|^2 \rangle \langle \sin^2 [\phi_e(u)/2] \rangle . \end{aligned} \quad (A-3)$$

Using the identity

$$\int_0^{\infty} \exp(-px^2) \sin^2(ax) dx = \frac{1}{4} \sqrt{\frac{\pi}{p}} [1 - \exp(-a^2/p)] \quad , \quad [p > 0] \quad (A-4)$$

the average over the distribution of phases is given by

$$\begin{aligned} \langle \sin^2[\phi_e(u)/2] \rangle &= \int_{-\infty}^{\infty} \sin^2(\phi_e/2) \frac{1}{\sqrt{2\pi} \sigma_{\phi}} \exp\left[-\phi_e^2/2\sigma_{\phi}^2\right] d\phi_e \\ &= (1/2) \left[1 - \exp\left[-\sigma_{\phi}^2/2\right]\right] \quad . \end{aligned} \quad (A-5)$$

Inserting this into Eq. (A-3) yields

$$e^2 \equiv \frac{E^2}{\langle |F(u)|^2 \rangle} \simeq 2 \left[1 - \exp\left[-\sigma_{\phi}^2/2\right]\right] \quad . \quad (A-6)$$

Note that $e^2 \rightarrow 2$ for $\sigma_{\phi} \rightarrow \infty$ and

$$e^2 \simeq \sigma_{\phi}^2 \quad \text{for} \quad \sigma_{\phi}^2 \ll 1 \quad . \quad (A-7)$$

Next consider the case of a normalized G , as in Eq. (4-3):

$$E^2 = A^{-1} \int |\alpha G(u) - F(u)|^2 d^2u \quad (A-8)$$

where

$$\alpha = \frac{\int G^*(u') F(u') d^2u'}{\int |G(u'')|^2 d^2u''} \quad . \quad (A-9)$$

then

$$\langle a \rangle = \frac{\langle G^* F \rangle}{\langle |G|^2 \rangle} = \frac{\langle |F|^2 \rangle \langle \exp(-i\phi_e) \rangle}{\langle |F|^2 \rangle} \quad (A-10)$$

$$= \langle \exp(-i\phi_e) \rangle = \exp(-\sigma_\phi^2/2) \quad (A-11)$$

Thus

$$\begin{aligned} E^2 &\approx A^{-1} \int |F(u)|^2 |\exp(-\sigma_\phi^2/2) \exp[i\phi_e(u)] - 1|^2 d^2u \\ &= A^{-1} \int |F(u)|^2 \{ \exp(-\sigma_\phi^2) + 1 - 2 \exp(-\sigma_\phi^2/2) \cos[\phi_e(u)] \} d^2u \\ &\approx \langle |F(u)|^2 \rangle \{ \exp(-\sigma_\phi^2) + 1 - 2 \exp(-\sigma_\phi^2/2) \langle \cos[\phi_e(u)] \rangle \} \\ &= \langle |F(u)|^2 \rangle [\exp(-\sigma_\phi^2) + 1 - 2 \exp(-\sigma_\phi^2/2) \exp(-\sigma_\phi^2/2)] \\ &= \langle |F(u)|^2 \rangle [1 - \exp(-\sigma_\phi^2)] \quad (A-12) \end{aligned}$$

or

$$e^2 = \frac{E^2}{\langle |F(u)|^2 \rangle} \approx 1 - \exp(-\sigma_\phi^2) \quad (A-13)$$

Note that for the normalized case, unlike the unnormalized case, $e^2 \rightarrow 1$ for $\sigma_\phi \rightarrow \infty$ and, like the unnormalized case, $e^2 \approx \sigma_\phi^2$ for $\sigma_\phi^2 \ll 1$.

By Parseval's theorem it can be shown that the variance of the error in the image domain is equal to the variance of the error in the Fourier domain.

Just as image shifts can be taken out before computing errors to allow for the fact that image shifts are unimportant to image quality, linear components of the phase error $\phi_e(u)$ can be taken out before computing σ_ϕ or e^2 .